La Sapienza
Università di Roma

DOCTORAL THESIS

Radiation effects for the next generation of synchrotron radiation facilities

Department of Physics
PhD School on Accelerator Physics
Cycly XXXIV

RESEARCH CONDUCTED AT
Instituto Nazionale di Fisica Nucleare
Milano Unit

Supervisor:
Prof. Dr. Luca SERAFINI
Prof. Dr. Vittoria PETRILLO

By:
Marcel RUIJTER
Matricola 1842024

2022

SAPIENZA
UNIVERSITÀ DI ROMA

DOCTORAL THESIS

Radiation effects for the next generation of synchrotron radiation facilities

Marcel RUIJTER
Matricola 1842024

Sapienza Università di Roma
Department of Physics
PhD School on Accelerator Physics
Cycly XXXIV

RESEARCH CONDUCTED AT
Instituto Nazionale di Fisica Nucleare
Milano Unit

Supervisor:
Prof. Dr. Luca SERAFINI
Prof. Dr. Vittoria PETRILLO

2022

Declaration of Authorship

I, Marcel RUIJTER, declare that this thesis titled, “Radiation effects for the next generation of synchrotron radiation facilities” and the work presented in it are my own. I confirm that:

- This work was done wholly or mainly while in candidature for a research degree at this University.
- Where any part of this thesis has previously been submitted for a degree or any other qualification at this University or any other institution, this has been clearly stated.
- Where I have consulted the published work of others, this is always clearly attributed.
- Where I have quoted from the work of others, the source is always given. With the exception of such quotations, this thesis is entirely my own work.
- I have acknowledged all main sources of help.
- Where the thesis is based on work done by myself jointly with others, I have made clear exactly what was done by others and what I have contributed myself.

Signed: 

Date: 05/05/2022

SAPIENZA UNIVERSITÀ DI ROMA

Department of Physics

Accelerator Physics

Instituto Nazionale di Fisica Nucleare

Abstract

Radiation effects for the next generation of synchrotron radiation facilities

by Marcel RUIJTER

High energy radiation is an important tool for many fields of research as it allows for the measurement of smaller structures and atomic interactions.

The current best method of generating coherent and narrow bandwidth synchrotron radiation is with a free electron laser. It requires very high charge density, to start the amplification process and concurrently leads to its high level of coherency, and high energies (GeV to obtain keV photons). The stringent parameters on the electron bunch are met by linear accelerators. These are typically kilometre long straight structures that operate from tens to 100 Hz repetition rate. A novel design was proposed by the INFN Milan research group called MariX [1]. Here a LINAC is used in combination with a compression arc. This reduces the size of the facility, because the electron bunch can be accelerated twice by the same LINAC. As the electrons pass through dipoles in the compression arc the fields emanating from the particles in the bunch can cause deterioration to it. These fields, consisting out of the relativistic Coulomb- and radiation field, travel with the speeds of light, and thus originate from a point in the past. For this reason the behaviour of these retarded fields is investigated from first principles and developed into a 3D algorithm for calculating the forces within a bunch. An in depth overview is given on how the constituent fields behave over a large range of electron energies. Proportionality relations are given that determine which one is dominant.

To reach unprecedented high energy photons is through the scattering of intense lasers with electron bunches; (inverse) Thomson or Compton scattering. Photon energies of keV can be reached with tens of MeV electrons, and MeV photons with GeV electrons.

High repetition rate collisions are possible with cavity based laser systems. Currently the power inside the cavity is several hundreds of kW with an intensity at the focus up to 10^{14-15} [W/cm^2]. With these high powers the cavities can become degenerate, i.e. higher order transverse modes are excited, either by imperfections of the mirrors or deformations caused by heat dissipation. A short study provides insights to the observability of these modes in the Thomson spectrum.

The general method for Thomson scattering is to have a (quasi) monochromatic laser pulse collide with an electron bunch with a very small energy spread. The latter usually leads to a reduction of the number of charges, and therefore the flux of scattered photons. The frequency of the scattered radiation is linearly dependent on that of the laser's, and therefore the energy spread of the electrons could be compensated by including a frequency modulation. The highest intensity lasers obtained are by chirped pulse amplification and thus readily available. Two schemes have been investigated: longitudinal and transverse chirp. Both can reach the limit in bandwidth and number of photons scattered of the mono-energetic and mono-chromatic case.

For ultra shorted pulses the carrier envelope phase becomes an important variable. Thomson scattering can be used to measure For intensities where non-linear effects dominate, because the scattered radiation contains the information of the laser pulse.. A model of its signature in the Thomson spectrum has been developed: it shifts the peaks of higher harmonics that overlap. This shift is also correlated to the emission direction of harmonics. A detailed analysis is given how to measure it experimentally.

Contents

List of Figures

List of Tables

Chapter 1

Introduction

1.1 Accelerators as Radiation Sources

One of the applications or objectives of an accelerator structure is to produce radiation, which is the key to probe, control or explore physical processes. To give a broad overview of the photon energies required for some research topics:

- Photon energy < eV: wavelength ~ 10 μm-200μm : frequency < 10^{14} Hz (THz)
  This radiation is of particular interest for material properties and monitoring of manufacturing [2, 3], and manipulating chemical and biological processes [4, 5].
- Photon energy ~ keV : wavelength ~ nm : frequency > 10^{17} Hz
  finds its purpose in medical and biology applications such as cancer treatment and invivo imaging [6, 7], nuclear & atomic research such as resonance fluorescence [8, 9] resolving microscopic structure and dynamics (e.g. electron re-collision [10]).
- Photon energy ~ MeV : wavelength ~ pm : frequency 10^{20} Hz
  Laboratory astrophysics research [11] and quantum physical effects such as vacuum birefringences [12] and hadron dynamics [11].

The radiation is emitted by relativistic electrons following curved trajectories, and is called *Synchrotron radiation*. The main advantage of such sources is that the radiation can be controlled by the parameters of the charges and the external field (that are the cause for the curved trajectories). An important parameter is the number of charges (N_e), or charge density, because the amount of radiation emitted scales with N_e for incoherent- and N_e^2 for coherent radiation. To reach the coherent limit the electron bunch needs to be extremely small, smaller than the wavelength it emits, over the time of emission; the volume of the bunch and its divergence needs to be small. This, in a sense, means that the bunch can be approximated more as a point source, which is a coherent source. In the accelerator community the quality term for the point-source-likeness and number of charges is called the *brightness* of a bunch. Complementary the term *brilliance* is used for the radiation, which also includes the bandwidth of the emitted radiation. The latter is included because for high energy photons it is especially hard to manipulate them, if possible at all. Besides additional costs, increase of the facility it will inevitably lead to losses. It is therefore better to have a narrow bandwidth source from the start. Thus lets look at the various types of generation techniques, and the energy requirement on the electrons.

1.2 Types of Synchrotron Radiation

Synchrotron radiation is emitted by a charged particle when it experiences a force perpendicular to its propagation direction. The process is thus described fully by classical electrodynamics. The term refers to the synchrotron accelerator, more on that in the Section 1.3, but due to the general description of the process it even includes astronomical objects: Also an accretion disc emits synchrotron radiation! More down to earth, in the next sections a brief overview of the theoretical history is given and whereafter the main methods to produce synchrotron radiation are discussed.

A Brief Historical Account on the Theoretical Development

Theoretical works on radiation emitted by a (classical) charge can be traced back as far as 1897 (Larmor) for the low energetic case, 1898 (Lienard) and 1900 (Wiechert) for the relativistic case. This should come as a bit of a surprise, since special relativity had yet to be developed. For instance the Lorentz factor was derived in 1905. The reason why the theory of emission could have been precede is that the speed of light c is a Lorentz invariant! The works of Lienard was extended by Schott 1907 [13], providing angular energy distributions for relativistic electrons following a circular path [14, 15].

The first synchrotron facilities built had their primary focus on high energy physics, and somewhat surprisingly the notion of the emission of radiation was essentially unknown in this community [16]. With the advances of the accelerator community the radiative energy losses got renewed attention by Pomeranchuk (1939), Pomeranchuk & Artsimovich(1945) [17, 16].

Blewett proposed to test the predictions of Pomeranchuck, and experimentally confirmed the orbital deviations [18]. Radiation itself, however, was not measured by Blewett, as the expected radiation wavelength by Blewett was in the radio frequency range, but was emitted in the near-infrared range. Experimental evidence of emission of radiation happened by accident in 1947 by a technician (Floyd Haber) looking into the (open) beamline with a mirror of the General Electric Laboratory, Schenectady, New York Synchrotron expecting to see sparks from electrons [14]. And hence the term “synchrotron radiation” was coined. Although Blewett had access to the work of Schwinger, it was not published until 1949 [19], in which the previous theoretical works were refined further and worked out in great detail.

To increase the brilliance of the synchrotron facilities devices were developed that would be placed in the straight sections of the synchrotron: undulators & wigglers. These are arrays of alternating dipole magnets and causes the bunch to oscillate in them. They were first proposed by in 1947 by Ginzburg and demonstrated in 1953 by Motz [20]. The emitted radiation and the electron bunch co-propagate and can affect each other. This was realised by Madey and presented the amplification process in 1971 [21] and goes by the name of the free electron laser. It requires a large electron density while it traverses the undulator: high brightness bunches.

From the late 90’s a new theoretical, and numerical, endeavour started: the influence of the fields from the charges on the bunch itself. The reason for this is because increasing the brightness is easiest by compression of the bunch. The size of the bunch is now comparable to a range of the frequencies it emits as synchrotron radiation in the beamline. A 1D model, or longitudinal wakefield, has been presented by Derbenev [22] and Saldin [23].

Another branch of radiation emission was studied coincidentally in the early 20^{th} century. Thomson developed the theory of free electrons scattering radiation in 1906 [24]. This process can be understood by imagining the electric field causing the electron to oscillate leading to dipole radiation. A relativistic and non-linear formulation was provided as early as 1949 by Sengupta, 1963 Vachaspati and 1970 Sarachik and Schappert [25].

Compton put forth his theory of scattering for low energy particles with photons in 1923 supported by his experiments and further cementing the field of quantum mechanics. The theoretical works were refined to include relativistic energies by Dirac in 1926 and Gordon in 1927, and after by Klein-Nishina in 1929 by including negative energy states [26]. Some decades later the non-linear quantum processes were published by Nikishov & Ritus [27]. These two scattering theories are the two limits of the same phenomenon; classical and quantum in nature.

The early analytical solutions of the scattering processes consisted out of plane wave dynamics, see for example [28]. In the 90’s solutions started to appear for Thomson scattering where the laser pulses is described by both a temporal and a transverse profile [29].

1.2.1 General Scaling of Emission of Radiation

The radiation sources can be dived into groups depending on the characteristics of the electron motion; Dipole, undulator, electron-photon scattering. The most general way to describe the power emitted by a particle is through the relativistic Larmor formula

$$P_{\text{ower}} = -\frac{2}{3}\frac{e^2}{m^2 c}\frac{dP^\mu}{ds}\frac{dP_\mu}{ds} \tag{1.1}$$

where e is the electic charge, m is the electron mass, c is the speed of light, $\gamma = \frac{1}{\sqrt{1-\beta^2}} = \frac{E_{\text{nergy}}}{mc^2}$ is the Lorentz factor and $P^\mu = mc\gamma\begin{pmatrix}1\\ \vec{\beta}\end{pmatrix}$ is the relativistic momentum of the electron and $\frac{dP^\mu}{ds}$ is its acceleration with $ds = \frac{dct}{\gamma}$ the spacetime infinitesimal. The acceleration occurs from an external field and its magnitude depends on the incidence angle of the electron. If one averages over an arbitrary incidence angle the average power is given by [30]

$$\langle P_{\text{ower}}\rangle = \frac{4}{3}\sigma_{Th}\beta^2\gamma^2 cU_f \tag{1.2}$$

$$\langle\omega\rangle \propto \gamma^2\omega_{U_f} \tag{1.3}$$

where $\sigma_{Th} = \frac{8\pi}{3}r_e^2$ is the Thomson cross-section with $r_e = \frac{e^2}{mc^2}$ being the classical electron radius, U_f is the energy density of the field the electron traverses and ω_{U_f} is the frequency with which the particle gyrates inside the field. Due to the relativistic nature of the electron the radiation is emitted in a narrow cone ($\sim \frac{1}{\gamma}$) in the direction of propagation, as is depicted in Fig 1.1. For repeating curved trajectories the emission cones can align, depending on the angular deflection.

The electromagnetic fields, for synchrotron radiation, are usually perpendicular to the propagation direction of the electron. In theoretical works it is quite common to change frame of reference, to one where the mathematical complexities are reduced. By performing a Lorentz transformation the electric and magnetic fields change in magnitude and exchange. However the field can be normalized by using the vector potential and the dynamics can be described using

$$a_0 = \frac{eA_0}{mc^2} = \frac{eE_0}{mc\omega_{U_f}} = \frac{eB_0}{mc\omega_{U_f}} \tag{1.4}$$

and is related to the energy density of the field ($U_f \propto (\omega_{U_f} a_0)^2$). It also describes when higher harmonics by an electron are emitted. For this we need the quantum picture of this parameter: a_0 represents the energy gain of an electron within one Compton wavelength per photon [27, 31, 32]. If $a_0 \geq 1$ then more than one photon is absorbed by the electron and emitted as one, thus giving the higher harmonics.

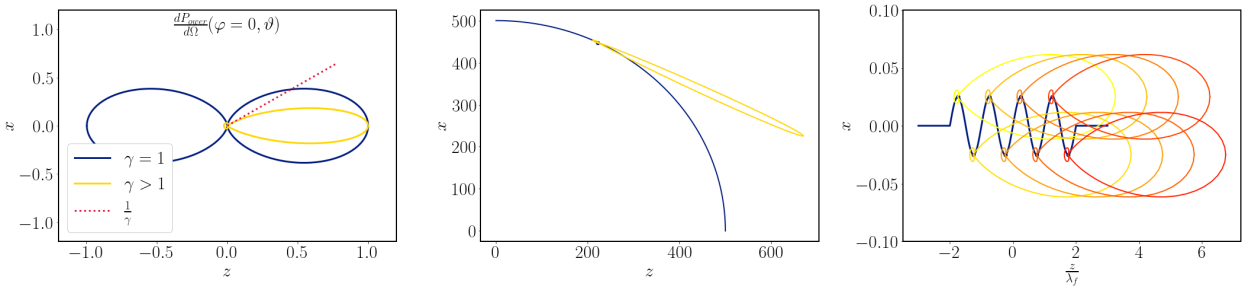

Figure 1.1: Schematic illustration of synchrotron radiation. Due to the relativistic velocity of the electron the radiated power distribution is confined into a narrow cone.
Left: Normalized power distribution for dipole oscillations $\gamma = 1$ and instantaneous circular motion $\gamma > 1$. The power emitted is confined to a $\frac{1}{\gamma}$ cone.
Middle: Power distribution for a particle travelling along a circular path like in a dipole.
Right: An electron follows an oscillating path like in an undulator or when colliding with a laser pulse. At each peak the motion can be approximated as an instantaneous circular motion, and the power distribution of emitted radiation overlap. The colours are only for differentiation purposes.

1.2.1.1 Synchrotron - Dipole magnet

An electron passing through a dipole magnet will follow a curved path with a radius proportional to $\frac{\gamma}{B_0}$. An observer far from this trajectory will see a single short flash from the electron (per round trip). From Fourier analysis one can anticipate that the shortness of the flash leads to a broad spectrum. This can also be understood the normalized vector potential. Although the dipole is a constant field one can use the electron's revolution frequency to determine $a_{0,Dipole} = \gamma$. This means that the spectrum contains harmonics independent of the energy of the electron (since $\gamma \geq 1$). [1] As given in [34] the average frequency emitted is given by

$$\langle \omega \rangle = \frac{4}{5\sqrt{3}} \gamma^2 c \frac{eB_0}{mc^2} \tag{1.5}$$

The critical harmonic number is given by $\frac{3}{2}\gamma^3$. For a dipole with $B_0 = 1$[Tesla] the electron energy required for the average frequency emitted are:

- eV (THz) : 10 μm: $\gamma \sim 30$, $R \sim 10^{-2}$[m]
- keV: 1 nm: $\gamma > 10^3$, $R = 2$[m]
- MeV: 1 pm: $\gamma > 10^5$, $R = 60$[m]

1.2.1.2 Undulator - FEL

An undulator consists out of a series of dipole magnets with alternating polarity. An electron traversing it will oscillate and consequently emit radiation with a wavelength according to

$$\lambda \propto \frac{(1 + a_{0,u}^2)}{(1+\beta)\gamma^2} \lambda_{\text{undulator}} \tag{1.6}$$

where λ_u is the length of two magnets of opposing polarity. The normalized field constant for an undulator (in literature often denoted as the undulator parameter "K") is given by

$$a_{0,u} = \frac{eB_u}{mc} \frac{\lambda_u}{2\pi} \tag{1.7}$$

[1] There exists the quantum description of the radiation emitted: virtual photons that surround the electron are scattered into existence [33].

Undulators have typically a wavelength of $\lambda_u \geq 2$ [cm] and $a_{0,u} \sim 1$ ($B_u \sim 1$ [Tesla]). For these parameters the energy requirements are

- eV (THz) : 10 μm: $\gamma \sim 50$
- keV: 1 nm: $\gamma > 10^3$
- MeV: 1 pm: $\gamma > 10^5$

When the field strength $a_{0,u} \geq 1$ also higher harmonics are emitted. At the start of the undulator the electrons emit incoherently (proportional to N_e). Because the electrons and the radiation propagate in the same direction, they can interact with one another. The density distribution of the electrons get modulated proportional to the wavelength of the radiation, and in return the electrons emit more coherently. This is the basic principle of a free electron laser. The strength of the coupling between the field and the electrons scales with the Pierce[2] parameter (often called the FEL parameter)

$$\rho = \frac{1}{\gamma}\left(\frac{a_{0,u}}{4}\frac{\omega_p}{\omega_u}\right) \tag{1.8}$$

where $\omega_p = \left(\frac{4\pi r_e c^2 n_e}{\gamma}\right)^{1/2}$ is the plasma frequency and $\omega_u = c\frac{2\pi}{\lambda_u}$. To start this amplification process requires a large enough electron density, contained over the length of the undulator. In other words to operate an FEL requires a high brightness electron bunch. The propagation length at which the field starts its exponential growth is given by [36]

$$L_g = \frac{\lambda_u}{2\pi\sqrt{3}\rho} \tag{1.9}$$

The amplification process does not continue indefinitely, at some point a steady state is reached where the modulation of the electrons and the amplitude of the field oscillate. This saturation length is approximately $\sim 20L_g$ where the power is

$$P = \sqrt{2}\rho P_0 \tag{1.10}$$

where P_0 is the power of the spontaneous emission. From here we see that the power at saturation scales with $N_e^{4/3}$ as has been observed experimentally [37].

1.2.1.3 Electron-Photon Scattering

Another way to produce high energy radiation is through the collision of low energy photons with high energy electrons, whereby the energy of the electron is transferred to the photon. Although this process is quantum in nature the process can also be described using classical electrodynamics when ≤ 1 [eV] photons (infrared lasers) collide with electrons up to the GeV range, in which case it is called Thomson scattering. In the linear regime the electron oscillates due to the electric field of the laser pulse, and the emitted radiation for a head-on collision is given by

$$\lambda_{scatter} \propto \frac{\lambda_l}{(1+\beta)^2\gamma^2} \tag{1.11}$$

Through the small wavelength of high power lasers (around 1 [μm]) the energy of the electrons need to be much smaller to reach keV energies as compared to undulator radiation. For a laser with a 1 [μm] wavelength require the following electron energies

- keV: 1 nm: $\gamma \sim 50$
- MeV: 1 pm: $\gamma > 10^3$

[2] It was derived in 1950 by Pierce [35] in his detailed study on coupling between fields and currents.

Unfortunately, the reduction is energy as compared to an undulator also directly leads to lower emitted power, as it scales with γ^2. The first experimental demonstration of Thomson scattering with relativistic electrons was performed in the 1960s [38, 39]. The energy of the lasers in these demonstrations were 10's of Joules and a temporal length of ~ milliseconds. This combination leads to a very low energy density; $U \sim 10^{-5}$ [J/cm^3] ($a_{0,l} \sim 10^{-7}$). The increase of the energy density of lasers mainly comes by shortening the pulse length. For example the first MeV photon beam was produced at Adone Frascati [40] with a laser of $3 \cdot 10^{-7}$ Joules, and a temporal length of 1 ns, reaching the same energy density as the aforementioned one.

Currently there are two main methods to produce laser pulses with energy densities for the use of Thomson/Compton scattering: Cavity based or chirped pulse amplification. The former reaches up to $a_0 \sim 10^{-3}$ and provides collision rates of MHz. Chirped pulse amplification are phenomenal in their energy density $a_0 \geq 1$, by compressing the pulse down into the subpico second range. They however come at the cost of repetition rates on the order of 1-10 Hz.

1.3 Relativistic Electron Sources for the Production of Radiation

As we just saw, the energy of electrons needs to be highly relativistic for the production of radiation. There are currently two main methods to obtain high brightness beams: linear radio frequency - and plasma wakefield accelerators.

Linear Accelerator

There are two limiting factors for a LINAC: 1) the maximum strength of the electric field in a cavity is limited to roughly 100 MV/m, after which the material of the cavity breaks (break down limit) and consequently 2) the physical size required to achieve certain electron energies. The long length requires many additional components to retain the quality of the bunch. For example the European XFEL in Hamburg Germany is 3.4 km long to reach electron energies ~ 17 GeV, or SLAC in Stanford USA is 3km long to reach electron energies up to 14GeV.

	Charge [nC]	Energy [MeV]	Bunch Length [μm]	Emittance [mm mrad]	Repetition Rate [Hz]
DESY E-XFEL [41]	1	8.5-17.5 $\cdot 10^3$	24	1.4	10
SLAC LCSL I [42]	0.02-0.25	2.4-15.4 $\cdot 10^3$	2-50	0.13-0.5	120
SwissFEL [43]	0.01-0.2	2.1-5.8 $\cdot 10^3$	0.75-6	0.18-0.43	100
SACLA [44]	0.2-0.3	4-8 $\cdot 10^3$	6	1	60

Table 1.1: Examples of electron bunch parameters used for FEL radiation in existing (linear) accelerator structures.

The next generation of these structures aim to reduce the costs by using super conducting RF cavities [45]. These allow for a much larger repetition rate of charges, which also leads to more photons produced, and higher field gradients. Another way to reduce the economical and physical footprint is to design the structure in a double-pass configuration: merging a linear- and circular accelerator together such that a bunch traverses the RF cavity twice. The second time the bunch can either be further accelerated, effectively doubling the length of the accelerator, or decelerate and the energy is returned to the cavity (Energy Recovery Linac) [46].

The stability of parameters, high current and brightness justifies the cost of such structures.

1.3.1 MariX

The INFN Milano research group has designed a facility called Marix [1]. The reduction in size of the facility (< 500 [m]) is realized by a two pass LINAC in combination with an arc. The arc consists out of

Chasman-Green lattices (or double bend achromats) [47]. Here the bunch is compressed by a factor of 18 before it reaches the LINAC again to get accelerated a second time and produce radiation through the FEL process. The envisioned repetition rate for the FEL is 1 – 2 MHz, much higher than the current facilities. In the arc the electrons emit synchrotron radiation and, because of the small size of the bunch, a range of the spectrum is emitted coherently. This can deteriorate the quality of the bunch; forming microstructures, increase its volume and increase the energy spread. In the figure below one section of the arc is shown. The focal position in the x plane lies inside the two dipoles. For the first one its close to the entrance, and for the second close to the exit. The 1D solution of the self-fields [22, 23] does not take into account the effect of the focal points. Clearly a higher dimensional analysis of the self-fields would be beneficial.

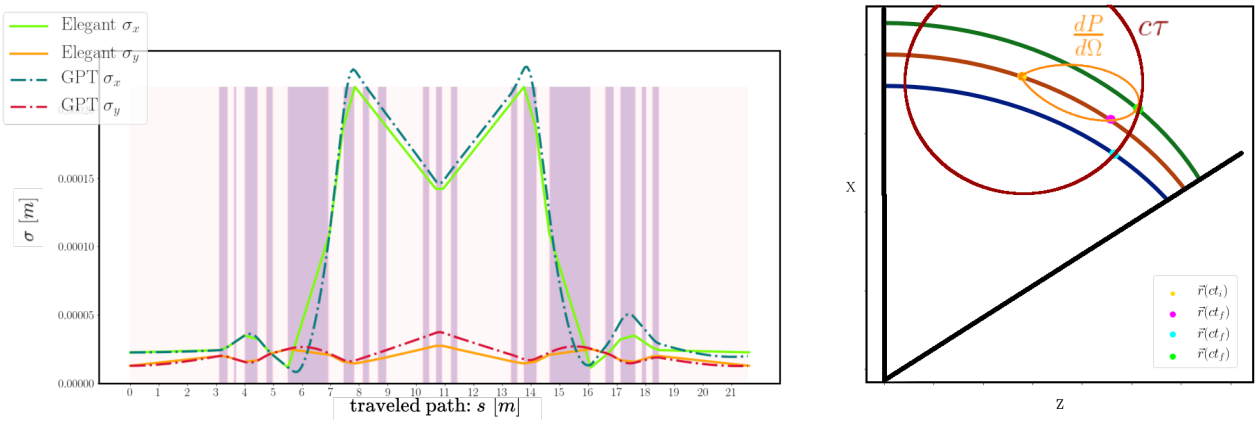

Figure 1.2:
Left: The transport of the electron bunch through one of the double bend achromats, from left to right. The matrix calculation by Elegant [48] performed by M. Rossetti Conti [49]. At the start of my PhD I tried to use GPT [50] to reproduce the as it give a more accurate description of the path of the bunch. What it does show is where that the bunch is focussed (in x) inside both bending magnets.
Right: Exaggerated schematic of how the focussing in the dipole could require a 2D model of the fields.

Plasma Wakefield Accelerators

Plasma wakefield accelerators (PWA) were first proposed in 1979 [51] and the first demonstration of the plasma wake was given in 1985 [52]. The physical principle of the accelerating gradient is as follows: A driver expels the electrons in the plasma, while the heavy positive ions remain quasi static. This creates a very large electric field on the order of 1 – 100 GV/m [53, 54, 55]. The driver can be a high intensity laser pulse (Laser Plasma Acceleration LPA) ($a_0 > 1$ - I>10^{18} W/cm^2) or another charged bunch (Beam driven Plasma Acceleration BPA). There are two ways to produce high energy electron bunches: self-injection where the electrons from the plasma are trapped into a bunch or external injection (i.e. a pre-existing electron bunch which is called a witness).

The attraction of PWA schemes is that the acceleration stage is very short, on the order of cm, and high energy electrons with minimal divergence are generated. The acceleration gradient is not constant, which leads to a relative large energy spread; on the percent to tens of percent level [56, 57, 58, 59]. The current mayor downsides for LPA are the low repetition rate, on the order of Hz, and low energy efficiency of lasers [60]. BPA operate on similar repetition rates (on the macro bunch scale) [61, 55] and require a high energy driver, which is produced in traditional accelerating structures.

	Charge [nC]	Energy [MeV]	Bunch Length [μm]	Divergence / Emittance [μrad] / [mm mrad]	Repetition Rate [Hz]
FACET [62]	$40 \cdot 10^{-3}$	$47 \cdot 10^{3}$	20	75 [μrad]	
SPARC LAB [63]	$20 \cdot 10^{-3}$	93	12	0.9 [mm mrad]	1
[64]	$50 \cdot 10^{-3}$	$2 \cdot 10^{3}$	15	-	0.1
Bella [65]	$5 - 60 \cdot 10^{-3}$	$6 - 7.8 \cdot 10^{3}$			1

Table 1.2: Examples of electron bunch parameters from plasma wakefield accelerators. The following articles give a good overview of other facilities [66] and the direction of research [67].

PWA is still a young research area and many different methods are investigated to improve the quality of the bunch: plasma density modulation [68], energy spread reduction [69], low intensity Multi-pulse LPA [60, 70], circumventing the dephasing by [68, 71], hybrid LPA & BPA [72] etc.

1.4 Motivation

Two fields within the production of synchrotron radiation have been researched: the effect of retarded potentials on a bunch within a bending magnet and Thomson scattering.

Compression of the electron bunch is a key point to improve the efficiency of radiation emission for an FEL. This is achieved in structures consisting of several dipole magnets, like chicanes or double bend achromats, by utilizing the path difference due to the chromaticity of an electron bunch. For example in the proposed facilities like in MariX the bunch is compressed by a factor of 18, from $\sigma_z = 365$ [μm] down to $\sigma_z = 20.6$ [μm] , through a sequence of double bend achromats [49, 1]. As the size of the bunch decreases more of the dipole induced synchrotron radiation is emitted coherently and could lead to detrimental effects [73]. The difficulty to calculate the forces on an electron (or macro-particle) is due to the finite speed of the electromagnetic field and the curved trajectory. The former means that the field acting on an electron originates from a source at a different point in space and time, and therefore the history of the source needs to be stored in numerical simulations. The latter makes a Lorentz transformation to the instantaneous rest frame of the source electron non-viable; it is not an inertial frame. The behaviour of the space-time separation between the source and target have been investigated and analytical solutions developed.

For Compton/Thomson scattering sources it is important to know what the properties are of the laser pulse (e.g. intensity, profile, polarization and carrier envelope phase), since these characteristics are transferred onto the scattered radiation [74, 75] and can influence experimental outcomes [10].

The laser pulse properties depend on its generation and design. To keep things general, a laser pulse can be grouped in two categories: cavity based and chirped pulse amplification (CPA).

Cavities, such as the Fabry-Perot, are used to obtain a monochromatic medium-high intensity laser pulse ($a_0 \sim 10^{-2}; I \sim 10^{14}$ [W/cm^2]). The recirculation of the pulse allows for a high repetition rate of collisions, increasing the yield of emitted radiation. The tremendous amount of power stored can excite higher transverse harmonics through imperfections of the mirrors or deformations caused by heat dissipation. This is detrimental on the stored laser energy, as these modes leak out of the cavity. The effect of such mixed modes from the perspective of the emitted radiation is investigated.

Lasers based on CPA are characterised by very short pulse durations (~ femto-second), and therefore to very high intensities ($a_0 \sim 1 - 10; I \sim 10^{18} - 10^{22}$ [W/cm^2]). For such short pulses the carrier envelope phase becomes an important parameter; does the peak of the envelope match the wave? This dependency has been analytically solved and methods provided on how it can be measured ensuring the right characteristics in further experiments.

The broad bandwidth of a CPA laser, before compression, has another interesting application: compensating an electron bunch's energy distribution. Especially LPA electron bunches have an energy spread in the direction of propagation on the order of few to tens of percent. It can also be interesting for

RF based accelerators, because more charge can be accelerated by allowing for a larger energy spread. By matching the energy spread of the electrons with the chirped pulse the bandwidth of the monochromatic case can be retrieved. This could be interesting for increasing the photon yield by increasing the charge of a bunch by allowing a large energy spread.

1.5 Dissertation Overview

Chapter 2 provides the theoretic background that is collected from textbooks and publications. The modelling of a laser pulse (Section 2.5) is given extra attention as to understand the choices made in the research part. In Chapter 3 we find the research conducted on the interaction between electrons within a bunch, with emphasise on acceleration, from first principles. How charges affect each other becomes more important for beam transport lines where a bunch is compressed. Derivations of the analytical solutions are found in Appendix B. In Chapter 4 contains the research on several topics regarding Thomson scattering. Experimentally determining the laser pulse properties such as its profile and its relative phase. And finally conclusions are given in Chapter 5.

Chapter 2

Theoretical Background

2.1 Choice of Units & Conventions

We already encountered a mix of units in the introduction. This is because the choice of units and notation can make the dynamics of a system more understandable. As the principles of accelerator physics are rooted in classical electrodynamics and special relativity the most fitting notation is to use space-time coordinates (ct, x, y, z) and the cgs (or more precisely the Gaussian) unit system [34, 76, 77, 78], especially when only microscopic particle dynamics in free space are be discussed .

Most of us are very familiar with the SI (also known as MKS) unit system as these are *the* units of all modern engineering. In the SI unit system unit charge is its own base unit. To obtain the right dimension of force due to an electric and/or magnetic field a proportionality constant is required: the permittivity and permeability of free space (In literature denoted as ϵ_0 and μ_0 respectively).

Historically they had great importance, because the reciprocal product of these two quantities gives the theoretical value of the speed of light in vacuum. Since light is an electromagnetic wave and empty space (in the classical framework) is just...empty, and it would be much neater to have these two fields equal each other dimensionally and the proportionality constant be dimensionless. This is in fact what is done in the cgs system: all units are expressed in terms of length (cm), mass (g) and time(s). For example, the unit of charge is given its value and unit through the Coulomb force as $\mathrm{g}^{1/2}\ \mathrm{cm}^{3/2}\ \mathrm{s}^{-1}$. A good read on on this topic is an article by H.G.B. Casimir [79]. The Lorentz force then clearly relates that the magnetic field becomes increasingly important for particle-light interactions when the particles move close to the speed of light

$$F = q(E + \beta \times B) \tag{2.1}$$

since $\beta = \frac{v}{c} \rightarrow 1$. A notation frequently seen in literature is to separate $\partial_0 = \partial_{ct}$ into $\frac{1}{c}\frac{d}{dt}$. Throughout this thesis, wherever the combination ct appears it should be read as an *inseparable quantity*.

2.2 Special Relativity

The convention for the space-time metric used here is

$$g^{\mu\nu} = \begin{pmatrix} 1 & 0 & 0 & 0 \\ 0 & -1 & 0 & 0 \\ 0 & 0 & -1 & 0 \\ 0 & 0 & 0 & -1 \end{pmatrix} \tag{2.2}$$

through which the spacetime interval is given by

$$ds^2 = dX^\mu dX_\mu = dct^2 - d\vec{r}^2 = \frac{dct^2}{\gamma^2} \tag{2.3}$$

where $\gamma = \frac{1}{\sqrt{1-\beta^2}}$ is the Lorentz factor.

$$X_\mu = g_{\mu\nu} X^\nu \tag{2.4}$$

Thus if $X^\mu = (ct, \vec{r})$ then $X_\mu = (ct, -\vec{r})$.
The Lorentz transformation in the z-direction is given by

$$X'^\mu = \begin{pmatrix} \gamma & 0 & 0 & -\gamma\beta \\ 0 & 1 & 0 & 0 \\ 0 & 0 & 1 & 0 \\ -\gamma\beta & 0 & 0 & \gamma \end{pmatrix} X^\mu \tag{2.5}$$

The four-velocity is given by

$$U^\mu \equiv \frac{dX^\mu}{ds} = \gamma \begin{pmatrix} 1 \\ \vec{\beta} \end{pmatrix} \tag{2.6}$$

This choice of the four-velocity results in its magnitude to be $U^\mu U_\mu = 1$. This relation is a powerful tool to find solutions to the motion of a particle, as we will see in section 2.6 and for various solutions in Appendix A.

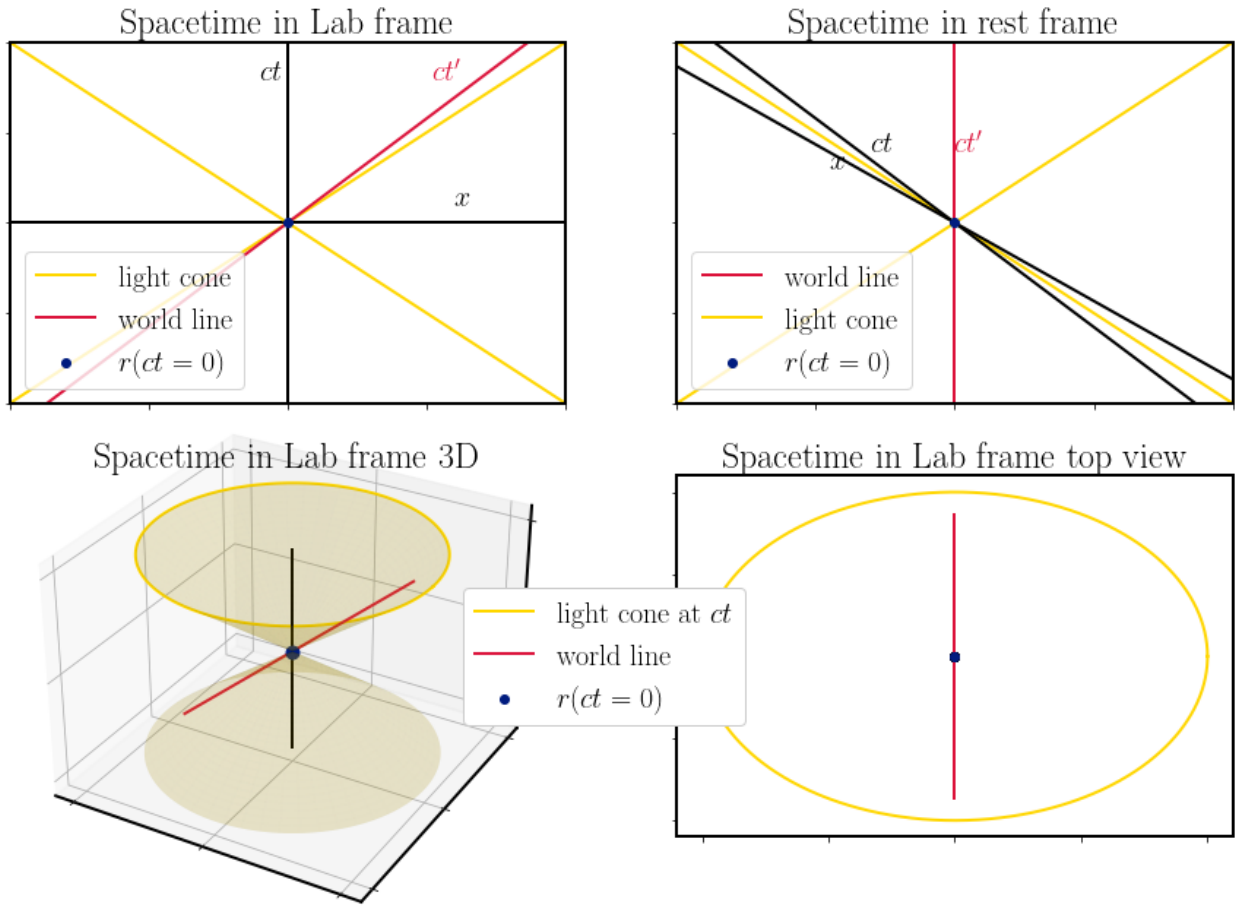

Figure 2.1: Illustrations of space-time diagrams for a particle moving in uniform linear motion.
Top left: Space-time diagram in the labframe. The particle's trajectory in such a diagram is called its world-line (red) and it has always a smaller than 45 degree angle with the time axis as it travels with a speed $\beta < 1$.
Top right: Space-time diagram in the particle's rest frame. Through the Lorentz transformation the time- and space axis of the lab are rotated.
Bottom left: 3D (x, z, ct) representation of the space-time diagram of the labframe.
Bottom right: Top view of the lab frame including the light cone originating from $\vec{r}(ct = 0)$.

2.3 Forces & Emittance

The goal of an accelerator structure is to obtain an electron bunch with specific parameters at an interaction point. During the transport from the source the electron bunch is manipulated with electromagnetic fields. This section provides the dynamics of charged particles in these (external) fields.

2.3.1 Force Equations

Lorentz Force

The acceleration of a charged particle is given by

$$\frac{dU^{\mu}}{ds} = \frac{q}{mc^2} F^{\mu\nu} U_{\nu} \tag{2.7}$$

The electromagnetic field tensor is given by

$$F^{\mu\nu} = \begin{pmatrix} 0 & -E_x & -E_y & -E_z \\ E_x & 0 & -B_z & B_y \\ E_y & B_z & 0 & -B_x \\ E_z & -B_y & B_x & 0 \end{pmatrix} = \partial^\mu A^\nu - \partial^\nu A^\mu \tag{2.8}$$

where E are the electric and B the magnetic components of the field, which can also be expressed as the partial derivatives of the four-vector potential A^μ. In theoretical publications the predominant choice for the fields is A^μ. This can be explained from Lagrangian/Hamiltonian formulation as the canonical momentum of a charge is given by $P - A$(see for example in [34]). Another explanation is found through Maxwell's equations; the wave equation for A^μ is equal to the (four) charge density. Moreover, by using the vector potential the equations of motion for the most well understood interactions have quite elegant solutions, see Appendix A.

Landau Lifshitz

The Lorentz force is not self-consistent as it does not take into account the radiation energy lost by an accelerated particle. This loss of energy can be viewed analogously to a frictions force. This friction force was derived by Lorentz (non-relativistic) and by Abraham (relativistic) and was renormalized by Dirac and hence is called the Lorentz-Abraham-Dirac equation. It is given by

$$\frac{dU^\mu}{ds} = \frac{q}{mc^2} F^{\mu\nu} U_\nu + \frac{2q^2}{3mc^2} F^\mu_{LAD} \tag{2.9}$$

$$F^\mu_{LAD} = \left(\frac{d^2U^\mu}{ds^2} - U^\mu U^\nu \frac{d^2U_\nu}{ds^2} \right) \tag{2.10}$$

The mayor problem with this equation is the so called runaway solutions: a single electron in the *absence* of external fields can self-accelerate (see for example [80] in references therein). This problem can be eliminated by perturbing the Lorentz force: take the derivative of Eq.2.7 with respect to s and substitutes it into Eq. 2.10. The result is the Landau-Lifshitz equation of motion [81].

$$\frac{dU^\mu}{ds} = \frac{q}{mc^2} F^{\mu\nu} U_\nu + \frac{2q^2}{3mc^2} \left(\frac{q}{mc^2} \partial_\gamma F^{\mu\nu} U_\nu U^\gamma + \left(\frac{q}{mc^2} \right)^2 \left(F^{\mu\nu} F_{\nu\beta} U^\beta - F_{\nu\beta} F^{\beta\alpha} U_\alpha U^\nu U^\mu \right) \right) \tag{2.11}$$

Solutions to this equation are sporadic; an electron in a constant magnetic field [82] and in a plane wave laser pules [83, 84, 85].

2.3.2 Emittance

The emittance is a quality factor that describes an electron bunch. There are, as is quite usual in physics, multiple definitions of the emittance: geometric, rms and normalized. The derivation of the emittance originates from the stability analysis of betatron motion, i.e. the oscillating trajectory due to focussing and defocussing quadrupoles, in synchrotrons [86, 87]. For this system the energy spread is negligible, the particles are non-accelerating and different coordinate pairs (e.g. x & y or y & $x' = \frac{dx}{dz}$) are uncoupled. In this case the 2D configuration space occupied by a bunch can be represented by an ellipse and the area of it is proportional to the emittance. Hence it now carries the preposition "geometric" [47].

A more rigorous approach is to start in the 6D phase space [88, 89]. The bunch can be expressed with a distribution function as it obeys the macroscopic limit, i.e. a bunch occupies a small volume (in real space) and contains a large number of particles. The distribution function is then normalized as

$$N_e = \int d^3x \int d^3p\, f(\boldsymbol{x}, \boldsymbol{p}; t) \tag{2.12}$$

Where $\boldsymbol{p} = mc\gamma\vec{\beta}$. If only conservative forces, i.e. forces without a momentum dependence[1] , act on the bunch then Liouville's theorem applies whereby the volume in phase space is a conserved quantity. Therefore one can map the (macro) particles linearly from one point to another in phase space: $f(\boldsymbol{x}(t), \boldsymbol{p}(t); t)$ to $f(\boldsymbol{x}(t'), \boldsymbol{p}(t'); t')$. The (normalized) emittance now can be represented as the determinant of the covariance matrix of the three coordinate pairs:

$$\epsilon^2 = \begin{vmatrix} \langle xx\rangle & \langle xp_x\rangle & \langle xy\rangle & \langle xp_y\rangle & \langle xz\rangle & \langle xp_z\rangle \\ \langle p_x x\rangle & \langle p_x p_x\rangle & \langle p_x y\rangle & \langle p_x p_y\rangle & \langle p_x z\rangle & \langle p_x p_z\rangle \\ \langle yx\rangle & \langle yp_x\rangle & \langle yy\rangle & \langle yp_y\rangle & \langle yz\rangle & \langle yp_z\rangle \\ \langle p_y x\rangle & \langle p_y p_x\rangle & \langle p_y y\rangle & \langle p_y p_y\rangle & \langle p_y z\rangle & \langle p_y p_z\rangle \\ \langle zx\rangle & \langle zp_x\rangle & \langle zy\rangle & \langle zp_y\rangle & \langle zz\rangle & \langle zp_z\rangle \\ \langle p_z x\rangle & \langle p_z p_x\rangle & \langle p_z y\rangle & \langle p_z p_y\rangle & \langle p_z z\rangle & \langle p_z p_z\rangle \end{vmatrix} \tag{2.13}$$

where the variances are given by

$$\langle w^n\rangle = \frac{\int d^3x \int d^3p\, w^n f}{\int d^3x \int d^3p f} \tag{2.14}$$

If the projections of the phase space are uncorrelated, e.g. $\langle xp_y\rangle = 0$, then for each projection an emittance can be calculated which remains constant. For the x-direction the emittance is then given by

$$\epsilon_x^2 = \begin{vmatrix} \langle xx\rangle & \langle xp_x\rangle \\ \langle p_x x\rangle & \langle p_x p_x\rangle \end{vmatrix} \tag{2.15}$$

The three quantities that can change are x, γ and β and thus the factors mc in p can be factored out obtaining the *normalized* emittance (ϵ^N). The relation between the normalized and geometric emittance is given by

$$\epsilon^N{}_x = \langle\gamma\beta\rangle\epsilon_x^G \tag{2.16}$$

Here we see that if the energy of the bunch increases the geometric emittance decreases and is referred to as adiabatic damping [47]. Note that Eq. 2.16 is valid only when the energy spread is small. The brightness is then defined as [89]

$$B_{\text{rightness}} \propto \frac{N}{V_{6D}} = \frac{N}{\epsilon^N{}_x\epsilon^N{}_y\epsilon^N{}_z} \propto \frac{I}{\epsilon^N{}_x\epsilon^N{}_y} \tag{2.17}$$

In short, to have high brightness means that a bunch approximates a single particle better. There is of course a limit to the single particle's emittance, which is given by the Heisenberg uncertainty principle and equates [90]

$$\epsilon^N{}_{x,QM} = \frac{\sqrt{\langle xx\rangle\langle p_x p_x\rangle}}{mc} \leq \frac{\hbar}{2mc} = 1.910^{-13}[\text{m}] \tag{2.18}$$

This limit, however, is far smaller than the practical accuracy required to represent a bunch and therefore the classical approach is justified. In fact, the current limit of emittance is limited by the intrinsic value of a photocathode [91].

2.4 Lienard Wiechert Potentials

There are two ways to view the causality relation which can be explained by taking two charges in space at the current time $r_1(ct)$ and $r_2(ct)$:

1) looking into the history of r_1 to find its time & position $r_1(ct_{ret})$ from which the field travelled to $r_2(ct)$. The time ct_{ret} is the retarded time.

[1] For a time independent magnetic field the force on a particle does depend on its momentum, however it is still a conservative force since $\nabla \times F \propto \nabla \times (\beta \times \vec{B}) \propto \frac{d\vec{B}}{dct} = 0$. Which is good since transport lines of accelerators consist out of time independent magnets.

2) looking into the future of r_1 to find its time & position $r_1(ct_{adv})$ to where the field travels from $r_2(ct)$ The time ct_{adv} is the advanced time.
Though both views are equally valid, from a numerical point of view the retarded time is preferential because the trajectory is known up to the current time and we are left with calculating the forces on the observer.

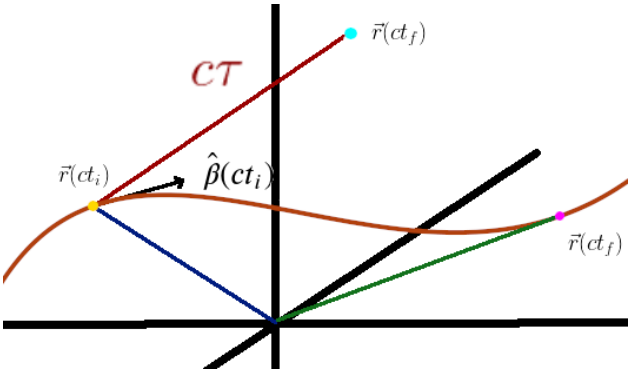

Figure 2.2: Schematics of retarded time. $\vec{r}(ct_i)$ and $\hat{\beta}(ct_i)$ represents the position and velocity respectively of the particle at the retarded time.

The retarded fields can be derived from the wave equation of A^μ and involves the use of Green's functions [34]. The solution is given by

$$A^\mu_{LW} = \frac{e}{\gamma c\tau(1-\hat{n}\cdot\vec{\beta})} U^\mu \Big|_{ct_{ret}}, \tag{2.19}$$

where $c\tau$ is the distance the field has travelled and $\hat{n}$ is the unit vector of $c\tau$, and the quantities on the right hand side are to be taken at the retarded time. The common way in literature to represent the retarded time is (e.g. [34])

$$ct_{ret} = ct - |\vec{r}_o(ct) - \vec{r}_s(ct_{ret})|. \tag{2.20}$$

The electric field is then found by taking the derivative with the space-time coordinate of Eq. 2.19 and results in

$$\vec{E}(ct,\vec{r}_o) = e\left(\frac{\hat{n}-\vec{\beta}_s}{\gamma^2 c\tau^2\left(1-\hat{n}\cdot\vec{\beta}_s\right)^3} + \frac{\hat{n}\times\left(\left(\hat{n}-\vec{\beta}_s\right)\times\dot{\vec{\beta}}\right)}{c\tau\left(1-\hat{n}\cdot\vec{\beta}_s\right)^3}\right)_{ct_{ret}}, \tag{2.21}$$

They are the Coulomb and the radiation field of the field. The magnetic field can be derived in a similar way giving $\vec{B} = \hat{n}\times\vec{E}$.

2.4.1 Radiation

To obtain the radiation emitted only the accelerative part of Eq. 2.21 needs to be taken into account. We want to know what the energy and frequency content is in a certain direction. For this we take the far field approximation; the unit vector $\hat{n}$ does not change during the electron's acceleration and encloses a sphere around a chosen origin. Then the radiated energy per unit frequency and sterradian is given by [34]

$$\frac{d^2I}{d\omega d\Omega} = \frac{e^2}{4\pi^2 c}\left|\int_{-\infty}^{\infty} dct \frac{\hat{n}\times\left(\left(\hat{n}-\vec{\beta}\right)\times\dot{\vec{\beta}}\right)}{\left(1-\hat{n}\cdot\vec{\beta}\right)^2}\exp\left[i\frac{\omega}{c}(ct-\hat{n}\cdot\vec{r})\right]\right|^2 \tag{2.22}$$

Which can be integrated by parts and gives (probably the better known) relation

$$\frac{d^2I}{d\omega d\Omega} = \frac{e^2}{4\pi^2 c}\left|\frac{\omega}{c}\int_{-\infty}^{\infty} dct\hat{n}\times\hat{n}\times\vec{\beta}\exp\left[i\frac{\omega}{c}(ct-\hat{n}\cdot\vec{r})\right]\right|^2 \tag{2.23}$$

2.4.1.1 Many particles & Coherency

Eq. 2.23 is valid for a single electron. To obtain the radiation from many particles is simply the summation of the retarded fields of each particle:

$$\frac{d^2I}{d\omega d\Omega} = \frac{e^2}{4\pi^2 c}\left|\sum_m^{N_e}\frac{\omega}{c}\int_{-\infty}^{\infty} dct\hat{n}\times\hat{n}\times\vec{\beta}_m\exp\left[i\frac{\omega}{c}(ct-\hat{n}\cdot\vec{r}_m)\right]\right|^2 \tag{2.24}$$

For N_e electrons following the same trajectory the product $\hat{n}\cdot\vec{r}_m$ only differs in a phase depending on the initial position [92, 93]. Now, because of the absolute square the sum of exponents can be read as a matrix as shown below

$$\left|\sum_m^{N_e}\exp i\frac{\omega}{c}\hat{n}\cdot\vec{r}_m(0)\right|^2 = \begin{vmatrix} 1 & \exp[i\frac{\omega}{c}\delta_{1,2}] & \dots & \exp[i\frac{\omega}{c}\delta_{1,N_e}] \\ \exp[-i\frac{\omega}{c}\delta_{1,2}] & 1 & & \\ \vdots & & \ddots & \\ \exp[i\frac{\omega}{c}\delta_{1,N_e}] & & & 1 \end{vmatrix} \tag{2.25}$$

where for the answer to Eq. 2.24 all elements of the matrix are summed together. The diagonal terms represent the so called incoherent radiation; each particle radiates independently. If the particles are randomly distributed, with the wavelength being smaller than the size of the bunch, the sum of the other entries of the matrix average to zero. When the bunch size is decreased to half the emitted wavelength the bunch starts to emit coherently [93]. For a single wavelength this is shown in Figure 2.3. The smaller the size of the bunch, as compared to the emitted wavelength, the more they can be represented as a single particle with charge eN_e [23]. A note must be added that here, from the field point of view, we have described constructive interference. In fact the distribution of particles can also be chosen such that the fields interfere destructively in the direction of an observer.

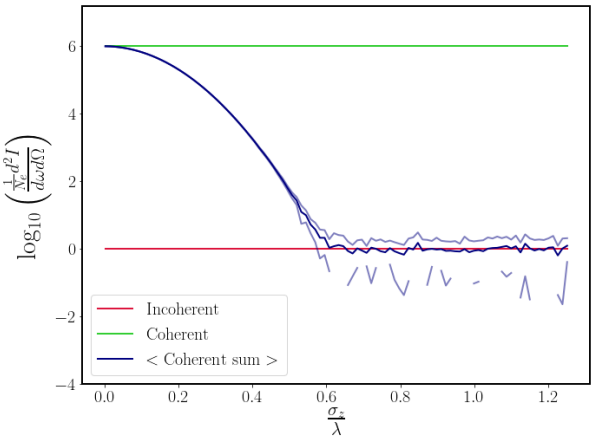

Figure 2.3: Energy observed by in a single angle in the far field from N_e radiating particles. The particle density is given by a 1D Gaussian profile along its propagation direction, with $N_e = 10^6$ particles randomly sampled. The coherency matrix (Eq, 2.25) is calculated for a single frequency 20 times per σ_z. The average of these tends to the incoherent limit when the wavelength is short compared to the bunch length. It has a large spread (rms in light blue lines), because of the random sampling. When the length is comparable to half the emitted wavelength the radiation starts to be coherent.

In the incoherent limit it therefore suffices to calculate the spectrum with

$$\frac{d^2I}{d\omega d\Omega} = \frac{e^2}{4\pi^2 c}\sum_m^{N_e}\left|\frac{\omega}{c}\int_{-\infty}^{\infty} dct\ \hat{n}\times\hat{n}\times\vec{\beta}_m \exp\left[i\frac{\omega}{c}(ct-\hat{n}\cdot\vec{r}_m)\right]\right|^2 \tag{2.26}$$

2.5 Laser Pulse

The following sections are written to form a consistent overview of laser pulse shapes that obey the Maxwell's equations together with the pulse properties such as the energy-field amplitude relations, wavelength scale pulse lengths and frequency modulation (chirp). This is important to correctly model interactions between fields and particles, especially when a Maxwell solver is used for the evolution of the field, because of the numerical dispersion caused by the discretization of spacetime [94]. For the comparison of different laser profiles it is important that the intensity (a_0) and energy are approximately equal, since a_0 determines the electron dynamics (see Section 2.6.2 or A.5) and the energy correlates the total number of photons emitted. For a field propagating in vacuum the wave equation is given by

$$\Box\vec{A} = \partial_\alpha\partial^\alpha\vec{A} = \left(\partial_{ct}^2 - \nabla^2\right)\vec{A} = 0, \tag{2.27}$$

together with the Lorenz gauge

$$\partial_\alpha A^\alpha = \partial_{ct}\phi - \nabla\cdot\vec{A} = 0. \tag{2.28}$$

To convert the vector potential to the electric and magnetic fields the following Maxwell equations are used

$$\vec{E} = -\nabla\phi - \partial_{ct}\vec{A}, \tag{2.29}$$

$$\vec{B} = \nabla\times\vec{A}. \tag{2.30}$$

The amplitude relations between the vector potential and the electric/magnetic field is

$$E_0 = B_0 = A_0 k \tag{2.31}$$

2.5.1 1+1D

Here we take the convention that a wave is travelling in $+\hat{z}$, and therefore $A^\mu = A^\mu(ct,z)$. Substitution in Eq. 2.28 tells us that the only solution is a plane wave with either linear ($A^1 \neq 0$) or circular ($A^1 \neq 0$ and $A^2 \neq 0$) polarization. Using the spatial and temporal Fourier Transform of our vector potential and substitution gives us the vacuum dispersion $\left(\frac{\omega}{c}\right)^2 = k^2$. The consequence is that for one a plane wave can be described by a scalar field and, moreover, any temporal profile is allowed for a plane wave of the form $A(k(ct-z)) = A(\zeta)$. Moreover, a pulse that has a changing phase of the form $\eta(\zeta)$, i.e. chirp, also obeys the Maxwell equations. For several pulse shapes, the temporal profile is shown in Figure 2.4. Throughout this thesis the convention is used that the FWHM of the pulse is equal to a integer value of the wavelength ($FWHM = \lambda_l N_c$).

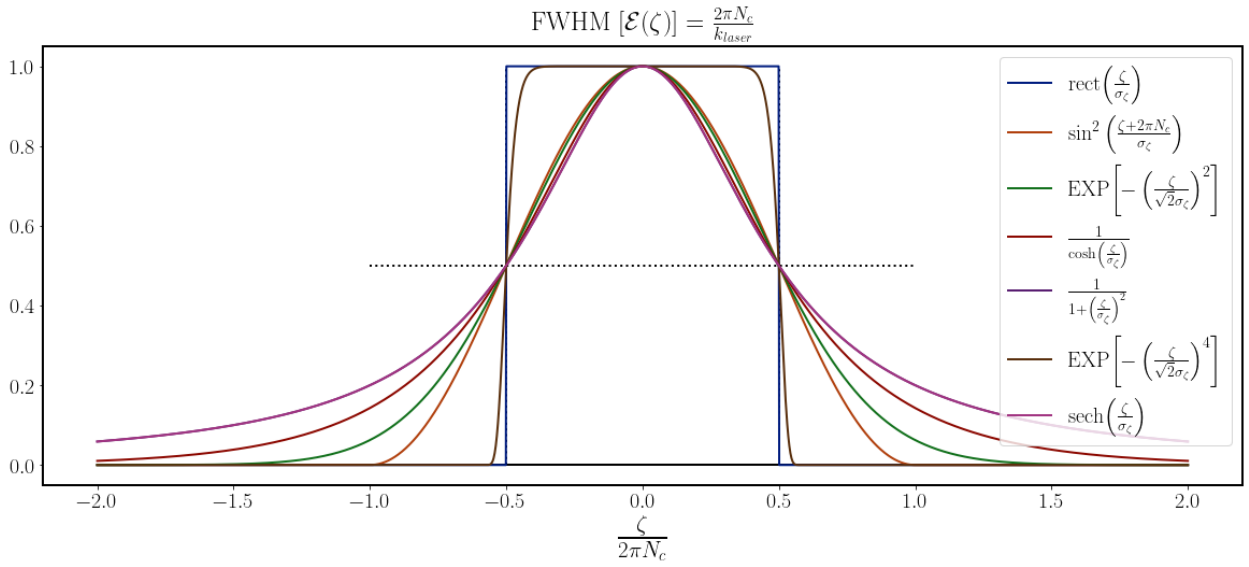

Figure 2.4: Temporal profiles for a 1+1D laser pulse. The wave equation puts no constraint on the shape of a plane wave travelling in vacuum.

2.5.2 3+1D

The solution for A^μ for a 3+1D pulse, i.e. spatial and temporal profiles, we look for solutions for which a volume of electromagnetic energy changes during its propagation, where the volume remains close to the propagation axis: paraxial approximation.

For the derivation of A^μ I recommend the works of K. T. McDonald [95] that have been a great source. Here we start with a scalar field of the form $A = A_0\Psi(\vec{r})\mathcal{E}(\zeta)e^{i\zeta}$ to be read as spatial- and temporal profile and the phase. Substitution in to Eq. 2.27 leads to

$$\Psi(\partial_{ct}^2 - \partial_z^2)\mathcal{E}e^{i\zeta} + \mathcal{E}e^{i\zeta}(-\nabla^2\Psi) + 2\partial_z\Psi\partial_z\mathcal{E}e^{i\zeta} = 0 \tag{2.32}$$

The first part of the equation is recognized as the plane wave (1+1D) solution and therefore equals zero. The last term can be rewritten to $\partial_z\Psi\left(1 - i\frac{\partial_\zeta\mathcal{E}}{\mathcal{E}}\right)$, where the slowly varying amplitude (SVA) approximation can be used. In [95] it is noted that for pulse shapes like the Gaussian profile ($\frac{\partial_\zeta\mathcal{E}}{\mathcal{E}} = \frac{\zeta}{\sigma_\zeta^2}$) this condition is not met. However, when looking more closely there is a distinction to be made between "short", that is the length of the pulse is comparable to its wavelength, and "long" pulses. For example, when taking the limit of the duration to infinite the wave equation does permit such a pulse shape. In Figure 2.5 the ratio for various pulse lengths are given for three pulse shapes often used in literature. We see that the Gaussian profile can be used when the FWHM pulse length is equal or longer than 50 times its wavelength.

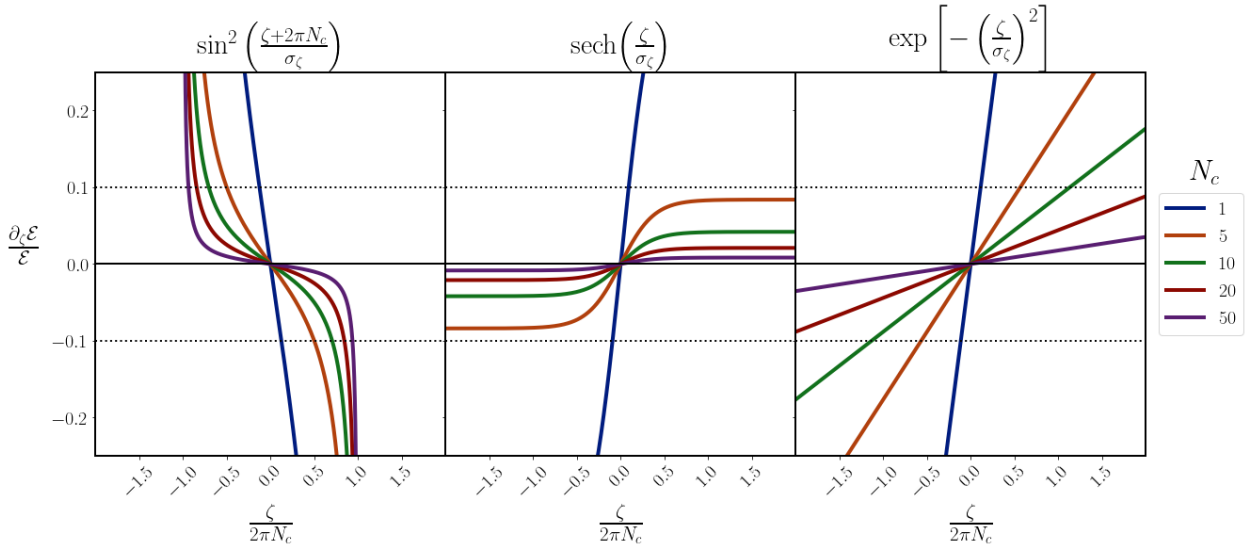

Figure 2.5: To obey the wave equation the condition $\frac{\partial_z \mathscr{E}}{\mathscr{E}} \ll 1$ needs to be fulfilled.

A solution of Ψ can be derived from Eq. 2.32, under the slowly varying envelope approximation for $\mathscr{E}$. One of which is the Gaussian beam [96, 97], given by

$$\Psi = \frac{q_0}{q(z)} \exp\left[-ik\frac{x^2+y^2}{2q(z)}\right], \tag{2.33}$$

where $q_0 = \frac{kW_0^2}{2}$ is the Rayleigh length and $q(z) = z + iq_0$. To find the full solution for A^μ we use Eq. 2.28 to find all its components. The component $A^3 = 0$, since the pulse travels in $+\hat{z}$. Thus to obey the Lorentz gauge the electric potential (ϕ) cannot be zero. A solution can be found by making the ansatz $\phi = A_0 f(\vec{r})\mathscr{E}(\zeta)e^{i\zeta}$. Giving us, within the SVA approximation, the relation

$$ik\phi = -\partial_x A_x - \partial_y A_y \tag{2.34}$$

$$\phi = -A_0 k \frac{i}{k^2}\left(\partial_x \Psi + i\partial_y \Psi\right)\mathscr{E}e^{i\zeta}. \tag{2.35}$$

Here we used the amplitude of the electric field in anticipation. To conclude the (four) vector potential for a linearly polarized laser pulse is given by

$$A^\mu = A_0 \Psi(\vec{r})\mathscr{E}(\zeta)e^{i\zeta}\begin{pmatrix} \frac{x}{q(z)} \\ 1 \\ 0 \\ 0 \end{pmatrix} \tag{2.36}$$

and for a circularly polarized by

$$A^\mu = A_0 \Psi(\vec{r})\mathscr{E}(\zeta)e^{i\zeta}\begin{pmatrix} \frac{x}{q(z)} - i\frac{y}{q(z)} \\ 1 \\ i \\ 0 \end{pmatrix} \tag{2.37}$$

Many also use the electric and magnetic field to describe the laser pulse, therefore here the approximations for them are given too. To start with the electric field for a linearly polarized laser pulse we find

$$\vec{E} = -\nabla\phi - \partial_{ct}\vec{A} \tag{2.38}$$

$$= A_0 k \begin{pmatrix} \frac{i}{k^2}\partial_x\partial_x\Psi \\ \frac{i}{k^2}\partial_y\partial_x\Psi \\ \frac{i}{k^2}\partial_z\partial_x\Psi \end{pmatrix} \mathscr{E} e^{i\zeta} + ikA_0\Psi\mathscr{E} e^{i\zeta} \begin{pmatrix} 0 \\ 0 \\ 1 \end{pmatrix} \tag{2.39}$$

$$\approx A_0 k\Psi\mathscr{E} i e^{i\zeta} \begin{pmatrix} -1 \\ 0 \\ \frac{x}{q(z)} \end{pmatrix} \tag{2.40}$$

and for the magnetic field

$$\vec{B} = \nabla \times \vec{A} \tag{2.41}$$

$$= A_0 k \begin{pmatrix} 0 \\ \frac{\partial_z\Psi}{k} + \Psi \\ \partial_y\Psi \end{pmatrix} \mathscr{E} e^{i\zeta} \tag{2.42}$$

$$\approx A_0 k\Psi\mathscr{E} i e^{i\zeta} \begin{pmatrix} 0 \\ -1 \\ \frac{-y}{q(z)} \end{pmatrix} \tag{2.43}$$

2.5.3 Relating a_0, N_c & Energy

To calculate the energy of an electromagnetic wave one needs to start with the Poynting vector: the energy flux, i.e. the energy transfer per unit area and per unit of time out of a volume (V), and is given by

$$\vec{S} = \frac{c}{4\pi}\vec{E} \times \vec{B} \tag{2.44}$$

The units of the Poynting vector are $\left[\frac{\text{erg}}{\text{s cm}^2}\right]$ (or $\left[\frac{\text{W}}{\text{cm}^2}\right]$ in SI units). Substitution of Eq. 2.40 and 2.43, after taking the real part, gives us

$$\vec{S} = \frac{c}{4\pi}(A_0 k\Psi\mathscr{E})^2 \sin^2(\zeta) \begin{pmatrix} \frac{x}{q(z)} \\ \frac{y}{q(z)} \\ 1 \end{pmatrix} \tag{2.45}$$

Appreciate that $\vec{S}$ shows the divergence of the Gaussian beam.
In the absence of charges the energy within V is related to the Poynting vector as

$$\frac{\partial}{\partial t}\text{Energy} = -\int_V dV\, \nabla\cdot\vec{S} = -\int_A \vec{dA}\, \vec{S} \tag{2.46}$$

Here A is the area, no to confuse it with the vector potential!

To calculate the energy of the pulse we place a screen (A) in the focus ($z = 0$), where the volume encompasses the negative part of $\hat{z}$. The energy of the laser pulse is then simply the energy leaving this volume (since the pulse travels in $+\hat{z}$).

$$\text{Energy}_{\text{laser}} = \int_{-\infty}^{\infty} dt \int_{-\infty}^{\infty} dx \int_{-\infty}^{\infty} dy \frac{c}{4\pi}(A_0 k\Psi\mathscr{E})^2 \sin^2(\zeta)|_{z=0} \tag{2.47}$$

Often in literature ([97]) it is said that the time average of the equation above needs to be taken, as tern $\left(\text{from the square of the sine, } \int d\zeta\mathscr{E}^2(\zeta)\cos(2\zeta)\right)$ is not measurable. This is only the case for infinite waves ($\mathscr{E} = 1$) as for laser pulses with finite length this part of the integral equals zero. Note that for a circularly polarized laser pulse contains twice the energy of a linearly polarized one (as there is no sine squared

term in the equation above). This can be understood from the fact the a circularly polarized laser pulse consists out of two orthogonal linearly polarized components. and we arrive at

$$\text{Energy}_{\text{laser}} = \frac{c}{4\pi}(A_0 k)^2 \int_{-\infty}^{\infty} dx \int_{-\infty}^{\infty} dy \Psi^2|_{z=0} \int_{-\infty}^{\infty} d\zeta \frac{\mathscr{E}^2}{2k}|_{z=0} \tag{2.48}$$

$$\text{Energy}_{\text{laser}} = \frac{c}{4\pi}(A_0 k)^2 \frac{\pi W_0^2}{2} \frac{\sigma_\zeta}{ck} \frac{f_{\mathscr{E}}}{2} \tag{2.49}$$

where $f_{\mathscr{E}}$ is the form factor of the laser pulse. The $\frac{\sigma_\zeta}{ck}$ has the unit of time and can be replaced by the FWHM σ_t. Thus the energy-a_0 relation becomes

$$a_{0,\text{linear}} = \frac{q}{mc^2}\sqrt{\frac{c}{4\pi}}\frac{\lambda}{2\pi}\sqrt{\frac{2\text{Energy}_{\text{laser}}}{\frac{\pi W_0^2}{2}\sigma_t f_{\mathscr{E}}}} \tag{2.50}$$

$$a_{0,\text{circular}} = \frac{q}{mc^2}\sqrt{\frac{c}{4\pi}}\frac{\lambda}{2\pi}\sqrt{\frac{\text{Energy}_{\text{laser}}}{\frac{\pi W_0^2}{2}\sigma_t f_{\mathscr{E}}}} \tag{2.51}$$

By having chosen the pulse length in FWHM the difference in a_0 given a pulse energy and length are negligible, see Table 2.1. This is crucial for the comparison of pulse shape effects in Thomson scattering and will be further discussed in Section 4.5. Finally we can also define a_0 through the peak intensity

$$a_{0,\text{linear}} = \frac{q}{mc^2}\sqrt{\frac{c}{4\pi}}\frac{\lambda}{2\pi}\sqrt{2I_{\text{peak}}} \tag{2.52}$$

$$= 0.85\lambda[\mu\text{m}]\sqrt{\frac{I_{\text{peak}}[\frac{\text{W}}{\text{cm}^2}]}{10^{18}}}$$

$$a_{0,\text{circular}} = \frac{q}{mc^2}\sqrt{\frac{c}{4\pi}}\frac{\lambda}{2\pi}\sqrt{I_{\text{peak}}} \tag{2.53}$$

$$= 0.60\lambda[\mu\text{m}]\sqrt{\frac{I_{\text{peak}}[\frac{\text{W}}{\text{cm}^2}]}{10^{18}}} \tag{2.54}$$

Energy = 10^{-3} [Joule], $\sigma_{t,FWHM}$ = 17.8 [fs], W_0 = 30 [μm]		
	a_0	
	Linear	Circular
rect	$7.63 \cdot 10^{-2}$	$5.40 \cdot 10^{-2}$
$\sin^2$	$7.03 \cdot 10^{-2}$	$4.97 \cdot 10^{-2}$
Gauss	$7.02 \cdot 10^{-2}$	$4.96 \cdot 10^{-2}$
sech	$6.99 \cdot 10^{-2}$	$4.94 \cdot 10^{-2}$

Table 2.1: Values of a_0 for a given energy and pulse length for the profiles discussed in Section 2.5.2.

2.6 Radiation from Scattering

In this thesis the scattering process is treated classically. To understand the limits of this description we will first look at the different models, starting with the more general quantum description. After having established the model, the analytical solutions of Thomson scattering are given.

2.6.1 Energy Regimes & Models

There are two ways to describe the collision between a laser pulse and an electron bunch:

1. Collision between photons and electrons as if they are billiard balls. This is the quantum picture and here the energy and momentum are conserved.

2. The electron rides an electromagnetic wave and emits continuously. This is the classical picture.

To start off with the quantum picture: the energy-momentum balance is given by

$$mcU^{\mu} + \hbar K^{\mu} = mcU'^{\mu} + \hbar K'^{\mu} \tag{2.55}$$

The frequency of the scattered photon, for a head on collision, is given by

$$\omega' = \frac{\omega_l(1+\beta)}{1-\beta\cos(\vartheta) + \frac{\hbar\omega_l}{\gamma mc^2}(1+\cos(\vartheta))} \tag{2.56}$$

where ϑ is the azimuthal angle. The ratio energy of the laser and electron, i.e. $\frac{\hbar\omega_l}{\gamma mc^2}$, in the rest frame of the electron is called the recoil parameter and is given by

$$\chi = 2\frac{\hbar\gamma(1+\beta)\omega_l}{mc^2} \approx 4\frac{\hbar\gamma\omega_l}{mc^2} \tag{2.57}$$

This parameter determines if the scattering needs to be treated quantum mechanically: if the energy of the photon in the rest frame is comparable to the rest mass of the electron then the energy exchange is substantial. For an optical-infra red laser the photons have an energy ~ 1 eV, meaning that the recoil is negligible for electrons up to GeV energies.

Thus far only a single photon-electron scattering has been described. As aforementioned, when $a_0 \sim 1$ an electron can scatter with several photons and converting it to a single emitted one: higher harmonics. The recoil then needs a correction with the harmonic number $\chi_n = n\chi$. In [98, 99] is shown that for $\gamma \leq 100$ the harmonics the recoil due to multi photon scattering does not influence the spectrum significantly and the spacing of the harmonics remain equidistant.

A further distinction must be made in the classical regime, namely for *long* pulses as the energy loss of the electron during the entire interaction needs to be into account. For this one can use the Landau-lifshitz equation (Eq. 2.11). Analytical solutions to the motion [84, 83, 85] have given this criteria: $2\gamma\frac{\omega_l}{c}\frac{2r_e}{3}a_0^2 N_c \ll 1$.

Figure 2.6 shows the scaling laws as function of a_0 and γ for two laser pulses with different wavelength and temporal length. Note that the lines indicate where the relevant parameter has reached a value of 0.01, but clearly it is not a hard border. For example in [100] it was shown that for the ELI facility [101] $\chi \approx 0.02$ already requires the quantum model.

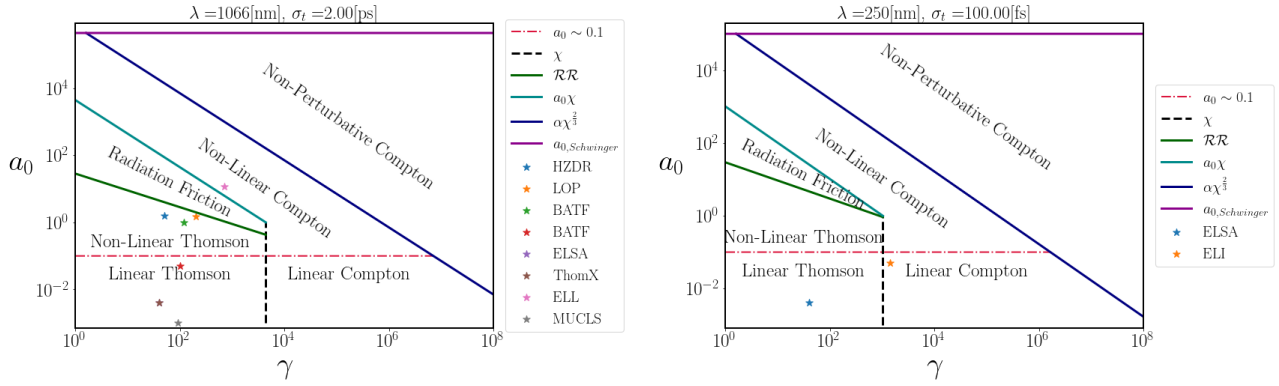

Figure 2.6: Schematic overview of the different models to describe the scattering between electrons and a laser pulse. The lines indicate where the relevant parameter has a value of 0.01, and are not hard boundaries. The Linear, Non-linear Thomson and Radiation Reaction [84, 83, 85] regimes are classical, where the electron emits continuously according to Maxwell's equations. The Compton regimes [27] are quantum mechanical in nature, where for the Non-perturbative regime additional corrections are necessary [27, 102]. The figures include facilities and have been added to the nearest wavelength.
Left: Regimes are calculated with $\lambda_l = 1.066\mu$m, $\sigma_t = 7$ps. HZDR [103], LOP [104], BATF [105], LBNL [106], SPARC [107], THomX [108], ELL [109], MUCLS [7].
Right: For $\lambda_l = 250$nm, $\sigma_t = 10$ps. ELSA [110], ELI [100].

To summarize, the classical model can be used for short infra-red laser pulses up to moderate levels of a_0 and electron energies up to GeV. This model teaches us some very interesting dynamics as we will see in the following sections, and can be found in many publications for example [111, 29, 112, 113, 114, 99] and tools with which we can alter the behaviour of the spectrum.

2.6.2 Analytical Solutions of Thomson Scattering

The motion and trajectory of an electron interacting with a laser pulse is analytically solvable in the plane wave approximation, i.e. $\Psi(\vec{r}) = 1$ or transverse ponderomotive forces are negligible. The derivation of the velocity can be found in Appendix A.5 (see also [112] and references therein) and is given by

$$U^\mu = \begin{pmatrix} \gamma + \frac{(a)^2}{2}(1-\beta)\gamma \\ a^1 \\ a^2 \\ -\gamma\beta + \frac{(a)^2}{2}(1-\beta)\gamma \end{pmatrix}, \tag{2.58}$$

where $(a)^2 = -a_\mu a^\mu$ is the magnitude of the vector potential. This equation is valid for any frame of reference, since ζ is a Lorentz invariant. Only when obtaining the trajectory it is important to remember that the integration constant $k\gamma(1+\beta)$ is a frame dependent quantity.

The spectral equation Eq. 2.23 can be rewritten in terms of ζ (the (monochromatic) laser phase), since the motion is fully described by it. Moreover, the terms in the exponential can be rewritten as an integral of the four-velocities with respect to ζ: $ct - \hat{n}\cdot\vec{r} = \int_{-\infty}^{s} ds' U^0 - \hat{n}\cdot\vec{U} = \int_{-\infty}^{\zeta} d\zeta' \frac{U^0 - \hat{n}\cdot\vec{U}}{k\gamma(1+\beta)}$. Thus the double differential in terms of the laser phase is given by

$$\frac{d^2 I}{d\omega d\Omega} = \frac{e^2}{4\pi^2 c}\left|\nu\gamma(1+\beta)\int_{-\infty}^{\infty} d\zeta\, \hat{n}\times\hat{n}\times\vec{U}\exp\left[i\nu\gamma(1+\beta)\int_{-\infty}^{\zeta} d\zeta' U^0 - \hat{n}\cdot\vec{U}\right]\right|^2, \tag{2.59}$$

where $\nu = \frac{\omega}{\omega_{l,0}}\frac{1}{\gamma^2(1+\beta)^2}$.

Several authors published the full solutions to the previous equation [29, 85], but here we will focus only on the backscattered radiation ($\vartheta = \pi$) for a linearly polarized laser pulse as this gives us enough

insight to the physics behind the dynamics of the scattering process. In Appendix C a more detailed derivation can be found and includes also the circularly polarized laser pulse. For the back-scattered radiation the integral of Eq. 2.59 is

$$\begin{aligned} &\int d\zeta U^1 \exp\left[i\nu\gamma(1+\beta)\int_{-\infty}^{\zeta} d\zeta' U^0 + U^3 \right] \\ &= \int d\zeta\, a_0 \mathscr{E}(\zeta) \exp[i\eta(\zeta)] \exp\left[i\nu \int_{-\infty}^{\zeta} d\zeta' 1 + (a)^2 \right] \end{aligned} \tag{2.60}$$

The slowly varying amplitude approximation and Jacobi-Anger expansion are used to extract the oscillating part of $(a)^2$ out of the exponent. This expansion moves the stationary phase points from the imaginary axis to the real one [31, 32], and more over already tells us the existence of (spherical) harmonics in the spectrum. Combining the remaining exponents results in

$$\begin{aligned} &\exp[i\eta(\zeta)(2m+1) + i\nu\int_{-\infty}^{\zeta} d\zeta' 1 + \tfrac{a_0^2\mathscr{E}^2(\zeta')}{2}] \\ &= \exp[i\int_{-\infty}^{\zeta} d\zeta' \tfrac{\partial\eta(\zeta')}{\partial\zeta'}(2m+1) + \nu(1+\tfrac{a_0^2\mathscr{E}^2(\zeta')}{2})] \end{aligned} \tag{2.61}$$

Now the stationary phase approximation can be used and we find that the frequencies emitted are given by

$$\nu = \frac{\partial\eta(\zeta')}{\partial\zeta'} \frac{(2m+1)}{1+\frac{a_0^2\mathscr{E}^2(\zeta')}{2}} \tag{2.62}$$

Figure 2.7 shows the dynamics of the of the emission of the radiation during the interaction process for both polarization states of a laser pulse without chirp ($\eta = \zeta$). The electron experiences the ponderomotive force in the longitudinal direction, decreasing its velocity, and consequently the emitted frequency reduces in magnitude; which is the non-linear broadening effect. Moreover, each frequency is emitted twice during the interaction, leading to subsidiary peaks due to interference in the spectrum as shown in Figure 2.8 [115].

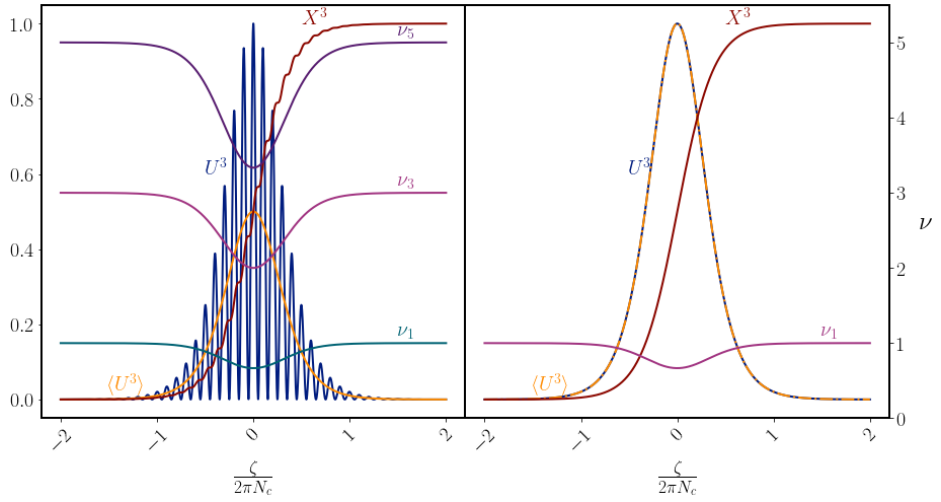

Figure 2.7: Dynamics of Thomson scattering for a head-on collision between an electron and a quasi-monochromatic plane wave laser pulse ($\eta = \zeta$). The graphs show the velocity (U^3), drift velocity ($\langle U^3 \rangle$) of the particle and the frequency emitted during the interaction (ν). The drift velocity causes a Doppler shift in the spectrum, and since it depends on $(a)^2$ it is called the non-linear broadening of the spectrum. The spectrum can be understood as the interference between a frequency emitted at two different points in space-time.
Left: Linearly polarized laser pulse. The electron not only oscillates in the transverse direction but also in the direction of propagation at twice the laser frequency. This causes the emission of higher harmonics.
Right: Circularly polarized laser pulse. On-axis there are no emission of harmonics.

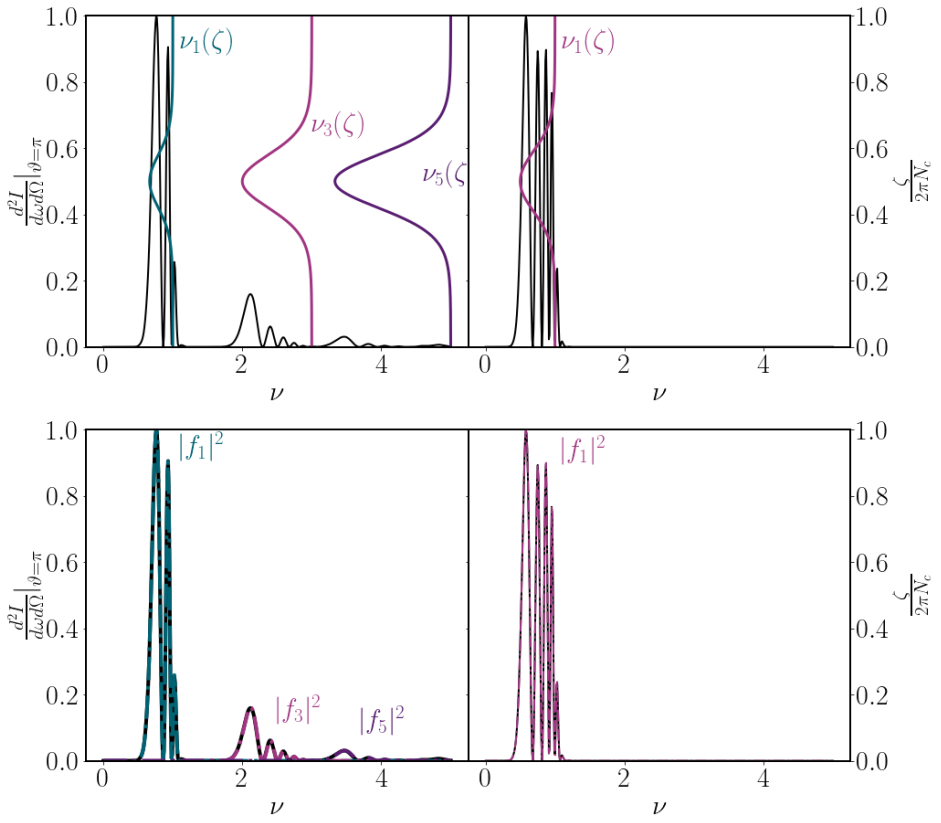

Figure 2.8: On-axis (Thomson) spectrum for a single electron colliding head-on with a laser pulse with $a_0 = 1$. The frequency for which the intensity of a harmonic is maximal can be approximated with the minimum of the frequency curve (Eq. 2.62).
Top left: Spectrum for a linearly polarized laser pulse including the frequency relation.
Bottom left: Spectrum for a linearly polarized laser pulse and the analytical solution of Eq. C.13 integrated numerically for each harmonic.
Top right: Spectrum for a circularly polarized laser pulse including the frequency relation.
Bottom right: Spectrum for a circularly polarized laser pulse.

Although the on-axis radiation gives the most simple analytical solutions it must be noted that here there is actually no radiation emitted. As the solid angle $d\Omega = d\varphi \sin(\vartheta) d\vartheta$ the sine term forces the double differential to zero.

The angular distribution can be obtained by a small angle approximation, since most of the radiation will be emitted close to the propagation direction of the electron. Similar steps must be taken for Eq. 2.60 but with $U^0 - \cos(\vartheta)U^3$ substituted. This leads to

$$\nu_1 = \frac{1}{1 + \gamma^2(\pi - \vartheta)^2 + \langle (a)^2 \rangle} \tag{2.63}$$

Here we see that the Lorentz factor of the electron gives rise to a Doppler shift. In fact if one makes a Lorentz transformation, for a Linear Thomson system, to the initial rest frame the electron one finds the frequency is the same in all directions.

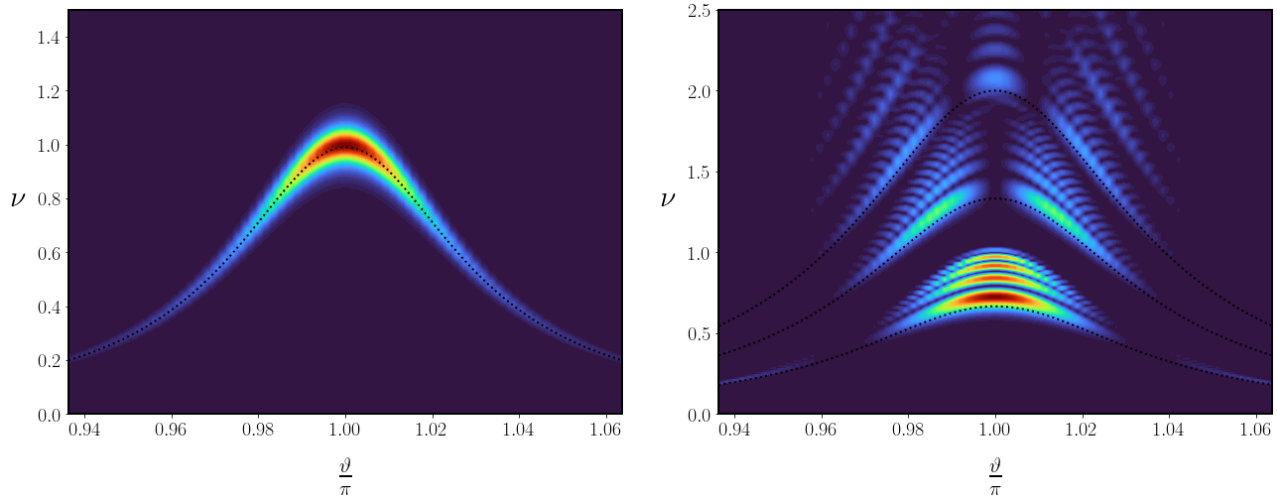

Figure 2.9: $\frac{d^2I}{d\omega d\Omega}$ as function of frequency and (azimuthal) observation angle for electron energy $\gamma = 10$ and a linearly polarized laser pulse with a sech longitudinal profile with length $N_c = 10$. The black dotted line is given by Eq. 2.63. Note that $d\Omega = d\varphi \sin(\vartheta) d\vartheta$, meaning there is no energy radiated in the backscattered direction when the sine would be included.
Left: For $a_0 = 0.1$.
Right: For $a_0 = 1$. The subsequent black dotted lines are obtained by multiplying Eq. 2.63 by the harmonic number.

These radiation patterns have been experimentally demonstrated in [116, 117, 118].

2.6.3 Particle distribution & Bandwidth

The bandwidth of Linear Thomson scattering is given by [119]

$$\frac{\sigma_\omega}{\omega} \approxeq \sqrt{\left(\Theta + \frac{\sigma_{\epsilon^N}}{\sigma_{W_e}}\right)^2 + \left(2\frac{\sigma_\gamma}{\gamma}\right)^2 + \left(\frac{\sigma_{\omega_l}}{\omega_l}\right)^2} \tag{2.64}$$

where Θ is related to aperture through which the radiation is collected and is given by $\Theta = \frac{1}{\sqrt{12}} \frac{(\gamma\vartheta_{max})^2}{1+(\gamma\vartheta_{max})^2/2}$.
Figure 2.10 shows the radiation collected for various acceptance angles for a single electron. For $\vartheta \leq \frac{1}{6\gamma}$ the shape is of the spectral distribution is shaped like the (relativistic Doppler-shifted) Fourier transform of the laser pulse. For smaller angles the bandwidth does not reduce significantly, but the energy collected does.

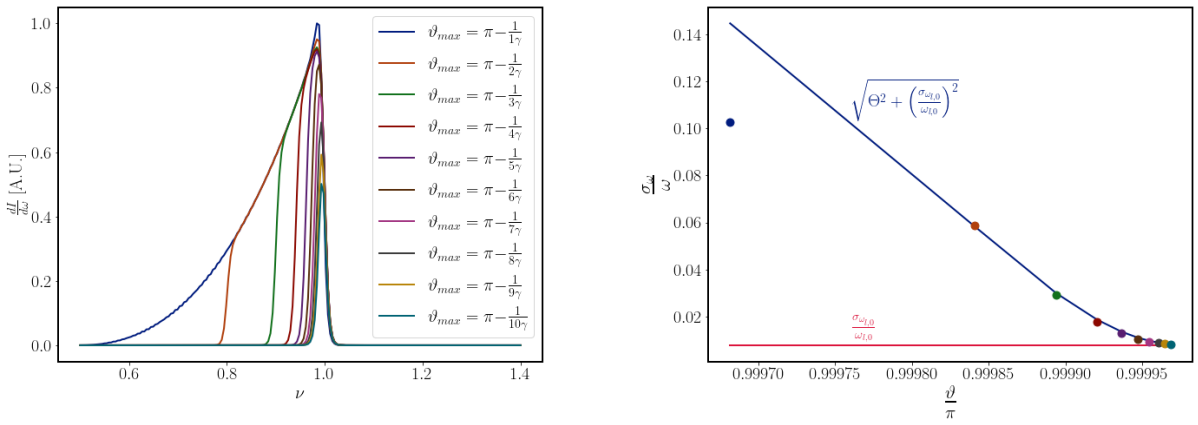

Figure 2.10: Radiation from Linear Thomson scattering of a single electron collected within different solid angles. The laser has a length of $N_c = 30$ and a longitudinal profile given by and $\gamma = 10^3$.
Left: Energy spectra.
Right: Bandwidth of the spectra of the left panel with the analytical approximation of Eq. 2.64 and the Fourier limited bandwidth of the laser pulse. The colours the bandwidths correspond to the ones in the left panel.

For an electron bunch that has non-zero emittance the bandwidth of the emitted radiation

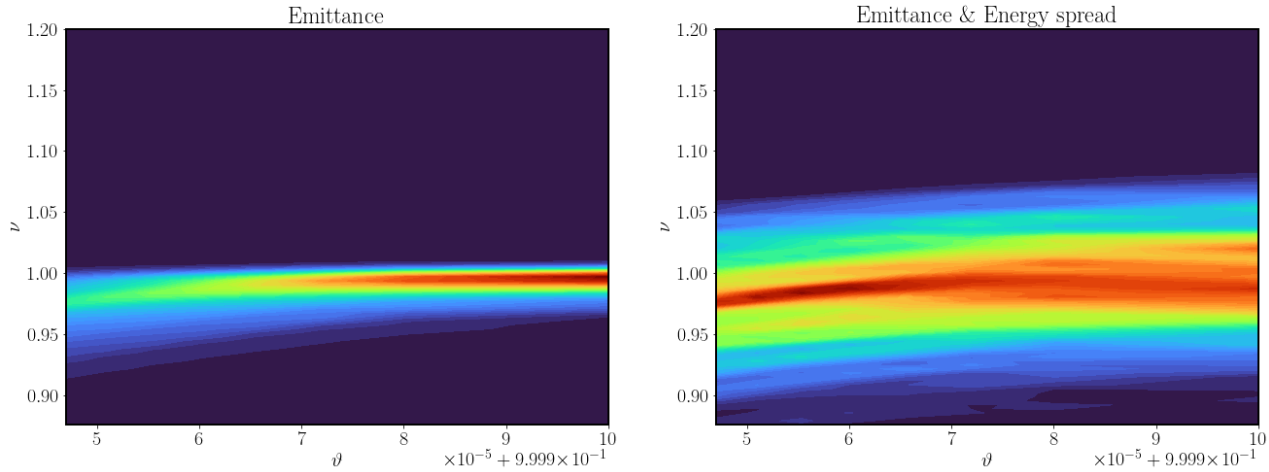

Figure 2.11: $\frac{d^2I}{d\Omega d\omega}$ within an acceptance angle of $\frac{1}{6\gamma}$ for an electron bunch with
Left: Emittance $\epsilon^N{}_x = 10^{-6}$.
Right: Emittance $\epsilon^N{}_x = 10^{-6}$ and energy spread $\frac{\sigma_\gamma}{\gamma} = 0.016$.

To reduce the bandwidth of Thomson (or Compton) scattering after the event would require special optics suitable for the produced wavelengths. This is not ideal, since optics induce losses if these already exist for the radiation [120].

2.6.4 Non-linear Broadening Compensation

The non-linear broadening makes a scattering source less appealing. How could one remove this non-linearity? Well the answer was hinted in Eq. 2.62: use a chirped laser pulse [121, 122, 123, 115, 124]. To have the emitted frequency constant one requires a chirp such that the (longitudinal) ponderomotive

force is compensated. The frequency modulation required is

$$\eta(\zeta) = \int_{-\infty}^{\zeta} d\zeta' \, 1 + \langle a(\zeta') \rangle^2 \tag{2.65}$$

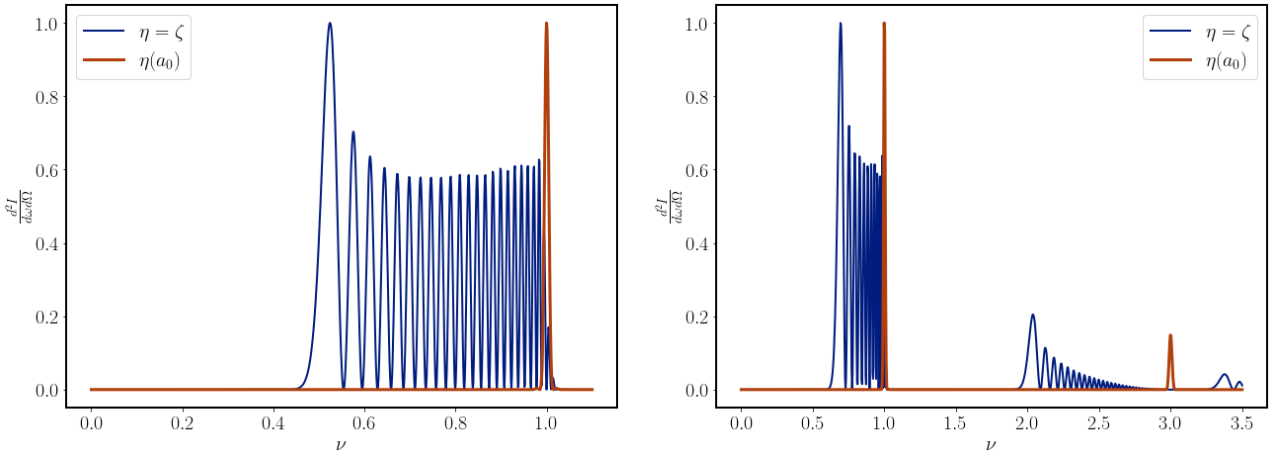

Figure 2.12: Spectra of Non-linear Thomson scattering for $a_0 = 1$. The linear Thomson spectrum can be recovered by introducing a chirp that compensates the non-linear broadening.
Left: Circularly polarised laser pulse. Here $\langle a \rangle^2 = a_0^2 \mathscr{E}^2(\zeta)$
Right: Linearly polarised laser pulse. Here $\langle a \rangle^2 = a_0^2 \mathscr{E}^2(\zeta)/2$

Such a frequency modulation exceeds known bandwidths of lasers: for $a_0 = 1$ the bandwidth of the laser needs to range from $200[nm] \leq \lambda \leq 1$ [μm].

Chapter 3

Electron transport with Lienard Wiechert Potentials

In this chapter the dynamics of the fields of the charges within a bunch (with relativistic energies) are investigated. These fields have gained traction in the past decades because the energies of the particles have increased and the curvature of their motion decreased, whereby the synchrotron radiation can become substantial to have negative effects on the properties of the bunch.

Analytical analysis of the retarded fields has a long history [19, 92]. For uniform linear motion the expressions for the retarded time and fields were given by Feynman [125]. For curved paths no exact solutions exist, and approximations are few. There exists a 1D model for coherent synchrotron radiation [22, 23]. The applicability of these 1D models are given by the two criteria

$$\frac{R}{\gamma^3} \ll \sigma_z \tag{3.1}$$

$$\frac{\sigma_r}{\sigma_z} \ll \left(\frac{R}{\sigma_z}\right)^{\frac{1}{3}} \tag{3.2}$$

In [73] it is noted that due to the reduction of the retarded time, due to a circular path, can lead to the Coulomb force being non-negligible. Recently several 2D methods have been published that supported this notion [126, 127, 128]. Not long ago even a 3D model has been published and comparing the method to obtain the retarded time one will see great similarities between here and [127, 129], but the methodology what to do with them is different.

Numerical solutions [73] can be regarded in three groups: general purpose particle trackers, dedicated retarded field codes and Particle-In-Cell codes. General purpose codes, such as Astra [130], Elegant [48] and GPT [50], have either a formula based algorithm (Like Saldin's [23]) or use a Lorentz Transform to the instantaneous rest frame of the bunch/source particle at the current time to obtain the self fields. A Lorentz transform is of course fully allowed when there is *no acceleration* involved. The problem manifests itself when the source is under acceleration, which will be further explained in Section 3.1.1.

Dedicated codes like TrafiC [131], Tredi [132], a Vlasov–Maxwell based algorithm [73] or Retar [133]. These work by finding the retarded position of the source in the history of its trajectory. This is computationally heavy as they scale with $\mathcal{O}(N_e^2)$.

Particle-In-Cell codes discretize space (cells) and compute the electromagnetic fields inside a cell using Maxwell's equations. A well known problem is numerical dispersion, because high frequencies cannot propagate with the speed of light in the discretized space [134, 94]. The major challenge for these codes are therefore the different scales involved between the particle motion, the driving field and the wavelengths of emitted radiation. To compute the propagation of the fields correctly requires a very fine mesh, but this of course increases the computation time.

In this regard it is beneficial to have rigorous 3D analytical solutions for the retarded time, by which the fields can be calculated consequently. First the retarded time is explained in depth and the challenges to compute the fields are explained. Then analytical solutions are given for the retarded time for uniform

linear motion followed by analytical approximations for circular motion. Finally the obtained results are used to give estimates on self field effects for practical situations.

3.1 Retarded time - Notation clarification

As mentioned in Chapter 2, section 2.4, the common way in literature to represent the retarded time is (e.g. [34])

$$ct_{ret} = ct - |\vec{r}_o(ct) - \vec{r}_s(ct_{ret})|\,. \tag{3.3}$$

Though, a more appealing way to describe it is through the distance the field has travelled, from both the perspective of SR and geometrically. This approach is more in line with the Huygens principle, where the particle emits a spherical wave at each point in time, see Fig 3.3. The four vector for this distance is given by

$$X_c{}^{\mu} = X_o{}^{\mu} - X_{s'}{}^{\mu} = \begin{pmatrix} ct - ct_{ret} \\ \vec{r}_o(ct) - \vec{r}_s(ct_{ret}) \end{pmatrix} = c\tau \begin{pmatrix} 1 \\ \hat{n} \end{pmatrix}, \tag{3.4}$$

and its (Lorentz invariant) magnitude

$$X_c{}^{\mu} X_{c\,\mu} = c\tau^2 - (\vec{r}_o(ct) - \vec{r}_s(ct - c\tau))^2 = 0. \tag{3.5}$$

We want to find an analytical solution for the light distance when we are given the information of the source at the current time and a point of observation: $c\tau\left(r'_s; \vec{r}_o, \vec{r}_s, \vec{\beta}_s, \vec{E}, \vec{B}\right)$.

3.1.1 Retarded time & Frames of Reference

Many numerics [130, 48, 50] use the instantaneous rest frame, either for each pair of particles or the frame of the bunch, as a way to calculate the interactions between particles. Even if we only consider the case where the forces through the retarded fields are of perturbative nature, this method of calculating the forces can only be applied for inertial frames. This we can see in Figure 3.1: in orange is the retarded position and in green the current position of the source and an observer in purple. For inertial frames it does not matter whether the retarded position is calculated from the retarded or current position of the source as the observer always intersects with the light cone of the retarded particle.

For a particle under acceleration, however, causality breaks under such Lorentz transformations, see bottom right panel of Figure 3.2. The observer intersects the light cone of the source if, and only if, the Lorentz transformation is performed for the retarded position of the source (Bottom left of Figure 3.2). One could argue that for small distances between the observer (purple) and the source (green) the discrepancy of causality diminishes. This, however, requires knowledge of the $c\tau$ a priori, because the relevant approximation should be that the distance between the source's current and retarded position is sufficiently small.

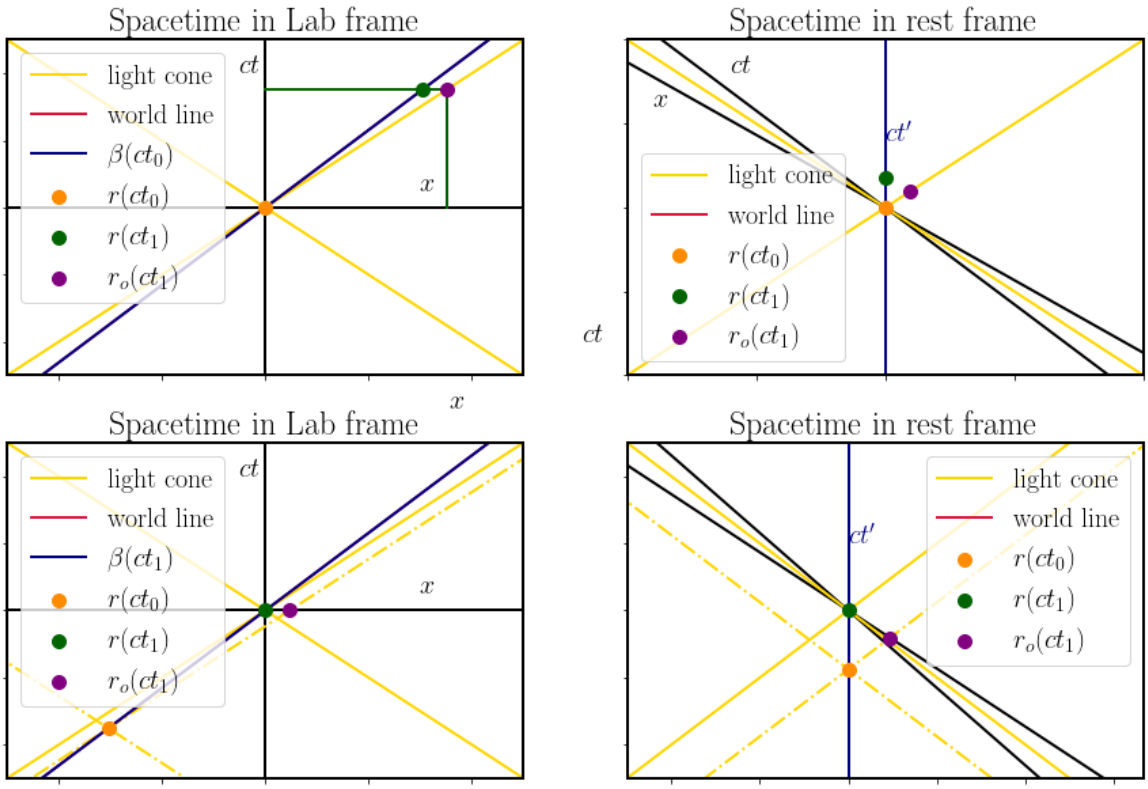

Figure 3.1: 2D Space-time diagrams for a source particle with uniform linear motion, where the current position is green and the retarded position is orange, and an observer in purple. The left and right frames are connected by a Lorentz transformation.
Top left: In the lab frame the observer lies on the light cone of the source particle at the retarded time. The source particle at the current time is spatially separated from the observer.
Top Right: In the rest frame of the source the observer (still) lies on the light cone of the source particle at the retarded time.
Bottom left: The source particle at the current time (now in the origin) has its own light cone and the light cone of the retarded position is dotted. The observer lies on the light cone of the retarded source.
Bottom right The observer lies on the past light cone of the source particle at the current time. This means that the effect of the source particle on the observer can be calculated using ct_{adv}.

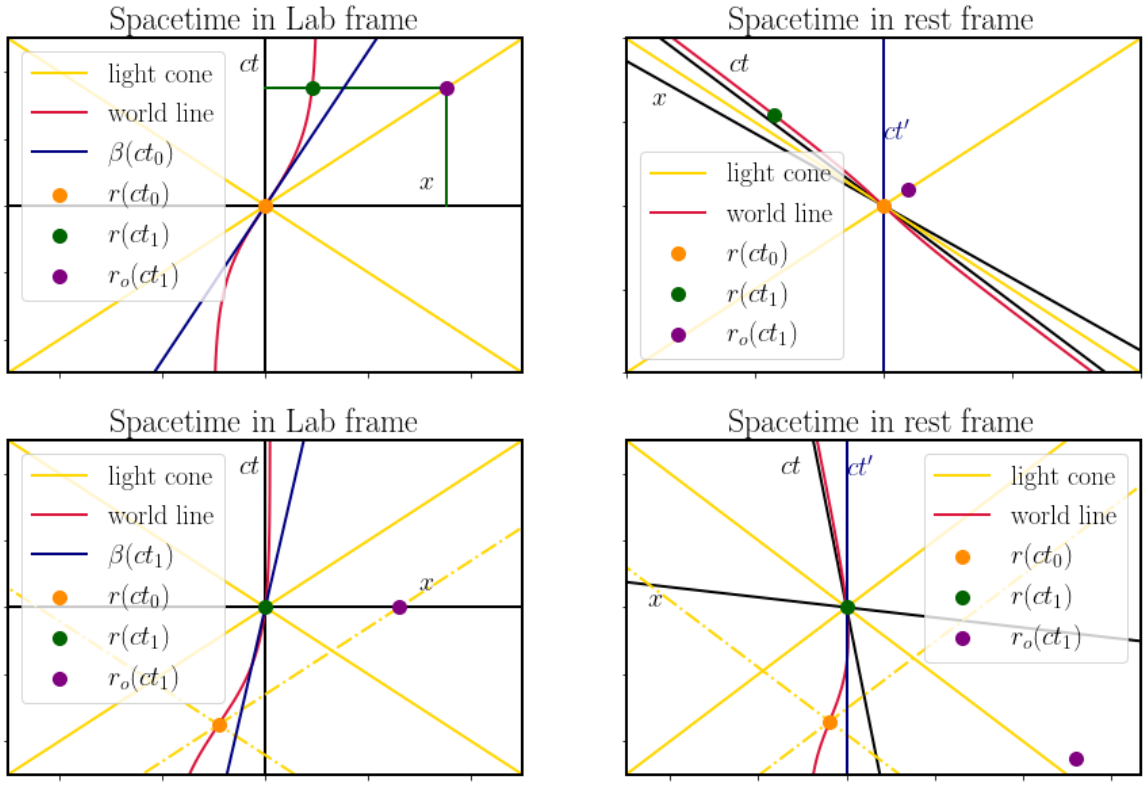

Figure 3.2: 2D Space-time diagrams for a source particle under acceleration, where the current position is green and the retarded position is orange, and an observer in purple. The left and right frames are connected by a Lorentz transformation.
Top left: In the lab frame the observer lies on the light cone of the source particle at the retarded time. The source particle at the current time is spatially separated from the observer.
Top Right: In the rest frame of the source the observer (still) lies on the light cone of the source particle at the retarded time.
Bottom left: The source particle at the current time (now in the origin) has its own light cone and the light cone of the retarded position is dotted. The observer lies on the light cone of the retarded source.
Bottom right The observer does not lie on the light cone of the retarded- nor on the future source position: causality is broken. The forces on an observer cannot be calculated in the (instantaneous) rest frame of the source at the current time.

3.1.2 Huygens style - Forward in Time Calculation

One way to calculate the retarded fields would be to approach it in the style of the Huygens principle: at each point in time the source emits a spherical wave and its radius increases along with time. The properties of the electron for each spherical wave are known and one is left to reiterate the value of the electric field. The electric field lines can be retrieved by adding labels to each point on each spherical wave and connect the same labels from the consecutive waves. This was already developed in [135] and gave the tangential field lines. Here the field is calculated according to Eq. 2.21. This approach can be used for any type of motion. A few examples can be seen in Figure 3.3.

In the Figures the simulation time is the same for all four cases, and therefore the radius of the first wave is the same. To know the field beyond this first wave requires times before the simulation started. In fact this is an initial condition problem. The Doppler effect is clearly visible: the density of the waves are highest in the direction of the motion of the source.

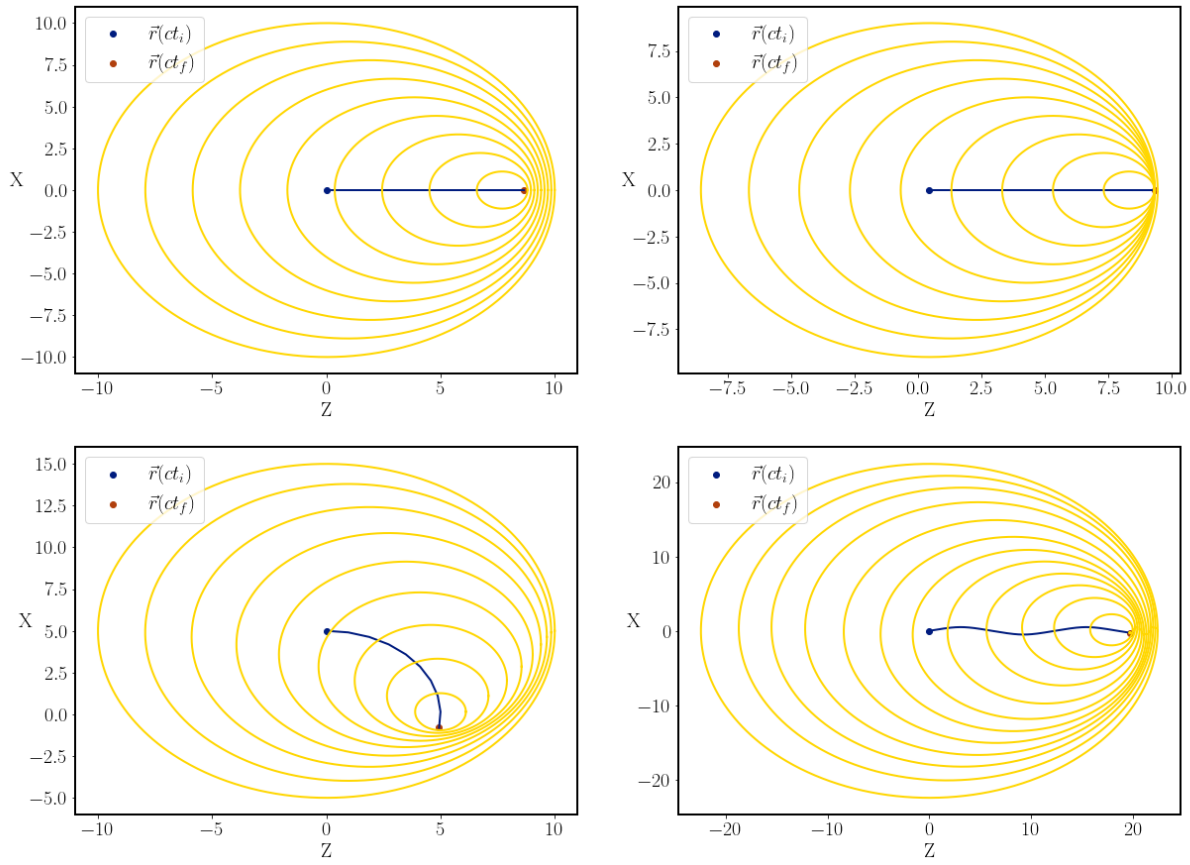

Figure 3.3: Representations of the forward in time calculation for various motions of a charged particle. At each point in time the particle emits a spherical wave, with the origin at the particle's position. The radius of the wave is the time difference between emission and the current time. All the properties to calculate the Lienard-Wiechert potentials are known, since the wave is calculated from a retarded position. A couple of notable facts: 1) None of the waves intersect, as this would break the speed of light. 2) The wave with largest radius comes from the start of the simulation. Points outside this sphere are affected from the source at earlier times. 3) The density of waves are highest in the direction of motion: Doppler shift.
Top left: Linear motion. Within transport lines it represents the drift spaces between
Top right: Linear acceleration.
Bottom left: Circular motion, like that of an electron in a dipole magnet.
Bottom right: Oscillating motion including a longitudinal momentum as is the case of an undulator and Thomson scattering.

For didactic purposes or low electron energies this method is quite fast as it does not require many waves. However, it is rather slow when the field is calculated for the use of a particle tracker; it requires small time steps to reduce the gaps between the waves, smaller than $\sim \frac{1}{\gamma}$, in the vicinity of the source particle. Moreover the the field is calculated for the entire trajectory, which means that a lot of calculation power goes to points far away of the source particle. Finally, it is hard so sum the fields from different particles together.

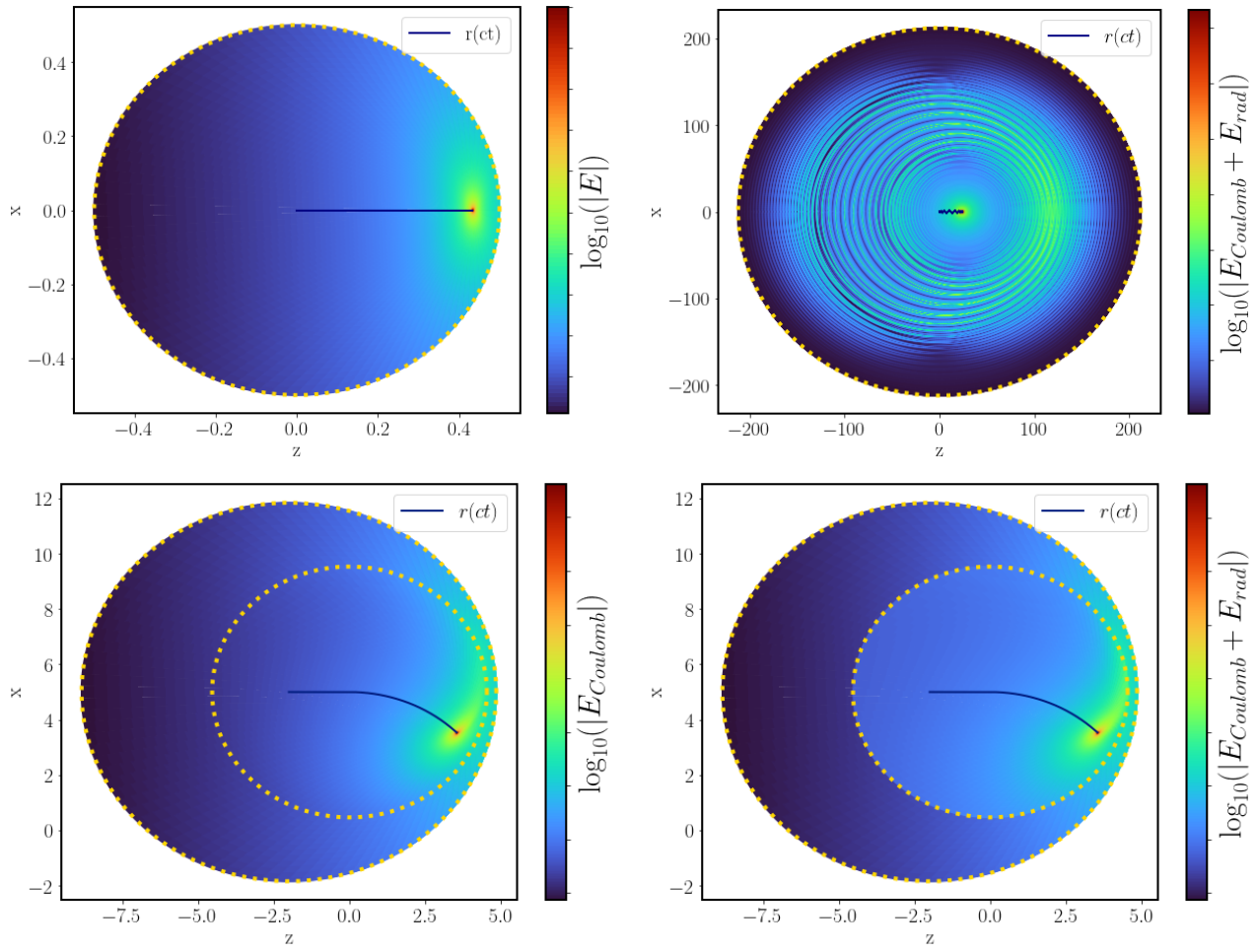

Figure 3.4: Retarded electric fields calculated in the Huygens style for different trajectories (dark blue). The outer yellow circle indicates how far the field has travelled from the starting position of the particle.
Top left: Linear motion. Within transport lines it represents the drift spaces in beamlines.
Topright: Thomson scattering with an electron initially at rest ($\gamma = 1$) with a linearly polarized laser pulse with $a_0 = 2$ and $N_c = 5$.
Bottom left: The Coulomb field for linear motion followed by a circular motion. Representing a drift and a dipole with a hard edge. Here $\gamma = 2$ and the radius of the circular motion is $R = 5$ [cm]. The inner yellow dotted circle indicates the how far the field travelled from when the electron starts its circular motion.
Bottom right: Same motioin as left, but the total retarded electric field is given. The acceleration is instantaneous due to the hard edge approach of the dipole and hence gives a jump in the electric field.

3.2 Far Field vs Near Field

When discussing the pattern of synchrotron radiation most will think about the $\frac{1}{\gamma}$ cone as depicted in Figure 1.1. This is the *far field* which is true for a short time of acceleration, in which the source is visible to the observer, and that the observer is sufficiently far enough away. This means that $\vec{\beta}$, $\hat{n}$ and $c\tau$ change negligibly over the time the electron is visible to the observer. This image distorts what is happening in the *near field*.

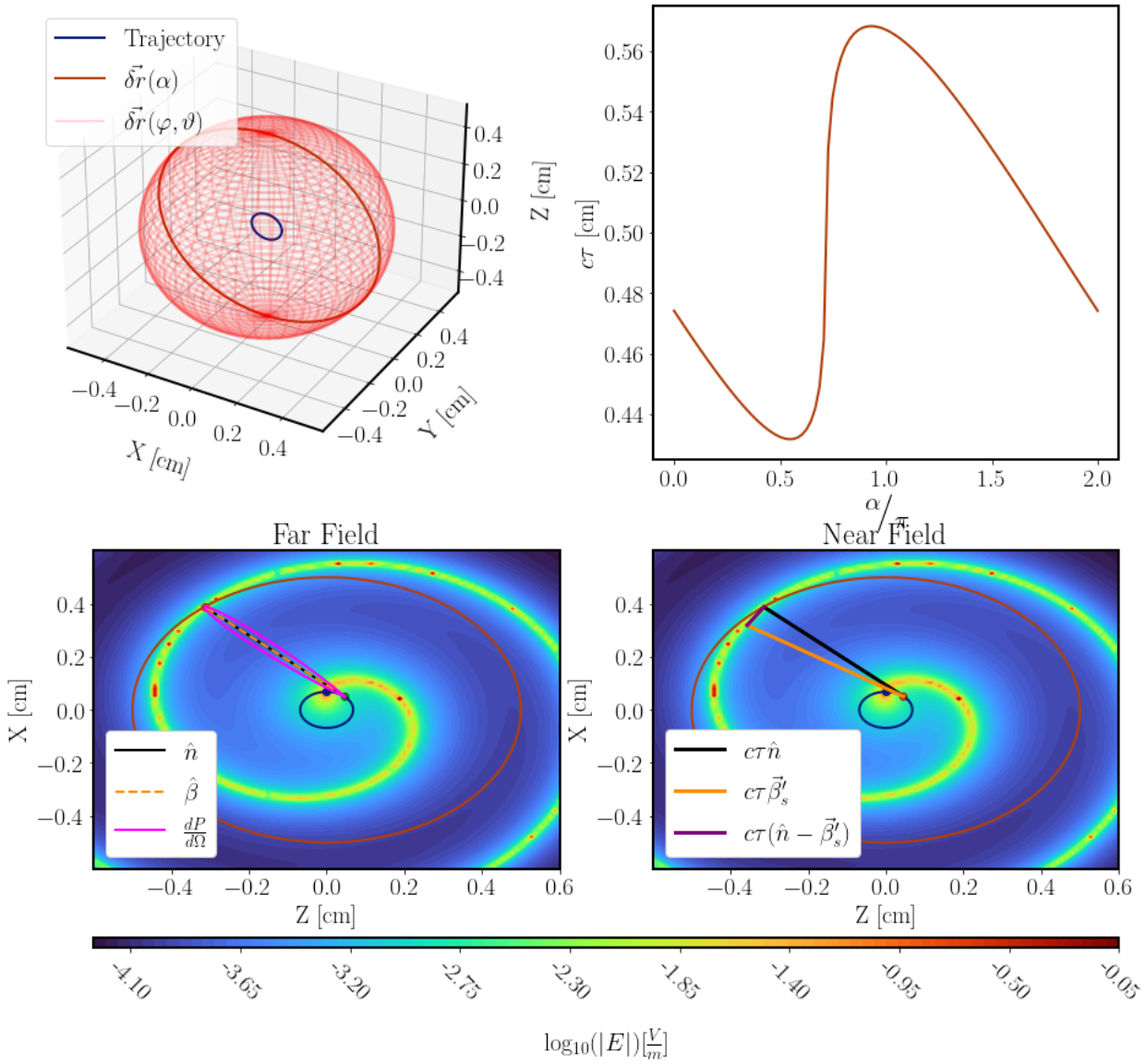

Figure 3.5: Retarded time and electric field calculated numerically in a far field configuration: the source travels on a circular trajectory and the observation points $\vec{\delta r}(\alpha)$ and $\vec{\delta r}(\varphi,\vartheta)$ encompass the the motion with ta distance 0.5[cm]. The retarded time is found by using a Newton method and providing the estimated value as the distance between the source and the observation point. The same parameters are used as in [133] for comparison: $R = 628\mu$m, $\gamma = 4.123$ and $\vec{B} = -10^5$ Gauss. The bottom panels show the magnitude of electric field on a grid in the $x-z$ plane calculated through Eq. 2.21. The grid size is 1000x1000 points, but is still insufficient to calculate the electric field properly. A part can be attributed to the narrowness of the field emitted in combination with the Cartesian coordinate system and the spherical wave emitted. To be compared to *Shintake 2002* Fig. 4 [135] and *Jackson 3rd edition* Fig 14.7 [34].
Top left: Overview of the trajectory (blue), the observation points $\vec{\delta r}(\alpha)$ and $\vec{\delta r}(\varphi,\vartheta)$.
Top right: The retarded time for the observation points $\vec{\delta r}(\alpha)$. $c\tau$ can be approximated by $|\delta r|$, since the observation points encompass the trajectory and therefore the distance light needs to travel is roughly the observation distance.
Bottom left: The magnitude of the electric field in the $x-z$ plane including the $\frac{dP}{d\Omega}$ as one would calculate in the far field: $\hat{n}$ is parallel to $\vec{\beta}$.
Bottom right: The magnitude of the electric field in the $x-z$ plane with the exact retarded position of the electron. $\hat{n}$ and $\vec{\beta}$ are no longer parallel, as this would render $\hat{n}\times\left((\hat{n}-\vec{\beta})\times\frac{d\beta}{dct}\right)$ zero.

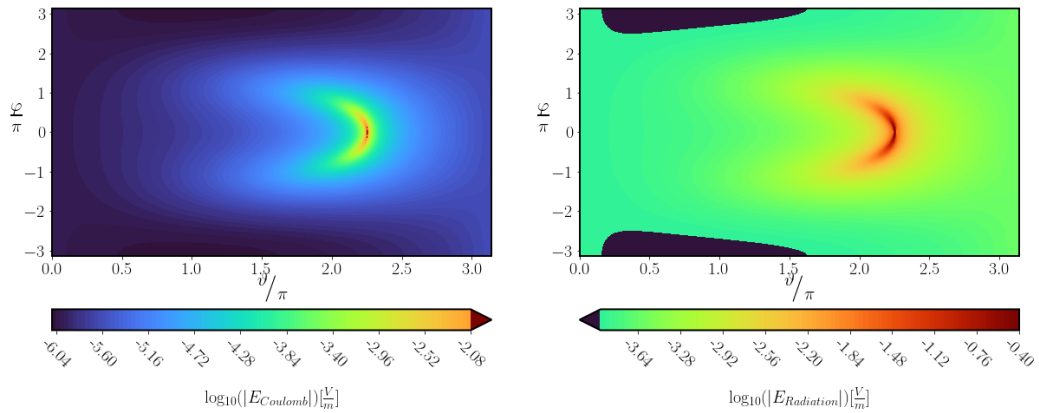

Figure 3.6: The Coulomb and radiation electric fields separately on the sphere $\delta r(\vartheta,\varphi)$ from Figure 3.5. The colour coding is such that the maximum and minimum of the electric field are equal for both graphs. The field is The Coulomb field is much smaller than the Radiation field as in accordance with the far field approximation.
Left: Coulomb field.
Right: Radiation field.

3.3 Uniform Linear motion - $c\tau\left(r_s';\vec{r}_o,\vec{r}_s,\vec{\beta}_s\right)$

For this case $c\tau$ can be found readily by performing a Lorentz transformation to the instantaneous rest frame of the source particle, where $c\tau' = |\vec{r}_s - \vec{r}_o{}'|$, and have the final answer by taking the inverse Lorentz transform. Nevertheless, solving a simple case can give clarity on methods for more complicated cases. Figure 3.7 depicts the space-time diagram of the "lab frame". For a particle undergoing uniform linear motion its retarded position can be expressed as

$$\vec{r}_s' = \vec{r}_s - \int_{c\tau} dct\vec{\beta}_s = \vec{r}_s - \vec{\beta}_s c\tau. \tag{3.6}$$

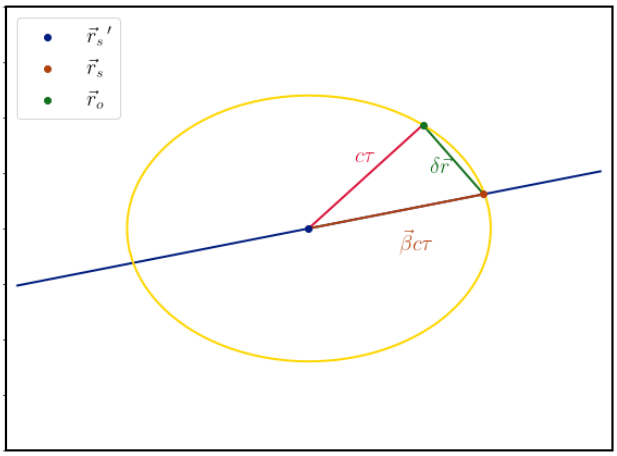

Figure 3.7: Retarded time for uniform linear motion. From the retarded position ($\vec{r}_s$) a spherical wave is emitted that reaches an observer ($\vec{r}_o$). The radius of the sphere is the light distance $c\tau$ and is solvable using the geometry.

Substitution in Eq. 3.5 leads to a quadratic equation with solutions

$$c\tau = \gamma_s^2\left[-\delta\vec{r}\cdot\vec{\beta}_s \pm \sqrt{\left(\delta\vec{r}\cdot\vec{\beta}_s\right)^2 + \left(\frac{\delta r}{\gamma_s}\right)^2}\right] \tag{3.7}$$

The two solutions are the retarded (<0) - & advanced time (>0). Before we discard the advanced solution, we will look at the solutions for observation points on a circle centred around r_s. This is shown in the top left panel of Figure 3.8 for the distance $\delta r(\alpha) = 10^{-3}$ [m], $\gamma = 10^3$. Due to the symmetrical nature of Eq. 3.7 the retarded solution of $\delta r(0)$ equals that of the advanced solution of $\delta r(\pi)$. If one solves the roots of the polynomial of Eq. 3.5 and 3.6 through the complimentary matrix method [136] one only needs to solve half the points of $\delta r(\alpha)$. Furthermore the solutions are rotationally symmetric around the propagation direction of r_s, thus the number of points can be reduced to only one quarter. If we expand the observation points to a sphere around the source only $\frac{1}{8}$ of the points are required by solving Eq. 3.7 with the aforementioned method.

The solution of $c\tau$ differ in several orders of magnitude depending on the $\delta\vec{r}\cdot\beta$, the term that tells whether r_o is in front or behind r_s, as is shown in Figure 3.8. It must be noted that for linear motion $c\tau$ is not bound when r_o is in front of r_s, i.e. $\lim_{\gamma_s\to\infty} c\tau\left(r_s';\vec{r}_o,\vec{r}_s,\vec{\beta}_s\right)\to\infty$.

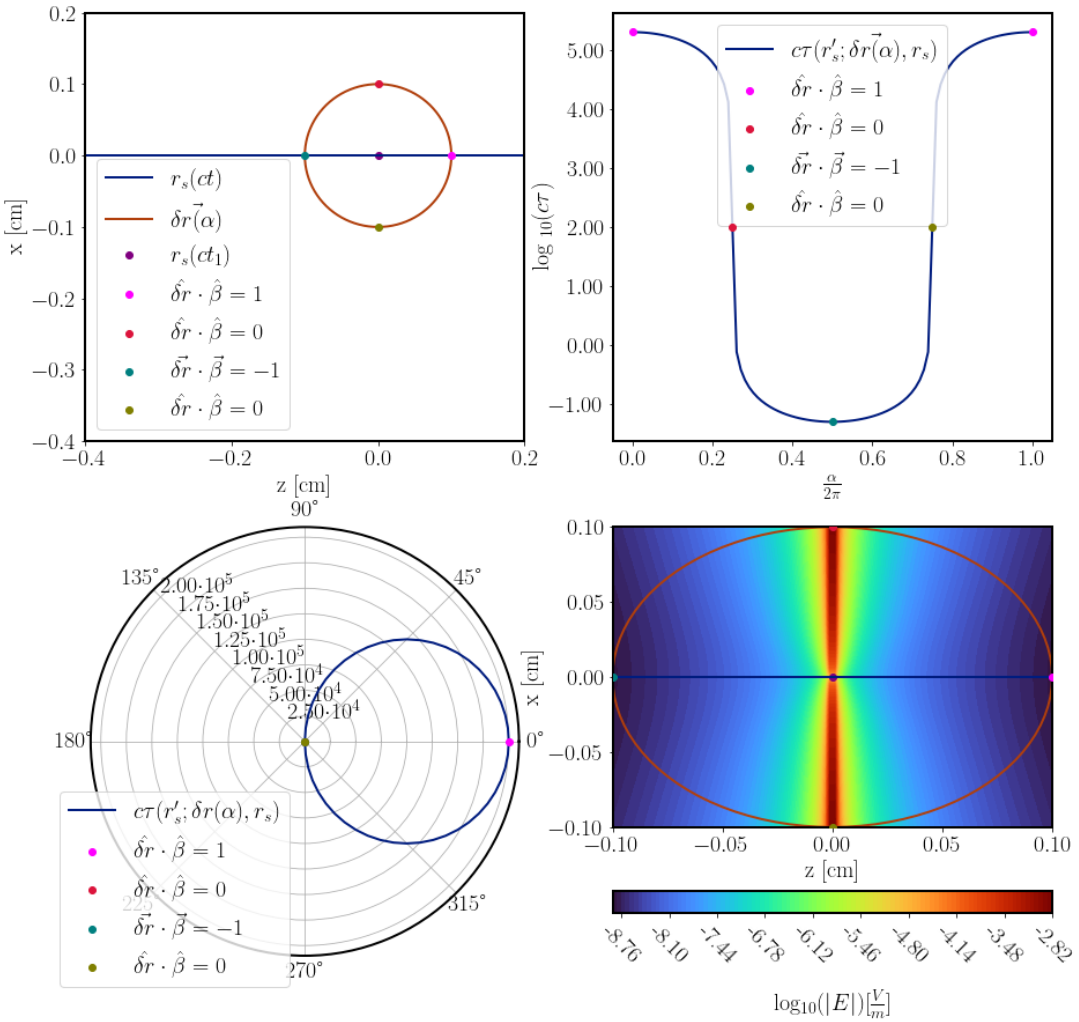

Figure 3.8: Solution fo $c\tau$ (*in [cm]!*) for uniform linear motion with the electron's energy $\gamma = 10^3$ and $\delta r = 10^{-3}$[m].
Top left: Trajectory (blue) of an electron with observation points on a circle ($\delta r(\alpha)$) around its current position. Four special points are marked.
Top right: Retarded time for the observation points. The scale of the vertical axis is logarithmic for clarity, since the difference between the forward and backward direction is six orders of magnitude. $c\tau$ is symmetric around the direction of propagation.
Bottom left: Same as top right, but represented in polar coordinates. The symmetry of $c\tau$ is even more clear.
Bottom right: The electric field (in $\frac{V}{m}$ and logarithmic scale) of points on the grid centred around the source particle at the current time.

3.4 Circular Trajectories - $c\tau\left(r'_s; \vec{r}_o, \vec{r}_s, \vec{\beta}_s, \vec{B}\right)$

In this section the retarded time for three cases is examined:

- 1D
  The source does not have a velocity component parallel to the magnetic field ($\beta_\parallel = 0$). The observer $\vec{r}_o$ lies on the trajectory of the source.

- Motion 2D
  The source does not have a velocity component parallel to the magnetic field ($\beta_\parallel = 0$). The observer can include vertical displacement.

- Circular motion 3D - Dipole Motion
  The source is allowed to have a velocity component parallel to the magnetic field. This is the real motion of a particle in a dipole or a circular undulator.

The four-velocity and four-position of a particle in a constant magnetic field are given by

$$U^\mu = \gamma \begin{pmatrix} 1 \\ \beta_\perp \cos(\frac{eB_0}{\gamma mc^2}(ct + ct_0)) \\ \beta_y(0) \\ -\beta_\perp \sin(\frac{eB_0}{\gamma mc^2}(ct + ct_0)) \end{pmatrix} \tag{3.8}$$

$$X^\mu = \begin{pmatrix} ct \\ R\sin(\frac{eB_0}{\gamma mc^2}(ct + ct_0)) \\ \beta_y(0)ct \\ R\cos(\frac{eB_0}{\gamma mc^2}(ct + ct_0)) \end{pmatrix}, \tag{3.9}$$

3.4.1 Circular Motion 1D

The trajectory of the electron changes according to its energy or the strength of the magnetic field through the magnetic rigidity. This makes it rather messy to understand the mechanics of the retarded time for the 1D model, where the observer lies on the path of the source particle. Therefore in this section the radius of the electron's trajectory is a constant, implying that if the energy changes the magnetic field changes with it, which is exactly how a beamlines work in facilities. In this configuration the retarded time condition is given by

$$\frac{c\tau}{2R} - \sin\left(\frac{\beta c\tau}{2R} + \frac{\delta\vartheta}{2}\right) = 0 \tag{3.10}$$

and is illustrated in Figure 3.9. Linearizing this condition results is the same as assuming that the source particle travels in a straight line, which does not give the correct result see Figure 3.2 and Figure 3.10. An interesting point is that $\delta\vec{r}\cdot\beta$ does no longer indicate whether r_o is in front or behind r_s for the general case. This can easily be found by equation $c\tau = 2R$; where the light front has travelled the diameter of the circular path. The angular distance where r_o is in front of r_s is then given by $\delta\vartheta \leq \pi - 2\beta$. This also indicates that, unlike the uniform linear motion, $c\tau$ has an upper bound.

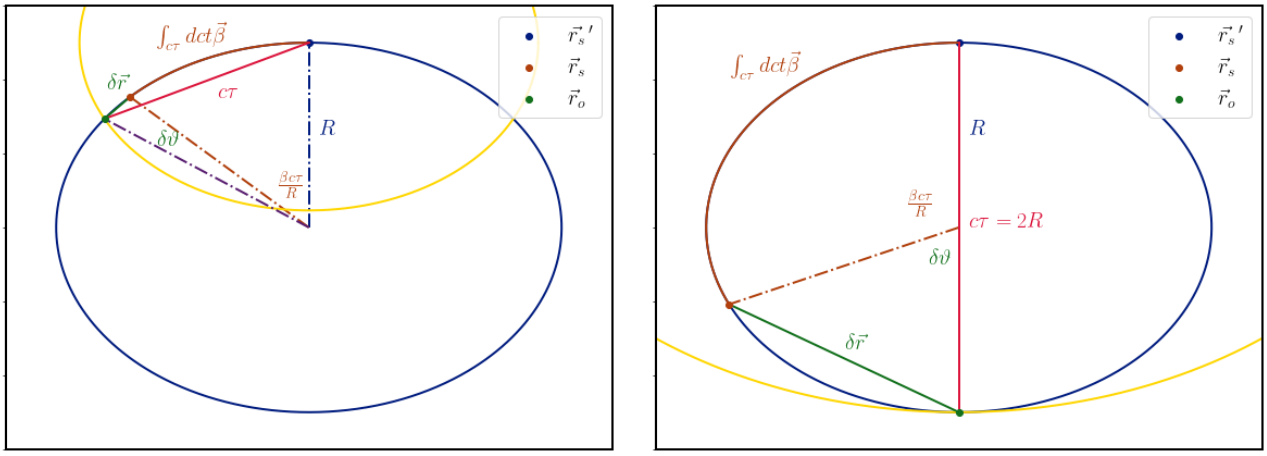

Figure 3.9: Retarded time for a source ($\vec{r}_s$) travelling along a circular trajectory (counter clockwise) where the observer $\vec{r}_o$ lies on its trajectory.
Left: The distance between $\vec{r}_s{}'$ and $\vec{r}_s$ is a chord and is given by the integral of the velocity. The path taken is the arclength and has length $\beta c\tau$. The chord and the arclength cannot be approximated to be equal to each other, as this would implicate that the particle travelled in a straight path!
Right: There exists an angle between the $\vec{r}_s$ and $\vec{r}_o$ for which the $c\tau = 2R$: $\delta\vartheta = \pi - 2\beta$. This determines whether the observer is in "front" or "behind" the source.

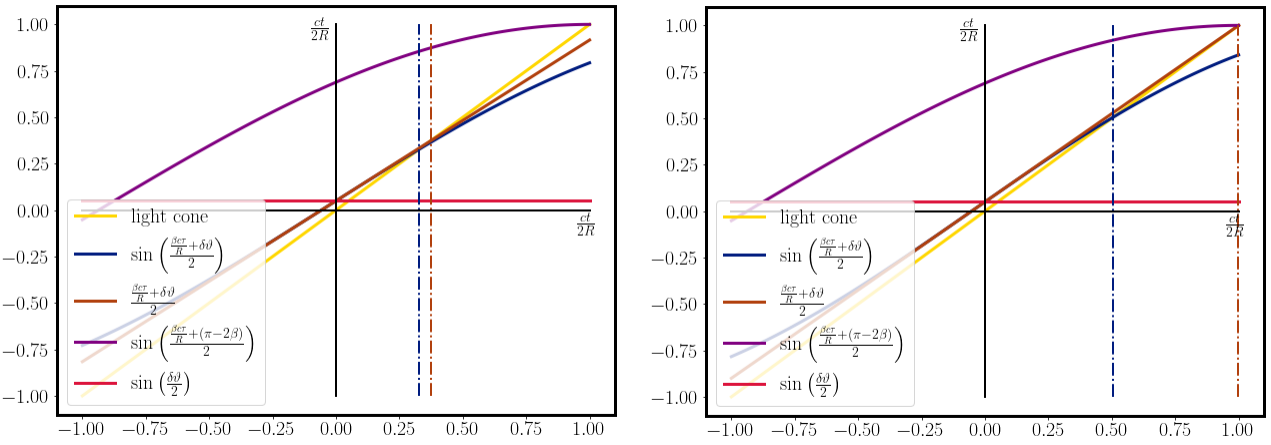

Figure 3.10: Spacetime diagrams for the retarded time condition for a source particle travelling on a circular trajectory and the observer lies ahead on the source's path (blue). The figures include the curves for which the source is stationary (red), linearized trajectory (dark orange), the (angular) distance between the particles for which $c\tau = 2R$ (purple) and the dotted lines indicate $c\tau$ for circular (blue) and linear (dark orange) trajectory. The energy of the source, the distance between the source and observer and the radius of the circle have been chosen for illustrative purposes: $R = 5$[m], $\delta\vartheta = 0.1$.
Left: The Lorentz factor of the electron is $\gamma = 2$.
Right: The Lorentz factor of the electron is $\gamma = 3.2$. For the circular trajectory there is a limit on $c\tau$ as function of γ, while for a linear trajectory it is unbounded (see section 3.3).

For the analysis of the electron-electron interaction within a bunch, the maximum scale of interest is on the order of $\delta r \sim$ [mm]. For these distances the relation $\delta r \cdot \beta$ suffices to determine which particle is in front of the other. When r_o is behind the source, Eq. 3.10 can be linearized and $c\tau \approx \frac{\delta r}{2}$ is a good approximation. When r_o is in front of r_s its a bit more complicated. Using an expansion of Eq. 3.10

comes with two questions: 1) up to what (polynomial) order do we get a good approximation and 2) how insightful is the analytical solution. Regarding the first question, we can rely on the solution of Eq. 3.7: $c\tau$ requires an even polynomial in order to correctly take the retarded and advanced solution into account. For the problem at hand this means that the minimal polynomial degree is 4. Although this can be solved analytically, the solutions can be complex and are lengthy and thus not great for understanding the dynamics. What we know for sure is that the solutions of $c\tau$ must be *real*.
Three (approximate) solutions have been found for the 1D case when r_o is in front of r_s:

1. By looking at the behaviour of the retarded time numerically, it was found that the shape resembles an S-shape (similar to the electron's longitudinal trajectory in Thomson scattering). A fit function has been developed.

$$c\tau(\gamma) = \sin\left(\frac{\delta\vartheta}{2}\right) + \frac{2A}{B}\left[\frac{\pi}{4} + \arctan\left(\tanh\left(\frac{B}{2}(\ln(\gamma_s) - C)\right)\right)\right] \tag{3.11}$$

2. Using the law of cosines for the triangle in Figure 3.9 and expanding the cosine up to fourth order. Assuming that the distance $\delta r \ll \frac{c\tau}{R}$ the fourth order polynomial can be reduced to a third order one and using Cardano's formula we find the solution to the retarded time. The derivation for this analytical approximation can be found in Appendix B.2.2.

$$c\tau = \frac{R}{\beta_s}\mathscr{C}\mathscr{F}\left(p = 3\left(\frac{1}{\gamma_s\beta_s}\right)^2,\ q = -3\frac{\delta\vec{r}\cdot\hat{\beta}_s}{R}\right) \tag{3.12}$$

3. Adding the line of $\frac{1}{\gamma}$ it was found to intersect the retarded time once. Including a factor f into this fraction shifts the point of intersection. Therefore one can imagine finding a fraction f such that the r_o lies on the cone $\frac{1}{f\gamma}$. The derivation for this analytical approximation can be found in Appendix B.2.1.

$$\begin{aligned} c\tau(f) = &\quad 2R\sqrt{1-\left(\tfrac{3\delta\vartheta}{3f^2+1}\right)^{\frac{2}{3}}}\left(\sqrt[3]{\tfrac{3\delta\vartheta}{3f^2+1}} - \tfrac{\delta\vartheta}{2}\right) \\ f = &\quad \mathscr{C}\mathscr{F}\left(p = -3\gamma_s^3\delta\vartheta, q = 3\right) \end{aligned} \tag{3.13}$$

The three solutions are shown in Figure 3.11 for $R = 5$m and $\delta S = 10\mu$m. The fitted function (Eq. 3.11) does not perform well, but in my opinion it does hint at a possible exact solution, but so far lacks the proper set-up of the problem. Eq. 3.12 has a very simple asymptotic behaviour:

$$\lim_{\gamma_s\to\infty} c\tau(\gamma) = 2R\sqrt[3]{3\frac{\vec{\delta r}\cdot\hat{\beta}}{R}} \tag{3.14}$$

The interesting part about this relation is the connection with the maximum possible value, as shown in the right panel of Figure 3.9. From this asymptote it is easy to calculate energy related to the inflection point ($\frac{dc\tau}{d\gamma} = 0$). Multiply the result of Eq. 3.14 by one half and substitute it into Eq. 3.10 and solve for β. This gives

$$\beta_C = \frac{2}{\sqrt[3]{3\frac{\vec{\delta r}\hat{\beta}}{R}}}\left[\arcsin\left(\frac{1}{2}\sqrt[3]{3\frac{\vec{\delta r}\hat{\beta}}{R}}\right) - \frac{\delta\vartheta}{2}\right] \tag{3.15}$$

$$\gamma_C = \frac{4}{5}\frac{1}{\sqrt{1-\beta_C^2}} \tag{3.16}$$

The factor $\frac{4}{5}$ has been added empirically, because the results overestimates consistently with $\sim 20\%$ for $\delta\vartheta \leq 50$ [mrad] (for example this corresponds to $\delta S = 0.25$[m] and $R = 5$[m]).

The coefficients of the fit (Eq. 3.11) could be found using the other two solutions, but because it already has a larger error than the other two this was left aside and the approximate coefficients could increases the error further.

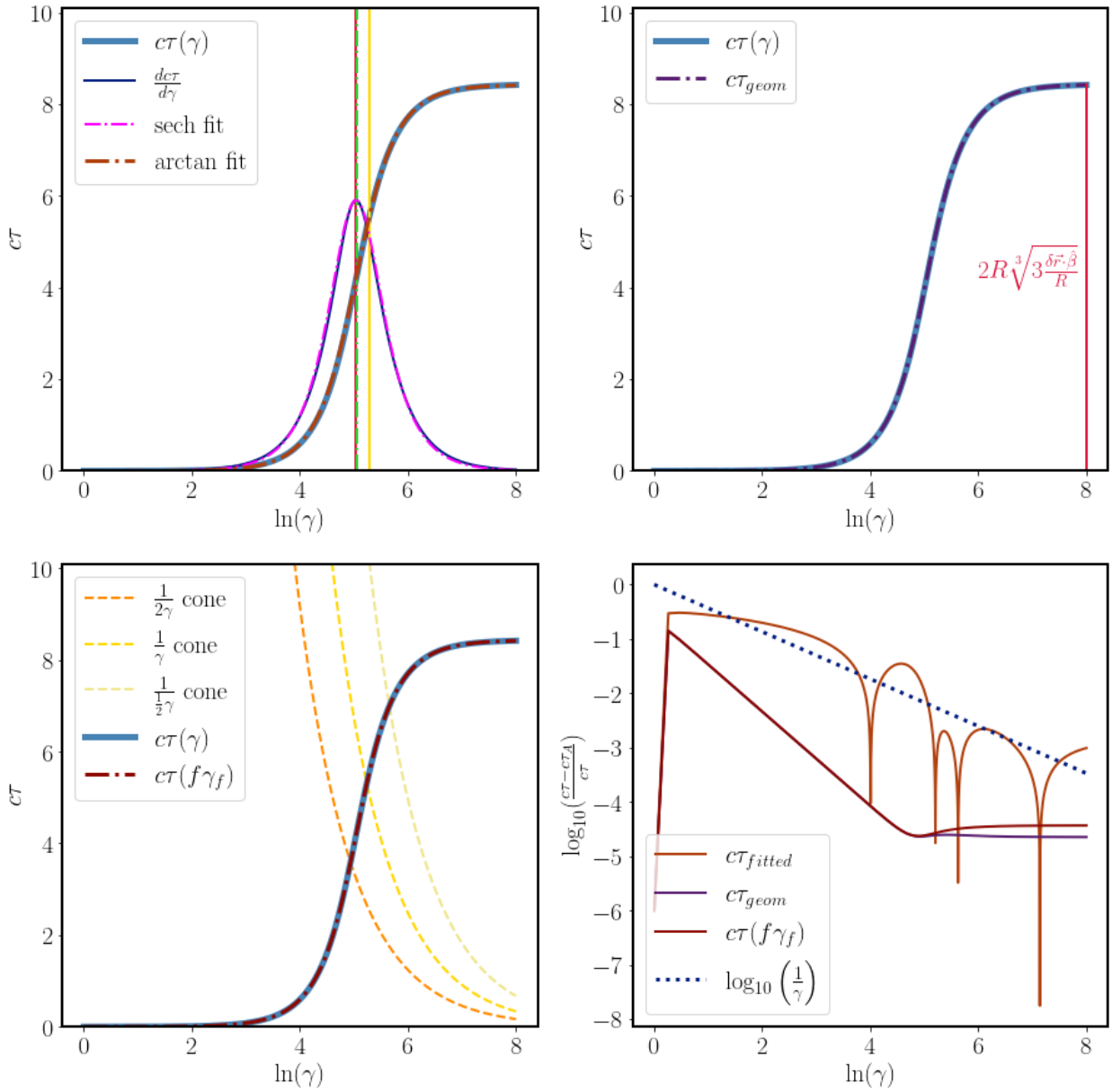

Figure 3.11: Solutions for $c\tau$ (*in [cm]!*) for $\vec{r}_o$ being an observer in front and on the orbit of $\vec{r}_s$ (the source) angularly separated $\delta\vartheta = 2\mu$rad and $R = 5$m ($\delta S = 10\mu$m). Note that the configuration has been used where the orbit (R) remains constant when the energy (γ) is increased, which implies that the magnetic field (B_0) also increases.
Top left: The curve of $c\tau(\gamma)$ suggests that its derivative has a bell shaped curve (similar to the longitudinal trajectory of an electron during Thomson scattering being an S-shape, and the velocity following the laser pulse shape, see Figure 2.7). The fit is given by Eq. 3.11.
Top right: The approximated solution from geometric principle; Eq. 3.12. From this analytical expression the value for the asymptote of $c\tau$ can be calculated.
Bottom left: The approximated solution using fractional gamma-cones; Eq. 3.14. Here we can see why the method is iterative: First the fraction f is calculated, then the new energy γ_f is calculated, which is where the $\frac{1}{f\gamma_s}$ intersects with $c\tau(\gamma)$.
Bottom right The relative error between the numerical and fitted/analytical solution of $c\tau$. It includes the $\frac{1}{\gamma}$ cone as a measure of quality, since the width of the emitted synchrotron radiation scales with it.

Using the above solutions the electric field at r_o are calculated. The total field and its components, the Coulomb and Radiation fields, are shown in Figure 3.12.

Most interestingly is that the Coulomb field starts to increase again after a certain energy, unfortunately no relation was found for this local minimum. In my opinion this is the energy for which the electron should be considered relativistic for circular motion. The local maximum of the Coulomb field coincides with the inflection point of $c\tau(\gamma)$ and is given by Eq. 3.16. The radiation field sharply decreases for a certain energy (for a fixed distance between r_o and r_s). An empirical formula has been derived using the following logic: If one calculates what the angular distance is for r_o to lie on the gamma cone (far field) of r'_s one finds the approximation $\delta\vartheta = \frac{1}{\gamma^3} \longleftrightarrow \gamma = \sqrt[3]{\frac{1}{\delta\vartheta}}$. This deviates from the exact value by a factor of 1.13..., which is not too far off from $\pi - 2\beta$ (see Figure 3.10) where β is the velocity related to the aforementioned energy and angular distance. For completeness

$$\gamma = \sqrt[3]{\frac{1}{\delta\vartheta}} \tag{3.17}$$

$$\gamma_R = (\pi - 2\beta)\gamma \tag{3.18}$$

In the next section we'll explore more in depth why the radiation field so suddenly reduces in strength, because I think the explanation is more clear using the orbit plane instead of a single observation point. The asymptotic value of the electric field is reached for energies larger than given by Eq. 3.18, and is therefore a good indicator for the radiation dominant regime.

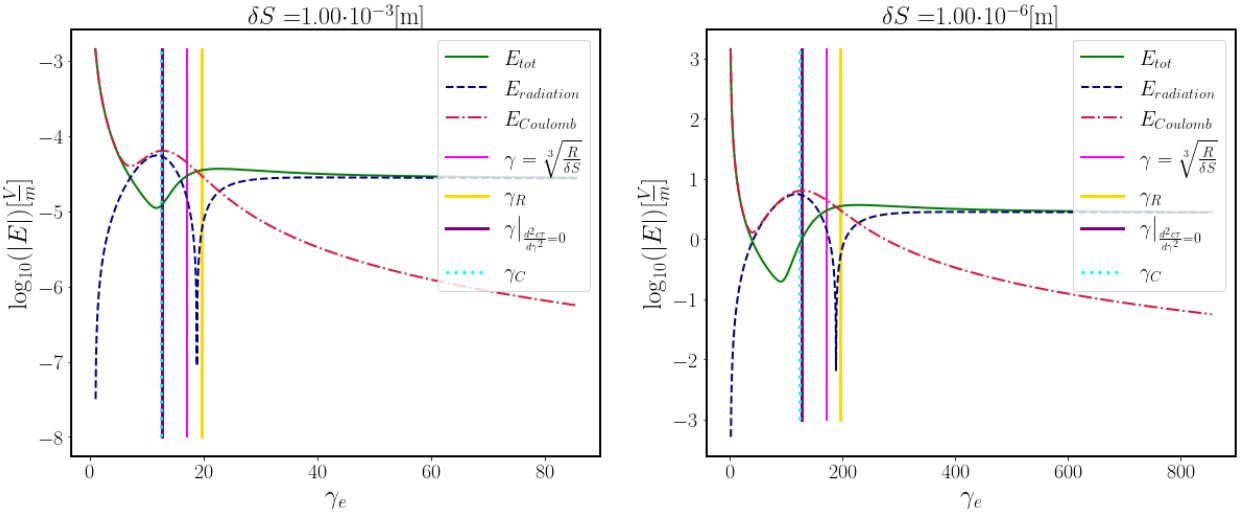

Figure 3.12: Retarded electric field and its decomposition in Coulomb and Radiation parts, for 1D circular motion as function of γ, where the radius R is kept constant and r_o is in front of r_s. Because $c\tau$ is much shorter for circular motion than linear motion the Coulomb field remains dominant for much larger γ. The maximum field strength of the Coulomb field coincides with the inflection point of $c\tau(\gamma)$ and γ_C is given by Eq. 3.16. The total electric field has an asymptotic value for γ_R (Eq. 3.18, where the Radiation term of the Lienard Wiechert potentials dominate.
Left: for an arclength distance of $\delta S = 10^{-3}$ [m].
Right: for an arclength distance of $\delta S = 10^{-6}$ [m].

3.4.2 Circular Motion 2D

In this section the motion of the source remains circular in a plane, like in the previous section, but the observer can be anywhere in 3D space. The geometrical constraint from the previous section is not adequate for this, however the angular separation depending on $c\tau$ remains attractive. Keeping the latter spans out a different triangle: from the origin to $\vec{r}_o$ to $\vec{r}'_s$ and back to the origin, see Figure 3.13.

To start, the position of $\vec{r}_o$ is projected into the plane of the source, for which the notation $\perp$ is used (i.e. perpendicular to the magnetic field). Under the assumption that the motion of the source can be described by the Lorentz force, one finds that $|\vec{r}_s'| = R$ and the constraint is given by

$$\begin{aligned} c\tau^2 - \left(\vec{r}_{o,\parallel} + \vec{r}_{o,\perp} - \vec{r}_{s,\perp}'\right)^2 &= 0 \\ c\tau^2 - r_o^2 - R^2 + 2r_{o,\perp}R\cos(\alpha) &= 0 \end{aligned} \tag{3.19}$$

where $\alpha = \frac{\beta c\tau}{R} + \delta\vartheta$ and $\delta\vartheta = \hat{\delta r}_\perp \cdot \hat{\beta}_s \arccos\left(\vec{r}_{o,\perp}\cdot\vec{r}_s\right)$. The first term in $\delta\vartheta$ is to ensure that $alpha$ is correct depending on whether $r_{0,\perp}$ is in front or behind r_s.

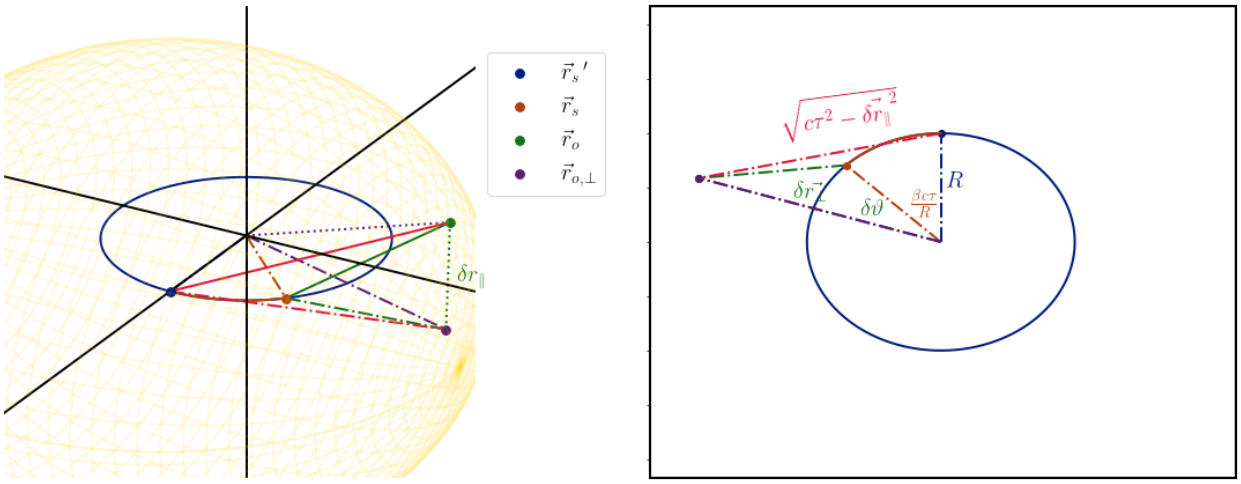

Figure 3.13: Retarded time where the source travels in a circular orbit and the observer can be situated anywhere in 3D space.
Left: 3D schematic of the geometry. The "-." lines are in the plane of the source's trajectory and the "··" perpendicular to this plane. The following lines are given: $c\tau$ (red solid line), $\vec{\delta r}$ (green solid line)
Right: Top view of the left figure. To solve for the retarded time the triangle $\vec{r}_{o,\perp}$, R, $\sqrt{c\tau^2 - \delta r_\parallel^2}$ needs to be solved using the angular separation between the source and the observer.

Before delving further into analytical approximations it is insightful to see how the retarded time behaves for observers equally spaced around $\vec{r}_s$, and compare it to the linear case. In Figure 3.14 the numerical solutions for $c\tau$ are shown for $R = 5$[m], $\gamma = 10^3$ and $\delta r = 0.5$ [m] and in Figure 3.15 for $\delta r = 10^{-3}$ [m] . For such large distances the antisymmetric behaviour of $c\tau$ is very clear. Most notably in the polar plot: the largest value of $c\tau$ is no longer in the direction of propagation but asymptotically reaches $\hat{\delta r}\cdot\hat{\beta} = \frac{\sqrt{2}}{2}$ depending on δr. Comparing $c\tau$ for the case of uniform linear motion and the circular motion (Figure 3.8 & 3.15) we see that the maximum of $c\tau$ is three orders of magnitude smaller. This is the reason why the Coulomb term is non-negligible even for relativistic energies.

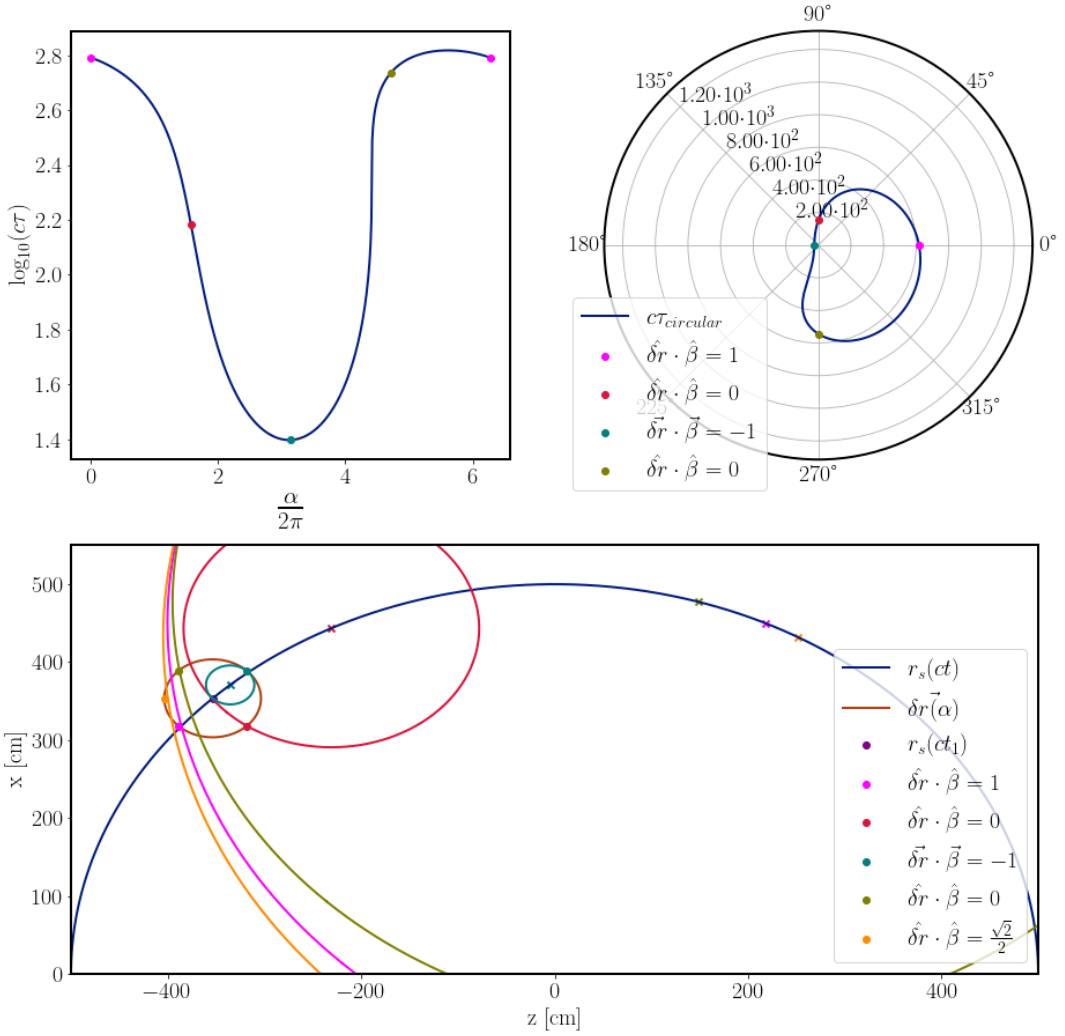

Figure 3.14: Behaviour of the retarded time for a particle travelling on a circular trajectory (counter clock wise) with energy $\gamma = 10^3$ and $\delta r = 0.5$[m].
Top left: Retarded time for the observation points equidistant around the source at the current time. The vertical axis is in logarithmic scale for clarity. The retarded time is antisymmetric. Which is most notable for the observation points perpendicular to the propagation direction ($\hat{\delta r}\cdot\hat{\beta}=0$). Note that the difference in the retarded time between the forward and backward direction (~ 1 order of magnitude) is much smaller as for the uniform linear case (~ 6 orders of magnitude) for the same electron energy and observation distance.
Top right: Same as top left, but represented in polar coordinates. The maximum value of $c\tau$ is not in the direction of motion, but off axis.
Bottom: The trajectory of the electron, with the observation points. The retarded positions for the special points are marked with "x" in the same colour. Here we can clearly see why $c\tau$ does not have its maximum in the direction of motion of the source particle.

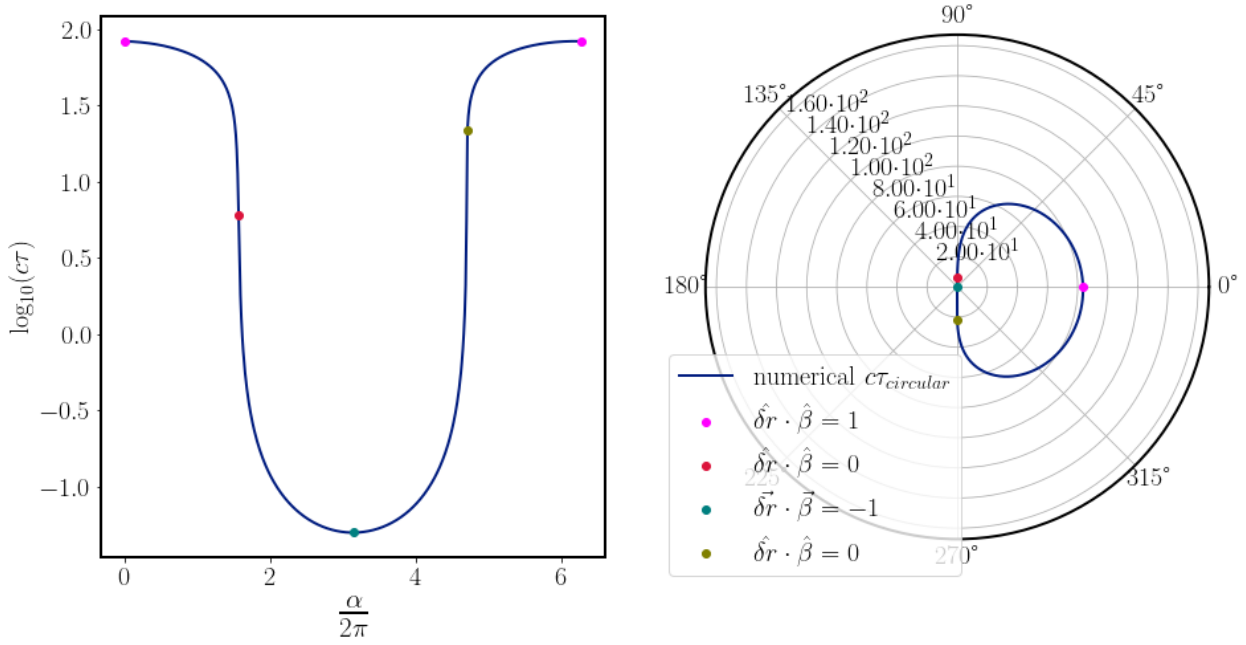

Figure 3.15: Behaviour of the retarded time for a particle travelling on a circular trajectory (counter clock wise) with energy $\gamma = 10^3$, $R = 5$[m] and $\delta r = 10^{-3}$[m].
Left: Retarded time for the observation points equidistant around the source at the current time. The vertical axis is in logarithmic scale for clarity. The retarded time is still antisymmetric, see the points of $\hat{\delta r}\cdot\hat{\beta}=0$. Note that the maximum of $c\tau$ is three orders of magnitude smaller than for the uniform linear motion (Figure 3.8).
Right: Same as left but represented in a polar plot. Here it's more clear that the maximum of $c\tau$ is in the direction of propagation.

By calculating $c\tau$ numerically we can also calculate the field on a grid near the source. Here the assumption is that the particle has travelled long enough on the circular path, meaning that the retarded fields will have travelled to each grid point. Figure 3.16 shows the magnitude of the electric field and its two constituents. The parameters are chosen for clarity and are $\gamma = 4$, $R = 5$[m] and $\delta r = 2$ [m]. The radiation field contains a curve that tends to zero and it encompasses the region where the field is at its maximum. This was noted in the previous section and the reason behind it is illustrated in Figure 3.17. There exists a retarded time $c\tau$ for which the term $\hat{n} - \vec{\beta}$ is (almost) parallel to $\dot{\vec{\beta}}$. Therefore the radiation field is zero where this occurs, and $\vec{r}_{o,\perp}$ lying on the trajectory of r_s the energy-distance condition is given by Eq. 3.18. However interesting it is, this phenomenon can only occur for the radiation field of a single particle and, moreover, because the Coulomb field is non-zero this is not a measurable quantity. The importance is that it is *not* a numerical artefact.

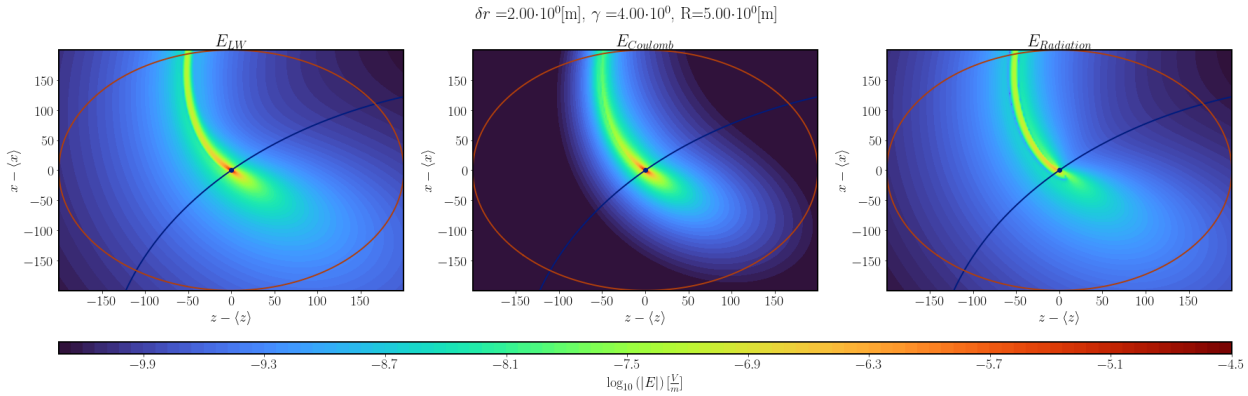

Figure 3.16: Retarded electric field near the source (r_s) which travels along a circular path with $\gamma = 4$, $R = 5$ [m] and $\delta r = 2$ [m].
Left: Magnitude of the retarded electric field.
Middle: Magnitude of the Coulomb field. Its effect depends on the distance from the source and is more tapered opposite to the direction of acceleration.
Right: Magnitude of the radiation field. There is a curve where the field tends to zero, enclosing the maximum field strength. See Figure 3.17.

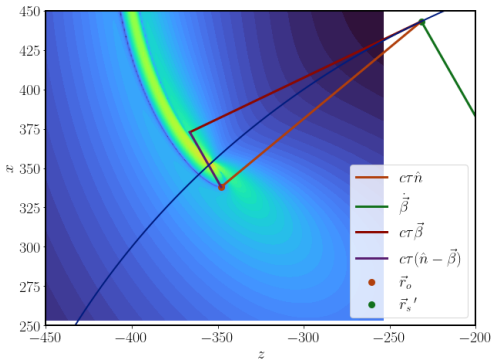

Figure 3.17: The (retarded) radiation field with the same parameters as in Figure 3.16. Lines for quantities in Eq. 2.21 are added for an observation point where the radiation field tends to zero. The reason why the field tends to zero is because $\hat{n} - \vec{\beta}$ is (almost) parallel to $\dot{\vec{\beta}}$.

In Figure 3.18 shows the dependency of the fields with respect to γ, regarding following the points from the right panel of Figure 3.12: the Coulomb and radiation field are equal (I, $\gamma = 40$), $\frac{d^2 c\tau}{d\gamma} = 0$ (II, $\gamma = 127$), (Eq. 3.18) $\gamma = (2 - \beta_c)\gamma_c$ (III, rounded off to $\gamma = 195$) and twice the previous energy (IV, $\gamma = 390$).

- case I, $\gamma = 40$: in the forward direction both fields are approximately equal, but over the 2D plane the Coulomb field remains dominant. Near $\hat{\delta r} \cdot \hat{\beta} = \frac{\sqrt{2}}{2}$ there is indication that the trajectory is circular, because the contours of the field are different for $r_o < R$ and $r_o > R$.

- case II, $\gamma = 127$: As indicated in Figure 3.12 the total electric field is lower than its constituents, most notably near $\hat{\delta r} \cdot \hat{\beta} = \frac{\sqrt{2}}{2}$. The Coulomb field is still stronger over the plane. The contours are more distorted and a minimum has formed.

- case III, $\gamma = 195$: The total electric field is still affected by the opposite signs of its constituent fields. The distortion of the Coulomb field is smaller than the grid size. For the radiation field we see a relatively large region where $\hat{n} - \vec{\beta}$ is parallel to $\dot{\vec{\beta}}$.

- case IV, $\gamma = 390$: The radiation field is dominant and the total field reflects this. The region where the radiation field tends to zero lies closer to the source and is smaller in width.

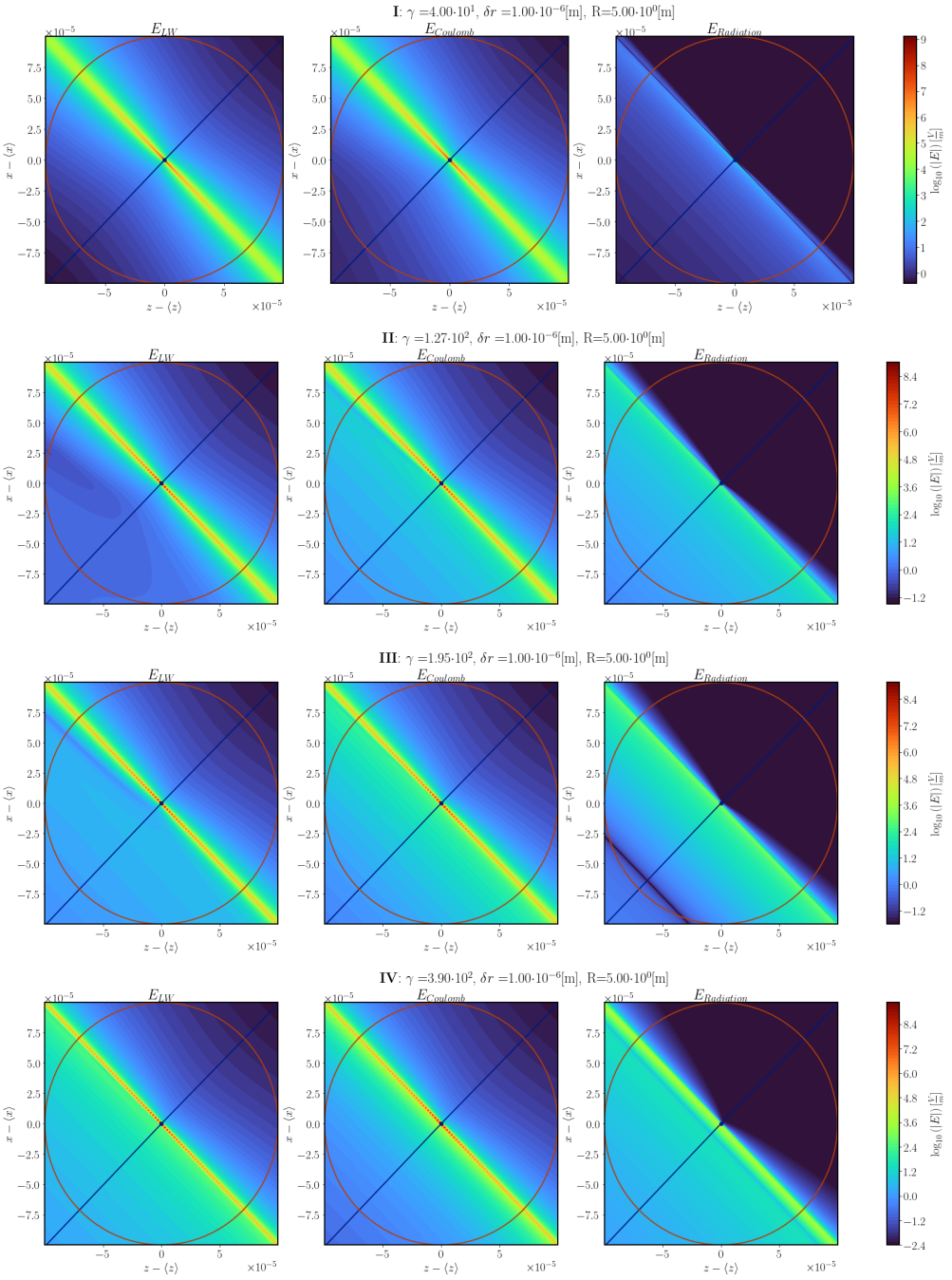

Figure 3.18: Four cases of the retarded electric fields depending on γ, with reference to the dynamics seen in Figure 3.12. The electron travels counter clockwise. For each row the left panel shows the total field, the middle the Coulomb and the right the radiation field. For each case the radius of the circular motion is $R = 5$[m] and $\delta r = 10^{-6}$[m].
I, $\gamma = 40$**:** The constituent fields are roughly equal in the forward direction (near the at the $\delta r(\alpha)$ line (orange)) . However since the Coulomb's field strength scales with $c\tau^{-2}$ it is stronger nearer to the source..
II, $\gamma = 127$**:** The total field is lower than its constituent parts, most evidently for $\hat{\delta r} \cdot \hat{\beta} = \frac{\sqrt{2}}{2}$.
III, $\gamma = 195$**:** The energy is given by Eq. 3.18. The radiation field exhibits a relatively large region where it tends to zero because $\hat{n} - \vec{\beta}$ is parallel to $\dot{\vec{\beta}}$. The distortion due to the circular motion is quite visible in the total field.
IV, $\gamma = 390$**:** The radiation field is dominant in the forward direction. The total field roughly equals the radiation field. The latter still contains a region where it tends to zero, but its size is smaller and closer to the source.

Now lets focus on the analytical solution of $c\tau$. Like in the previous section the solution of the retarded time can be found by expanding the Eq. 3.19 and solving for the roots the following fourth order polynomial

$$\frac{2Rr_{o\perp}\cos(\delta\vartheta)}{4!}T^4+\frac{2Rr_{o\perp}\sin(\delta\vartheta)}{3!}T^3+\left(\left(\frac{R}{\beta_s}\right)^2-\frac{2Rr_{o\perp}\cos(\delta\vartheta)}{2!}\right)T^2+2Rr_{o\perp}\sin(\delta\vartheta)T-\delta r^2=0, \quad (3.20)$$

where $T=\frac{\beta_s}{R}c\tau$. Many terms could be factored out in the equation above, but they were kept for completeness. Rather, lets talk about the possible roots of this polynomial. There is a set of four approximate expressions possible:

- $\hat{\delta r}\cdot\hat{\beta}=1$: the same solution as in the previous section (equations 3.11, 3.12 and 3.14).
- $\hat{\delta r}\cdot\hat{\beta}=0$: Eq. 3.20 reduces to a biquadratic
- $\hat{\delta r}\cdot\hat{\beta}=-1$: Eq. 3.19 can be linearized and $c\tau\approx\frac{\delta r}{2}$

Figure 3.19 shows the results of $c\tau$ when the observer lies in the plane of the source (i.e $\vec{r}_o=\vec{r}_{o,\perp}$). The roots of Eq. 3.20 are a pretty good approximation, although when $\delta\vartheta$ tends to zero the error grows. For these points it would be beneficial to implement the biquadratic solution, where $\vec{r}_o$ is given relative to $\vec{r}_s$ instead of the origin (the centre of circular motion).

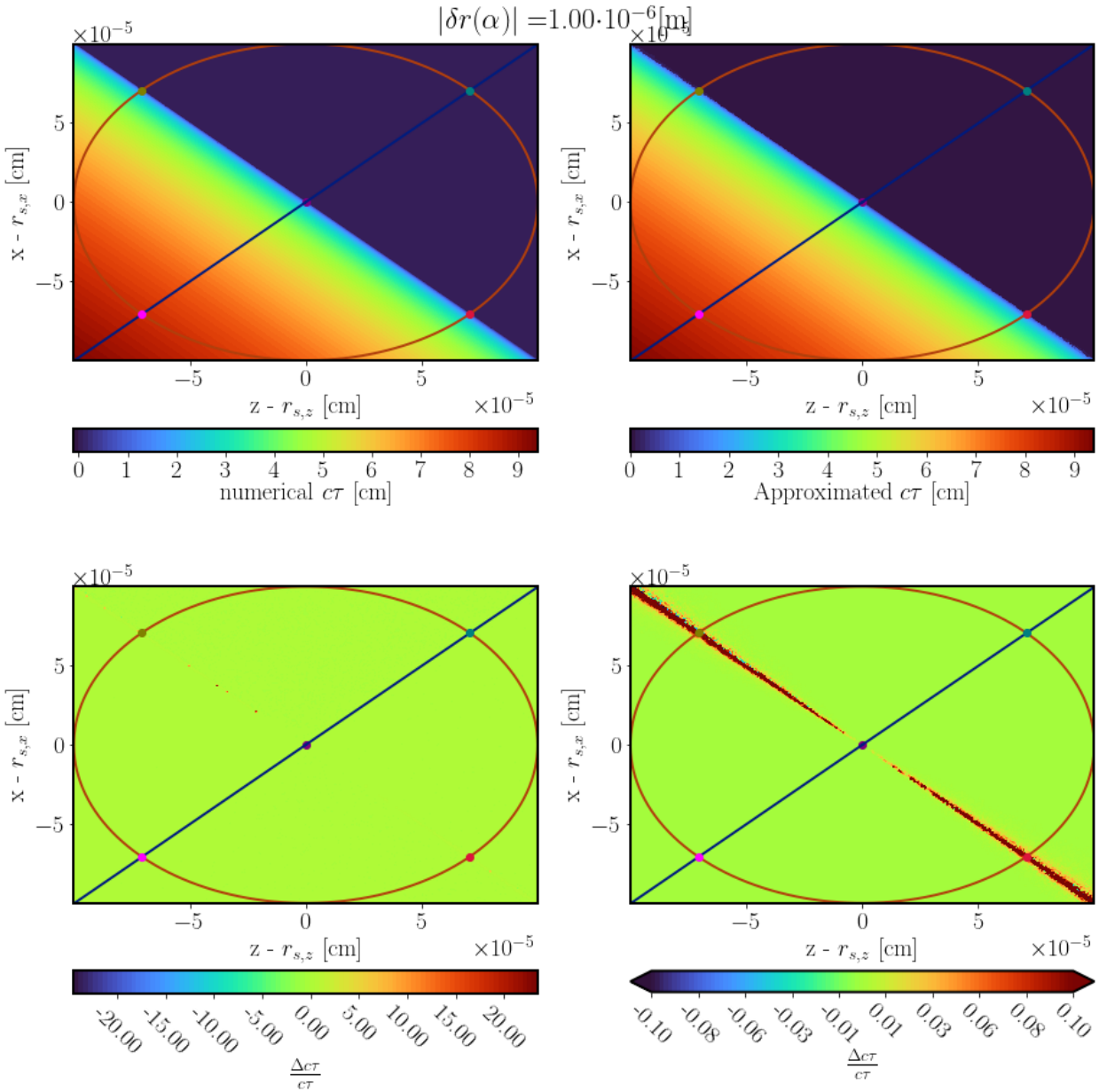

Figure 3.19: Comparison between numerically and analytically calculated retarded time according to Eq. 3.5 and 3.20 respectively.
Top left: Retarded time calculated numerically.
Top Right: Retarded time calculated by solving the fourth order polynomial.
Bottom left: Relative error for the analytical solution.
Bottom right: Same as bottom left but with the error range bound by 10%.

In principle the solution of $c\tau$ for a particle travelling along a circle should converge to the linear case for either very large $\frac{R}{\gamma}$ or very small δr. The figures below show that this is true, but that even for $\delta r = 10^{-8}$[m] the discrepancy in $c\tau$ is still some factor but at least on the same order of magnitude. Note that the distortion, as seen in case III in Figure 3.18, becomes visible once more.

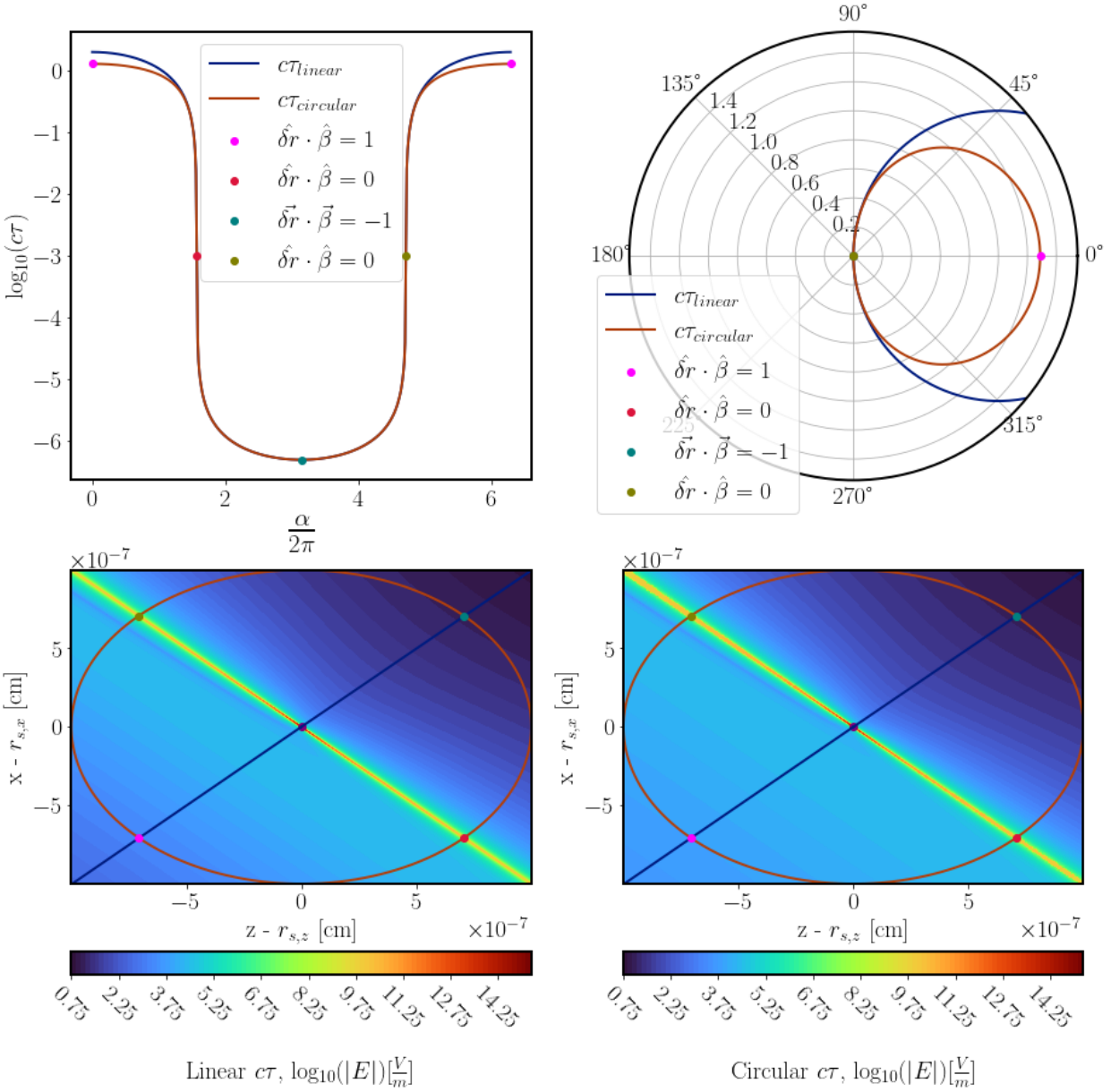

Figure 3.20: Retarded time and the electric field calculated in the xz-plane using the linear- and circular solution. The distance between the source particle and the observation points $\delta r(\alpha)$ is 10^{-8} [m]. Note that the linear solution is the same as calculating the retarded time and electric field in the instantaneous rest frame of the source particle and is clearly a bad approach.
Top left: Comparison of the retarded time as function of the observer position $\delta r(\alpha)$. Even for such small distances between $\vec{r}_s$ and $\vec{r}_o$, notably the start of the x-ray regime, the linear solution still overestimates the retarded time in the forward direction ($\hat{\delta r}\cdot\hat{\vec{\beta}}_s=1$) .
Top Right: Same as left but in polar coordinates.
Bottom left: The electric field in the xz-plane when the retarded time is calculated using the linear solution.
Bottom right: The electric field in the xz-plane when the retarded time is correctly calculated using the circular solution.

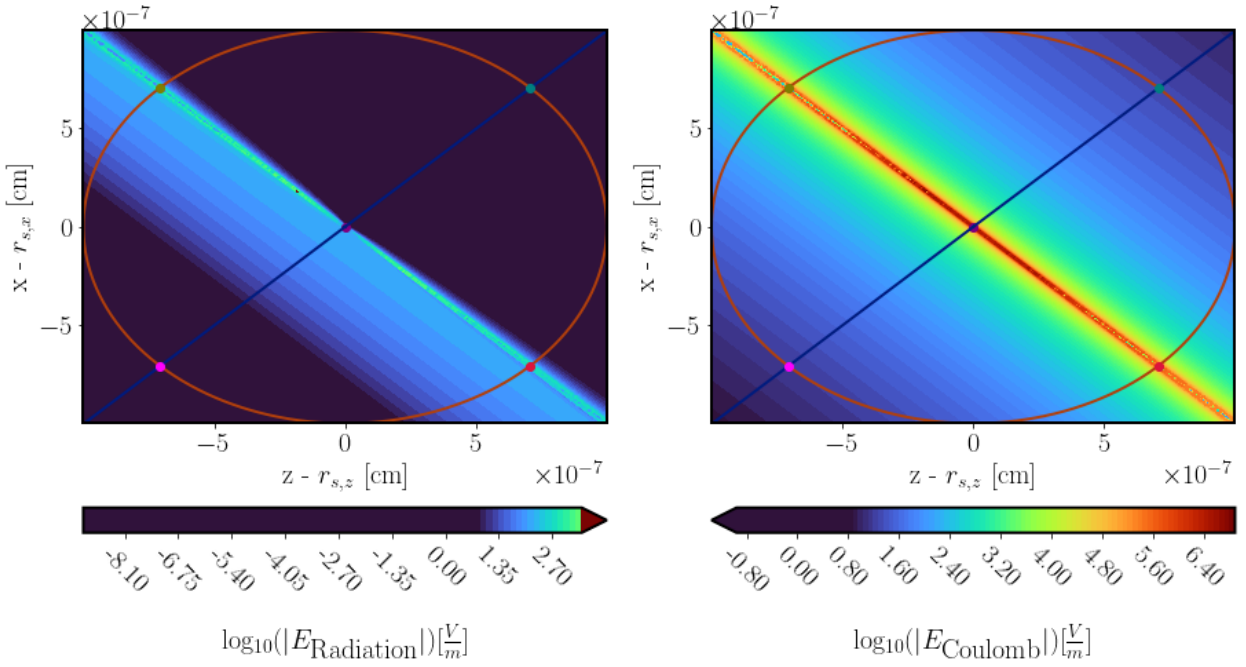

Figure 3.21: Comparison between the Coulomb and Radiation part of the electric field. The radius from the source is $\delta r = 10^{-8}$[m]. The dependency of which field is dominant depends on the scale where one looks at: the closer to the source the Coulomb force will always dominate.

3.4.3 Circular motion 3D - Dipole Motion

The solution of $c\tau$ for a particle travelling according to 3.8 can be found in two different ways:

1. Perform a Lorentz Transform (perpendicular to the circular motion!) and use the 2D solution, while keeping in mind that the simultaneity is lost in this frame, and make a Lorentz Transformation back

2. Find the geometrical relation in the lab frame

Here the we will continue on the track of having all solutions in the lab frame. The difference between the previous case is that the source particle has a velocity component parallel to the magnetic field, and is thus unaffected. Thus we can combine the solutions for uniform linear motion and the 2D circular motion. The condition for $c\tau$, as shown in Figure 3.22, is given by

$$\begin{aligned} c\tau^2 - \left(\vec{r}_{o,\parallel} + \vec{r}_{o,\perp} - \vec{r}'_{s,\perp} - \vec{r}'_{s,\parallel}\right)^2 &= 0 \\ c\tau^2(1-\beta_\parallel^2) + 2\delta r_\parallel \beta_\parallel c\tau - \left(r_{o,\perp}^2 - R^2 + 2r_{o,\perp}R\cos(\alpha)\right) &= 0 \end{aligned} \tag{3.21}$$

where $\alpha = \frac{\beta_\perp c\tau}{R} + \delta\vartheta$ and $\delta\vartheta = \hat{\delta r}_\perp \cdot \hat{\beta}_\perp \arccos\left(\vec{r}_{o,\perp} \cdot \vec{r}_{s,\perp}\right)$. The two limits are recovered; 1) $\vec{\beta}_\perp = 0$ the uniform linear motion, 2) $\vec{\beta}_\parallel = 0$ the circular 2D motion with the observer in 3D space.

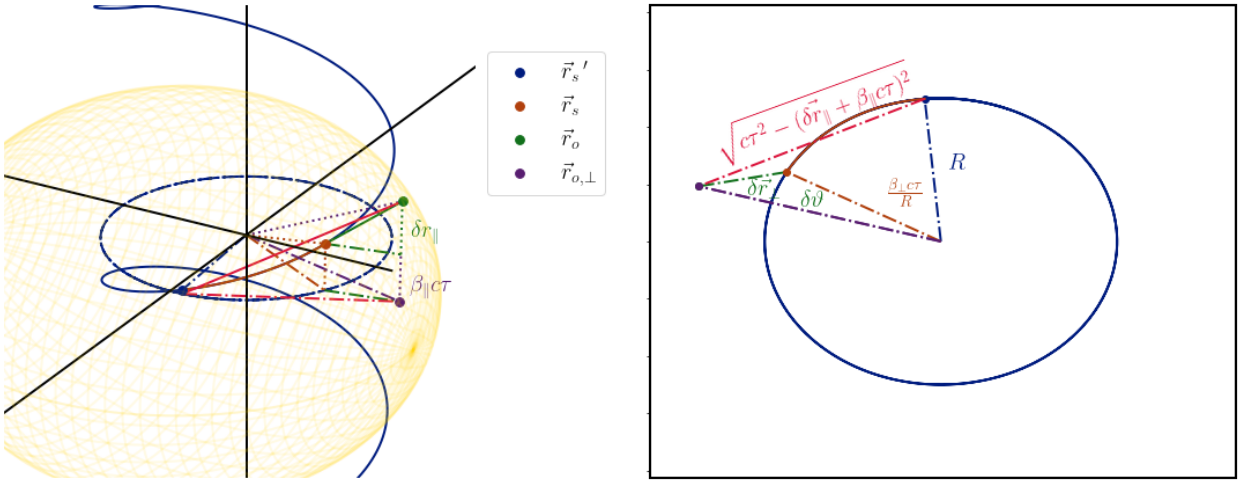

Figure 3.22: Retarded time where the source travels in a circular orbit and the observer can be situated anywhere in 3D space.
Left: 3D schematic of the geometry. The "-." lines are in the plane of the circular orbit and the "‥" perpendicular to this plane. The following lines are given: $c\tau$ (red solid line), $\vec{\delta r}$ (green solid line)
Right: Top view of the left figure. To solve for the retarded time the triangle $\vec{r}_o$, R, $\sqrt{c\tau-(\delta r_\parallel+\beta_\parallel c\tau)^2}$ needs to be solved using the angular separation between the source and the observer.

Again the solution of the retarded time is then found by taking the series of the cosine and solving for the roots of the following fourth order polynomial

$$\frac{2Rr_{o\perp}\cos(\delta\vartheta)}{4!}\left(\frac{\beta_\perp}{R}\right)^4 c\tau^4+\frac{2Rr_{o\perp}\sin(\delta\vartheta)}{3!}\left(\frac{\beta_\perp}{R}\right)^3 c\tau^3+$$
$$-\frac{2Rr_{o\perp}\cos(\delta\vartheta)}{2!}\left(\frac{\beta_\perp}{R}\right)^2 c\tau^2+(1-\beta_\parallel^2)c\tau^2-2Rr_{o\perp}\cos(\delta\vartheta)\left(\frac{\beta_\perp}{R}\right)c\tau-2\vec{r}_o\cdot\vec{\beta}_\parallel c\tau-\delta r^2=0 \tag{3.22}$$

Here it is was found not possible to factor out $\frac{\beta_\perp}{R}c\tau$: it causes the terms with $\beta_\parallel$ to be much larger than the other term, thereby dominating the solution and leading to wrong results.

Visualizing $c\tau$ or the retarded fields is rather challenging and one needs to resort to cuts (e.g. $x-z$ plane). And besides, for a single charge the number of degrees of freedom has now increased dramatically; Therefore the effect will directly be calculated on a bunch. The trajectory is given in Figure 3.23

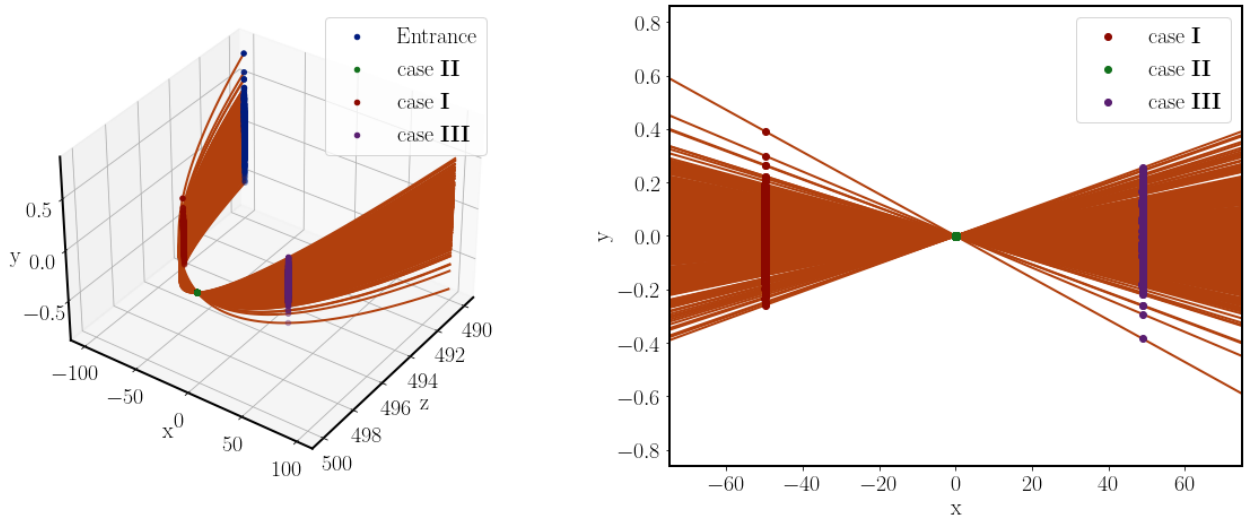

Figure 3.23: Trajectories of particles in a bunch inside a dipole magnet with $R = 500$[m], $\gamma = 100$ and $\epsilon^N{}_x = \epsilon^N{}_y = 10^{-6}$[m]. The bunch dimensions given in the *lab frame* coordinates at case **II** are $\sigma_z = \sigma_y = 5$ [μm] and $\sigma_x = 400$ [μm]. For the positions marked by the cases (**I**, **II**, **III**) the retarded time and field will be calculated.
Left: 3D view.
Right: Projection onto $x - y$ plane.

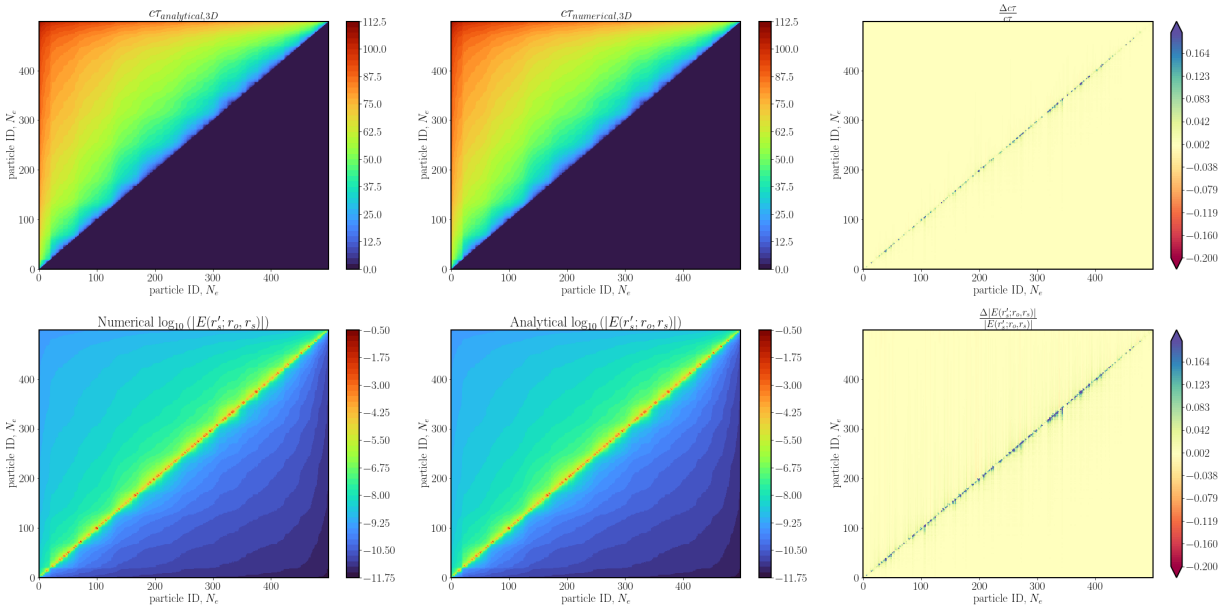

Figure 3.24: Results for case **II** in Figure 3.23, assuming that the fields have had time to reach the particles. The particle ID's ordered in the longitudinal direction. Note that exactly on the diagonal of the figures the retarded time and field are zero, because the source and the observer are the same particle, and is not visible due to the number of particles.
Top left: Analytical solution using the fourth order polynomial (Eq. 3.22).
Top middle: Numerically obtained retarded time (3.21)
Top left: Relative error in the retarded time, colour coding restricted to 20%.
Bottom left: Magnitude of the electric field calculated with the numerical result of $c\tau$ for each pair of particles. Under the diagonal only the Coulomb field contributes.
Bottom middle: Magnitude of the electric field calculated with the analytical result of $c\tau$ for each pair of particles.
Bottom right: Relative error of the electric field with the colour coding restricted to ±20%.

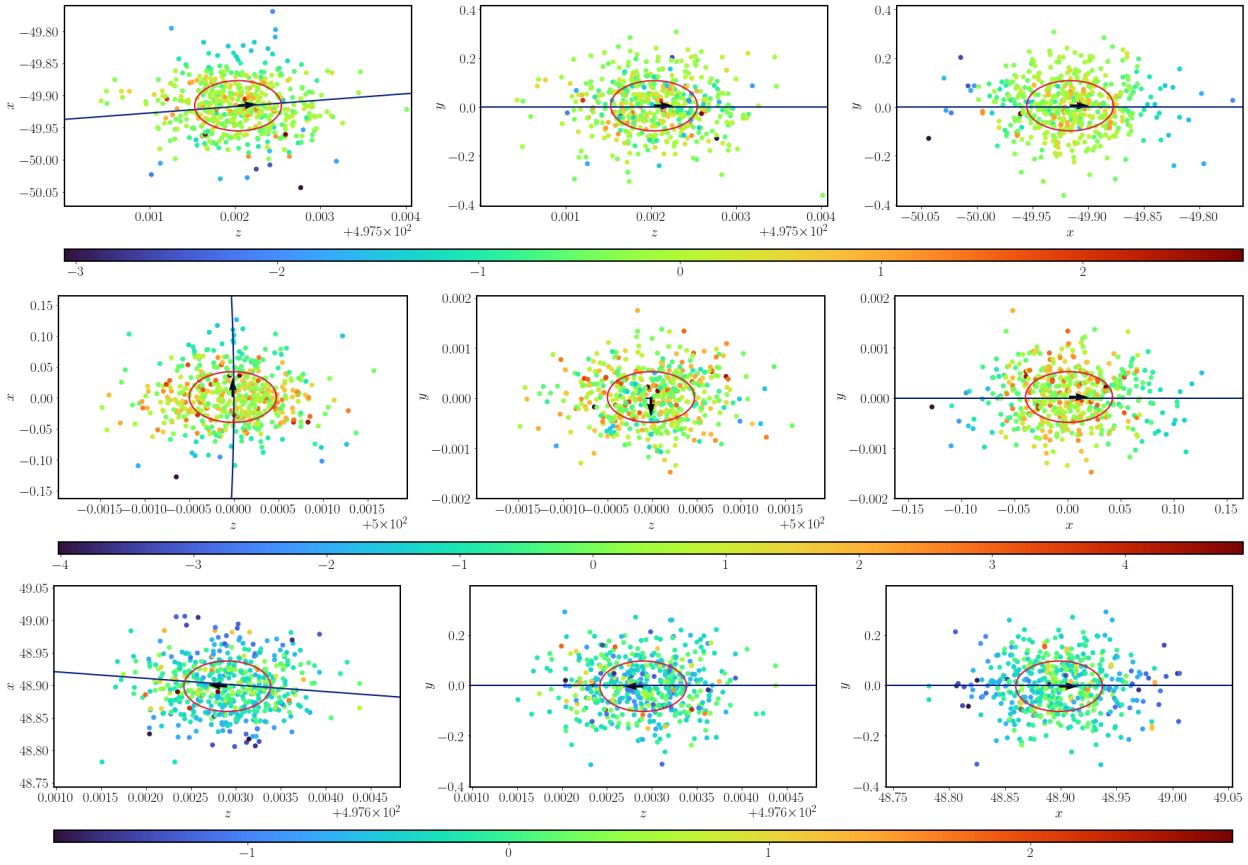

Figure 3.25: Magnitude of the electric field, using the numerical value of $c\tau$, on macroparticles for the three cases given in Figure 3.23, assuming that the fields have had time to reach the particles. Each row contains three panels with the projections of the bunch in a plane. Note the axis are in lab frame coordinates. The blue line is the reference trajectory, the red line indicates the rms bunch size and the black arrow the direction of the bunch.
Top row: Case **I** where the bunch is moving towards the focus. The particles are convergin towards the focus.
Middle row: Case **II** where the bunch is at the focus.
Bottom row: Case **III** where the bunch is moving away from the focus. Because the particles are travelling away from each other $c\tau$ is larger and therefore the field strength lower.

3.5 Discussion and prospectives

From the previous sections the following results can be used for modelling the interaction of a bunch inside a dipole

- From γ_R (Eq. 3.18) we can discern which field will be dominant in the forward direction over a given distance between particles
- From 1D solution we can estimate which part of the bunch is affected by the trailing part (time wise)
- From the 2D solution we know that particles for which $r_\perp > R$ are less affected, because it takes longest for the fields to arrive
- From 3D solution the forces on macro particles can be calculated

The second point refers to that $c\tau$ *has* to be smaller than the time a particle is inside a dipole, see Figure 3.4.

In Section 3.4.2 it was shown in detail that the Coulomb field is dominant (both longitudinally and transversely) for energies $\gamma \leq \gamma_C$ (Eq. 3.16) and that the radiation field is only dominant for $\gamma > \gamma_R$ (Eq. 3.18). In Section 3.4.3 it was shown that the particles for which $r < R$ the retarded fields are strongest. This is because the $c\tau$ is shortest.

The analytics provided here give an extension to the 1D works of Derbenev & Saldin: for energies where the radiation field is dominant the distance $c\tau$ reaches an asymptotic value, given the radius of curvature and distance between the particles.

The 3D solutions have not been examined thoroughly. For example the retarded time seems to follow a hyperbolic relation in Figure 3.24. The algorithm needs to be optimized by itself and parallelization of the calculations need to implemented to decrease the simulation time. The solutions here are given for a dipole field. With the methodology developed here it should be easy to find solutions for a bending magnet, i.e. a dipole with a field gradient.

Chapter 4

Advancements for Thomson Scattering

This chapter is dedicated to results from research conducted on emitted radiation through Thomson scattering. First the topics on the linear Thomson regimes will be discussed, which are related to the current synchrotron facilities. Whereafter the studies on the non-linear Thomson regimes.

4.1 Higher Order Transverse Modes

Currently, intensities inside a laser cavity can reach up to an order of $I_{\text{peak}} \sim 10^{14}$ ($a_0 \sim 10^{-2} - 10^{-3}$) [137, 138, 139]. Increasing the intensity further is becoming difficult in two ways: the spot size of the beam needs to be larger to avoid damage on the mirrors and the thermal dissipation into the mirrors causing deformations and excitation of higher transverse modes: a degenerate cavity [138, 139, 140, 141].

4.1.1 Cavities & Transverse Modes

One way to obtain a high intensity laser pulse is by stacking pulses inside a cavity: Each round trip of the in-cavity laser pulse an external one is added. The goal is of course to have the pulses add constructively and hence theses cavities are also called an optical resonator. A cavity where the laser pulse circulates using optical components is called a Fabry-Pérot cavity. The previously discussed transverse profile, Eq. 2.33, is not the only solution to the wave equation. Two groups can be distinguished: paraxial waves (the wavefronts are normal to the propagation) and planar waves. The former consist out of Hermite- and Laguerre-Gaussian beam solutions, i.e. they are solutions to the scalar wave equation and require the same steps . The latter leads to non-uniform transverse intensity distributions for which Bessel functions of the first kind are often given solutions [97]. Here we will focus only on the Hermite-Gaussian beams for which the transverse profile is given by

$$\Psi(x,z) = \sqrt{\frac{q_0}{q_x(z)}}\sqrt{\frac{1}{2^n n!}} H_n\left(\frac{\sqrt{2}x}{W_x(z)}\right) \exp\left[i n \arctan\left(\frac{z}{\mathscr{I}_m(q_{x,0})}\right)\right] \exp\left[-i\frac{kx^2}{2q_x(z)}\right] \tag{4.1}$$

where $W_x(z) = \sqrt{-\frac{2}{k.\mathscr{I}_m\left(\frac{1}{q_x(z)}\right)}}$ The frequency of a mode is given by

$$\nu_C = \left(C + (n+m+1)\frac{\Delta\zeta_{\text{Gouy}}}{\pi}\right)\nu_F \tag{4.2}$$

where $\nu_F = \frac{c}{2L_{\text{cavity}}}$ and is also the spectral spacing between longitudinal modes. The first couple of higher modes are given below.

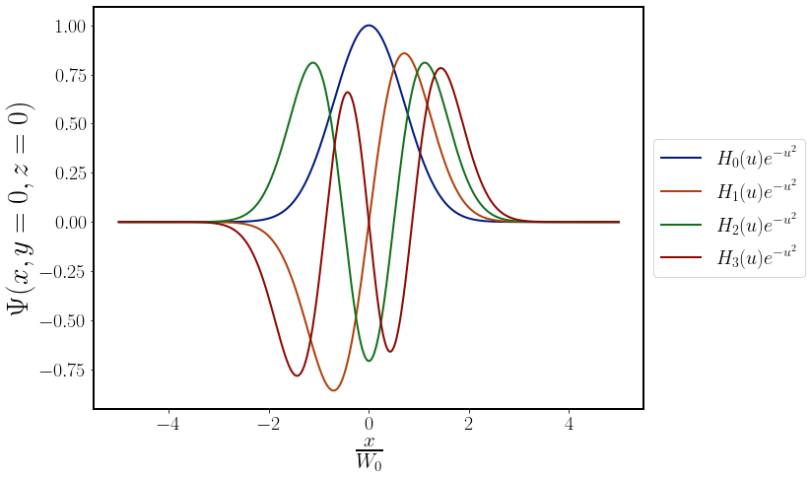

Figure 4.1: First three orders of Hermite-Gaussian pulse shapes in focus and the x-plane. The main take away is that for even harmonics there is a maximum at the centre of the pulse, while for odd harmonics the amplitude at the centre is zero.

In section 2.4.1.1 it was shown that the particles can be summed incoherently. This was under the assumption that the differences phases between particles is small and thus $\beta_i \approx \beta$. This is true for a symmetric field like the Gaussian transverse envelope (blue curve in Figure 4.1). For higher order modes this is no longer the case. Take for example the first Hermite-Gaussian mode (orange curve in Figure 4.1). For particles $x_i < 0$ the field is negative while for $x_i > 0$ it is positive. The on-axis radiation should destructively interfere as $\beta_{x<0} + \beta_{x>0} = \beta_{x<0} - |\beta_{x<0} = 0|$.

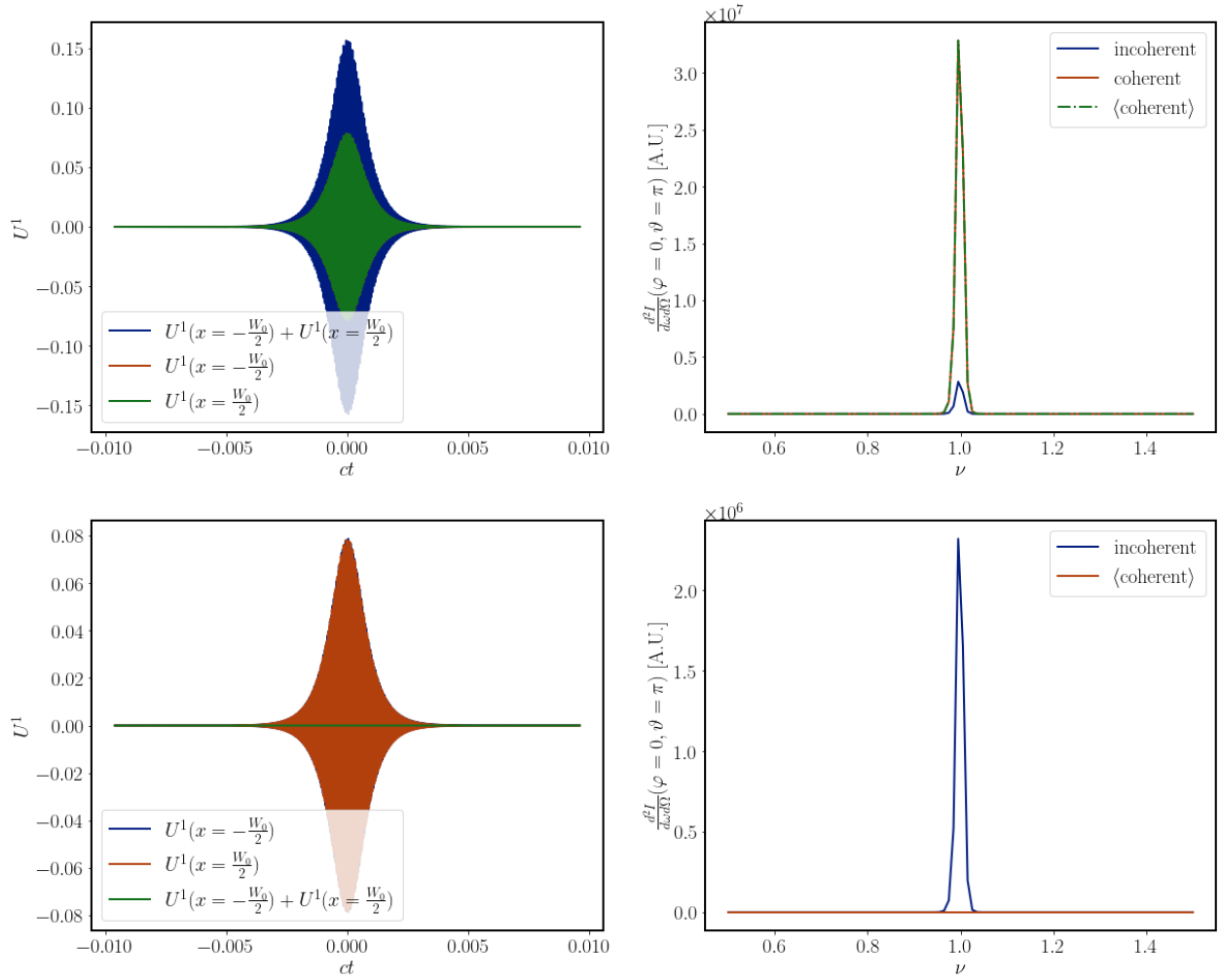

Figure 4.2: Comparison of the motion and the spectrum between $H_{0,0}$ and $H_{1,0}$. The particles are described by a line distribution: $\sigma_x = 2W_{0,x}$ and $\sigma_y = \sigma_z = 0$.
Top left: Velocity of two particles traversing $H_{0,0}$. Since the field is symmetric the sum of the velocities is twice is large.
Top right: Because all particles are in the same phase their contributions to the spectrum sum coherently.
Bottom left: Velocity of two particles (equidistant from x=0) traversing $H_{1,0}$. The field is antisymmetric leading to a phase difference of π between the two particles. Summation of the velocities thus leads to zero.
Bottom right: The spectrum is zero when it is calculated according to Eq. 2.24, since particles $x < 0$ emit with a phase shift of π compared to $x > 0$. Calculating the spectrum incoherently does not take this effect into account.

Here the amplitude of a mode is taken as the root of the power associated with it. Below we can see three examples of degenerate fields. Within the spot size of the fundamental mode the field has the same sign, meaning the incoherent summation for calculating the spectrum can be used.

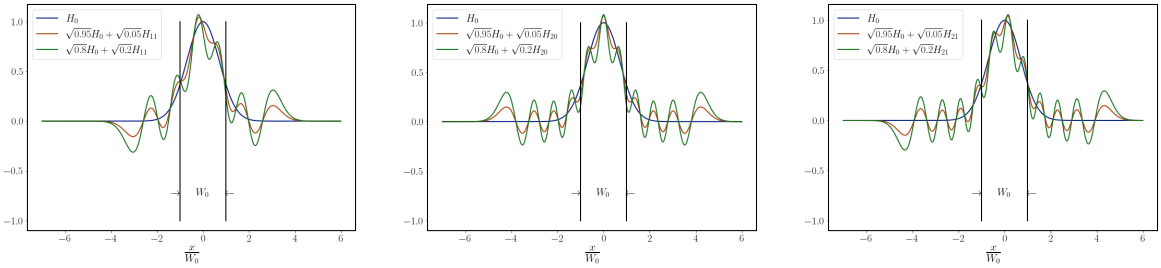

Figure 4.3: Examples of degenerate fields consisting out of the sum of the fundamental and a higher order mode. Within the spot size of the fundamental the field is positive, meaning that there are no phase dependencies in the summation in the spectrum.
Left: $H_{0,0}$ combined with $H_{11,0}$
Middle: $H_{0,0}$ combined with $H_{20,0}$
Right: $H_{0,0}$ combined with $H_{21,0}$

4.1.2 Influence of Mode Degeneracy

These modes are generally $n, m \geq 10$ and can have up to 20% of the power [139]. When a mode in one plane is excited it is accompanied by a mode in the other plane which is correlated by $m = \sqrt{n} W_{0,x}$. This degeneracy of the laser pulse has been clearly measured in [138] (their Fig. 4.). For the Thomson spectrum only a single higher order mode is considered in combination with the fundamental one. The results of the emitted radiation collected within a $\frac{1}{6\gamma}$ cone are given below.

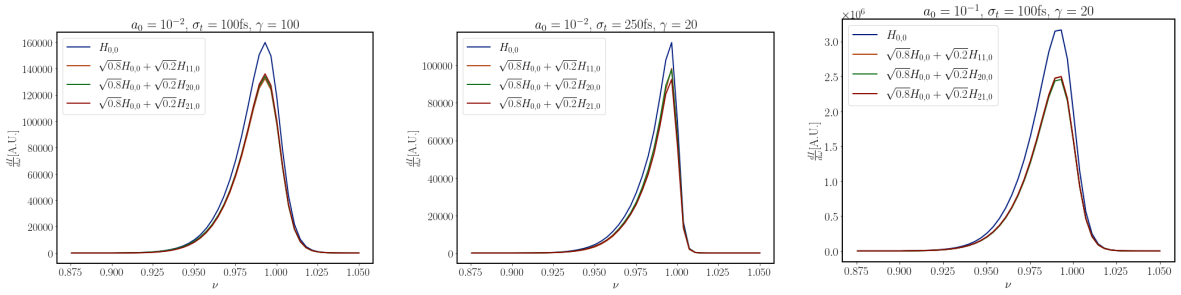

Figure 4.4: Results of simulations for a degenerate cavity. Three different combinations have been tried which have been observed experimentally. The energy of the particle, the length of the laser pulse and the intensity have been varied. In each case the spectrum of the combined modes is 20% lower than the fundamental one, and they are indistinguishable from one another.

Interestingly there is very little difference between the different degenerate modes in the spectrum. The absolute bandwidth does not change. The energy distribution $\frac{dI}{d\Omega}$ have been checked, but also here one could not tell that a mixed mode laser collided with the electrons, except for the amplitude.

4.2 Discussion

That the results for a degenerate cavity are underwhelming is actually a good sign: for another two orders of increase in the power inside a cavity does not lead to a deterioration in the bandwidth of the Thomson spectrum. The radiated energy does decrease with the amount that is in the higher order mode, but the distribution of the energy remains the same.

4.3 Compensating Energy Spread of Particles

In general a narrow bandwidth photon source is desired for experiments [10, 11, 142]. To achieve this with Thomson scattering it requires a priori to operate in the linear regime [143] in combination with a small aperture (due to the angular dependency of the emitted radiation, see Figure 2.9). The use of quasi-monochromatic laser pulses puts the remaining constraints (to achieve the narrow bandwidth source) on the electron bunch parameters: spot size, divergence and energy spread. These constraints are often met by reducing the bunch charge, in both RF and PWA structures, and consequently the radiated energy per bunch is reduced.

The obvious question then arises if there is a way to increase the number of particles by easing the constraints and use the laser pulse to compensate the broadening. From the aforementioned electron parameters only the energy spread can be eased under the condition that it is spatially correlated. Especially PWA electron bunches are characterised by such a correlation due to the acceleration gradient: energy spread in the direction of propagation from few to tens of percent [56, 53, 57, 58, 59]. Also for traditional radiofrequency structures this effect takes place: the difference in the energy of a bunch depends on its length and therefore on the phase of the accelerating wave.

If we look back at Eq. 2.62 we see two possible options to compensate a correlated energy spread:

1. use the non-linear broadening to keep $\frac{\gamma^2}{1+(a)^2}$ constant [144].
2. use a chirp on the laser pulse such that $\gamma^2\omega_l$ remains constant [145]

The first method requires that a_0 is substantially different from 0 and thus leads inevitably to non-linear broadening of the spectrum. In [144] the laser pulse and electron bunch collide under a 90 deg angle, reducing the interaction time/length of an electron in the pulse. In addition the profile of the laser pulse needs be shaped such that it matches the energy spread distribution. For symmetric pulses as described in Sec. 2.5.2 this actually puts a limit on the electron energy distribution and furthermore only the section of the pulse can be used that matches the energy distribution.

The second method has the attractive attribute that it can work in the linear regime as the emitted wavelength depends linearly on the laser frequency. To find the chirp condition we first generalize Eq. 2.62 for many particles by substituting the bunch energy distribution. Then we find

$$\frac{\omega}{c} = \frac{\omega_{l,0}}{c}\langle\gamma\rangle^2(1+\beta)^2 = \frac{\partial\eta(X)}{\partial\zeta}\frac{\gamma(X)^2(1+\beta)^2}{1+(a)^2} \tag{4.3}$$

$$\frac{\partial\eta(X)}{\partial\zeta} = \frac{\omega_{l,0}}{c}\left(\frac{\langle\gamma\rangle}{\gamma(X)}\right)^2(1+(a)^2) \tag{4.4}$$

where X is the spatial coordinate of the (correlated) energy spread of the electrons. From the last equation we see that, in principle, any energy distribution can be compensated through a specific chirp. Before solving η and constructing geometries of the interaction, lets first establish the requirements for the laser pulse's bandwidth.

In the otherwise ideal conditions the bandwidth of the Thomson spectrum equals the Fourier limited bandwidth and is inversely proportional to the length of the pulse $\frac{\sigma_{\lambda_l}}{\lambda_l} \propto \frac{1}{N_c}$ [146]. The minimum pulse length for the Fourier limited bandwidth to be smaller than the contribution of the energy spread of $\frac{\sigma_\gamma}{\gamma} = 0.02$ is $N_c \geq 60$ ($\sigma_t \geq 200$ fs). Figure 4.5 shows the results of several numerical simulations for ideal electron bunches and one with a large energy spread. The latter results in the same bandwidth as a ideal electron bunch colliding with a short laser pulse.

To compensate the energy spread of an electron bunch the bandwidth of the laser pulse needs to equal $\frac{\sigma_{\lambda_l}}{\lambda_l} = 2\frac{\sigma_\gamma}{\langle\gamma\rangle}$. Thus for an energy spread of $\frac{\sigma_\gamma}{\langle\gamma\rangle} = 0.02$ (FWHM) requires a bandwidth of $\frac{\sigma_{\lambda_l}}{\lambda_l} = 0.04$ (FWHM). With the advent of chirped laser amplification these bandwidths are readily available, see Table 4.1. The spectrum of these laser pulses are Gaussian-like in shape, but even broad bandwidths with a flat top intensity profile have been demonstrated [147, 148]. The uncompressed pulse in CPA schemes

have an amplitude on the order of $a_0 \sim 10^{-3} - 10^{-1}$, under the assumption that $W_0 = 20$ [μm]. For the remainder of this research the amplitude of the laser pulse is chosen to be $a_0 = 10^{-2}$.

	CPA lasers before compression			
	$\frac{\sigma_{\omega_l}}{\omega_{l,0}}$	E_{nergy} [Joule]	σ_t (FWHM)	a_0
[149]	0.02	$800 \cdot 10^{-3}$	$85 \cdot 10^{-15}$	0.85
[150]	0.625	$0.3 \cdot 10^{-3}$	$30 \cdot 10^{-12}$	10^{-3}
[151]	0.04	$700 \cdot 10^{-6}$	$45 \cdot 10^{-15}$	0.03
[152]	0.04	3.5	$400 \cdot 10^{-12}$	0.03
[58]	0.04	45	$2 \cdot 10^{-9}$	0.04
[105]	0.03	70	$100 \cdot 10^{-12}$	0.7

Table 4.1: Selection of published works on chirped pulse amplification. For the calculation of a_0 it is assumed that the laser pulse is focussed down to $W_0 = 20\mu$m.

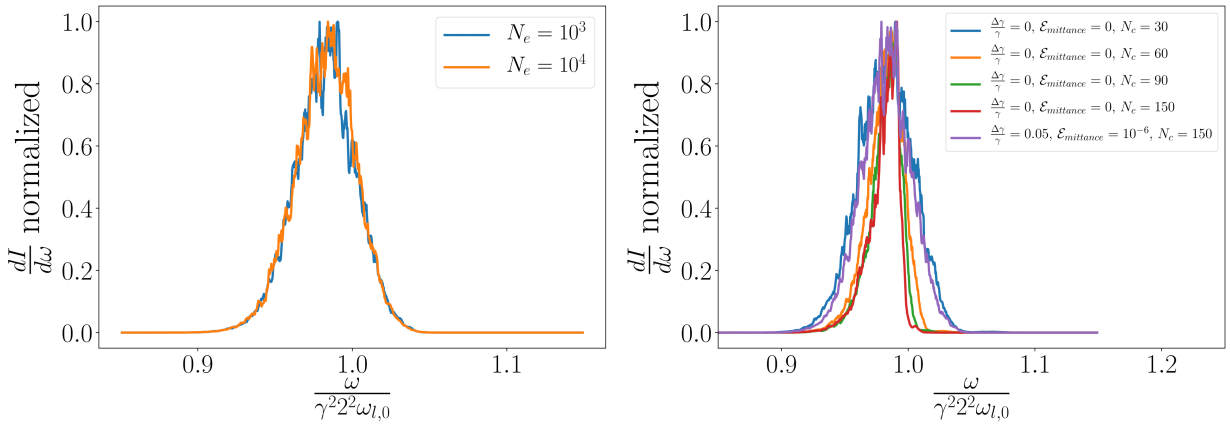

Figure 4.5: Numerical results of Thomson spectra for various laser pulse lengths and an ideal electron bunch (no energy spread, no divergence) and a long laser pulse colliding with an electron bunch with a 5% energy spread. The spectrum becomes more narrow as the pulse length increases, i.e. the Fourier limited bandwidth. To use a chirped laser pulse for the compensation of the energy spread of an electron bunch you want the following condition $\frac{\sigma_{\omega_l}}{\omega_{l,0}} \ll 2\frac{\sigma_\gamma}{\gamma}$.

Next we can focus on the geometry. The chirped laser pulses presented above have their frequency correlated to the propagation direction. Simply colliding the chirped pulse and beam head-on will have the opposite effect: an electron will experience all frequencies and thus broadening the spectrum. Instead, one is required to have a collision angle such that an electron only experiences the frequency matched to its energy. To obtain analytical solutions the interaction region will be modelled as a plane wave travelling in $\hat{z}$. To achieve this physically is by adding a second pulse that cancels the transverse momentum, see Figure 4.6 left panel. A different geometry can be achieved by first reflecting the chirped pulse on a grating. This effectively rotates the axis of the frequency content into the transverse direction. Of course the electron bunch's energy spread must now also be in the transverse direction. The right panel of Figure 4.6 depicts this geometry schematically. I would like to attribute original idea of the longitudinal geometry to Matt Zepf and the transverse geometry to Vittoria Petrillo. Both geometries will be investigated thoroughly in the next sections. To make the analytics more approachable the effect of a linear chirp is considered. This is justified because higher order terms have effect over large scales, while

a single electron should only interact on a small scale.

$$\frac{\omega_l(X)}{c} = A + BX \tag{4.5}$$

Then factor B can be expressed as the total (laser) bandwidth divided by the characteristic length of the bunch.

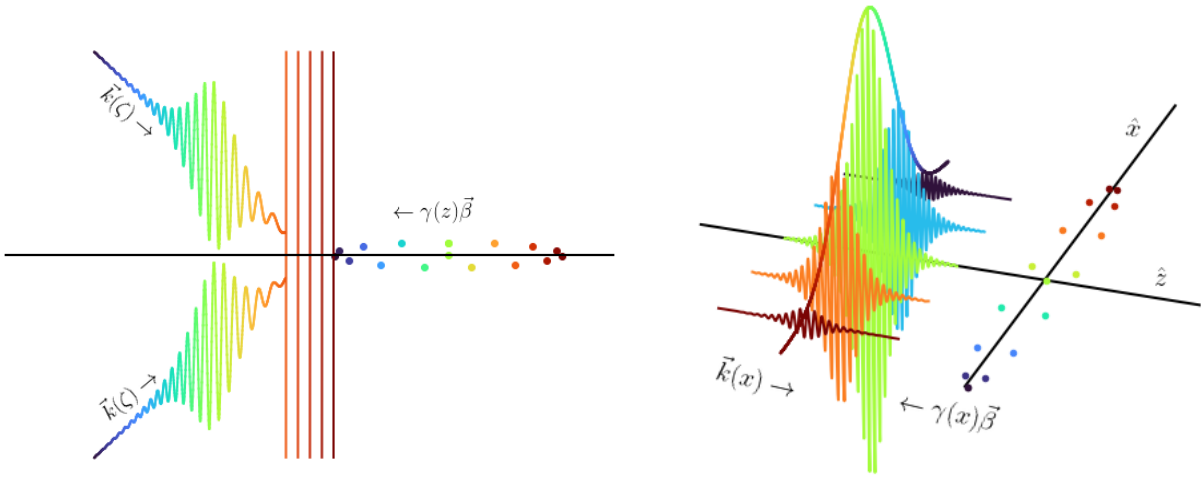

Figure 4.6: Schematic of energy spread compensation by using a chirped laser pulse. Each electron interacts with a portion of the laser pulse that has a frequency matched to its energy such that the frequency of the emitted radiation is constant.
Left: The chirp is along the propagation direction of the laser pulse (Longitudinal chirp). In order for a single electron to experience its matched laser frequency the collision requires a collision angle. The transverse momentum of the laser pulse can be negated by using two of them as indicated in the figure. During the interaction, i.e. where the pulses combine, the plane wave approximation can be used where the pulse travels in $+\hat{z}$.
Right: The chirp is perpendicular to both the propagation- and polarization direction.

4.3.1 Longitudinal Frequency Modulation $\eta(\gamma(z))$

First, let's narrow down what properties the laser pulse can have in this configuration. The chirp of the laser is along the direction of propagation. From the Lorenz gauge we see that both linear and circular polarization can be used. However, it cannot compensate the non-linear broadening as it would require a frequency modulation along the same axis (see Section 2.6.4). Thus we are only interested in the linear regime for which the $(a)^2$ term in Eq. 4.4 can safely be ignored. The interaction region (L_I) is where the two chirped laser pulses overlap and act as a plane wave travelling in $\hat{z}$. This will lead to interference patterns, but are for now discarded. What we require is that the frequency remains constant from the moment an electron enters L_I until it exits. This means that a frequency needs to occupy a length within the pulse of $\frac{1+\beta}{\beta} L_I$ as is shown in Figure 4.7. Thus the chirp condition is found to be

$$\frac{\partial \eta}{\partial \zeta} \equiv \frac{\omega_l(z)}{c} = \frac{\omega_{l,0}}{c} \left(\frac{\langle \gamma \rangle}{\gamma \left[\frac{1+\beta}{\beta} z \right]} \right)^2 \tag{4.6}$$

where $\gamma\left[\frac{1+\beta}{\beta}z\right]$ is the rescaled electron energy distribution. The difference frequencies experienced by a single electron traversing the interaction region is

$$\begin{aligned}\Delta\omega_{\gamma,\epsilon^N} = &\quad \omega_l(ct=0, z=-\tfrac{LI}{2}) - \omega_l(ct_1, z=\tfrac{LI}{2}) \\ = &\quad B(ct_1 + L_I)\end{aligned} \tag{4.7}$$

The time can be approximated, for an electron with a divergence angle (α_{ϵ^N}), as $ct_1 \approx \frac{L_I}{\beta\cos(\alpha_{\epsilon^N})}$. Thus we find

$$\frac{\Delta\omega_{\gamma,\epsilon^N}}{\omega_{l,0}} = \Delta\omega_l \frac{1+\beta\cos(\alpha_{\epsilon^N})}{\beta\cos(\alpha_{\epsilon^N})}\frac{L_I}{L_B} \tag{4.8}$$

where the approximation of $B = \frac{\Delta\omega_l}{L_B}$ has been used. What can be concluded from the relation above is that the frequency content seen by an electron is negligible due to divergence. For example the difference between $\alpha_{\epsilon^N} = 0\,\text{deg}$ and $\alpha_{\epsilon^N} = 10\,\text{deg}$ is on the order of 10^{-2}. More crucial is the ratio between the interaction region and the bunch length. This can also be reformulated as the energy gradient of the electron bunch scaled to the interaction region. How this relation influences the spectrum will be further explained under the simulation results after concluding the geometry. Using the slowly varying amplitude approximation for Eq. 4.8 we find the frequency modulation to be

$$\eta(\zeta) = \frac{\omega_l(\zeta)}{c}\zeta \tag{4.9}$$

An example of this phase is illustrated in the right panel of Figure 4.7.

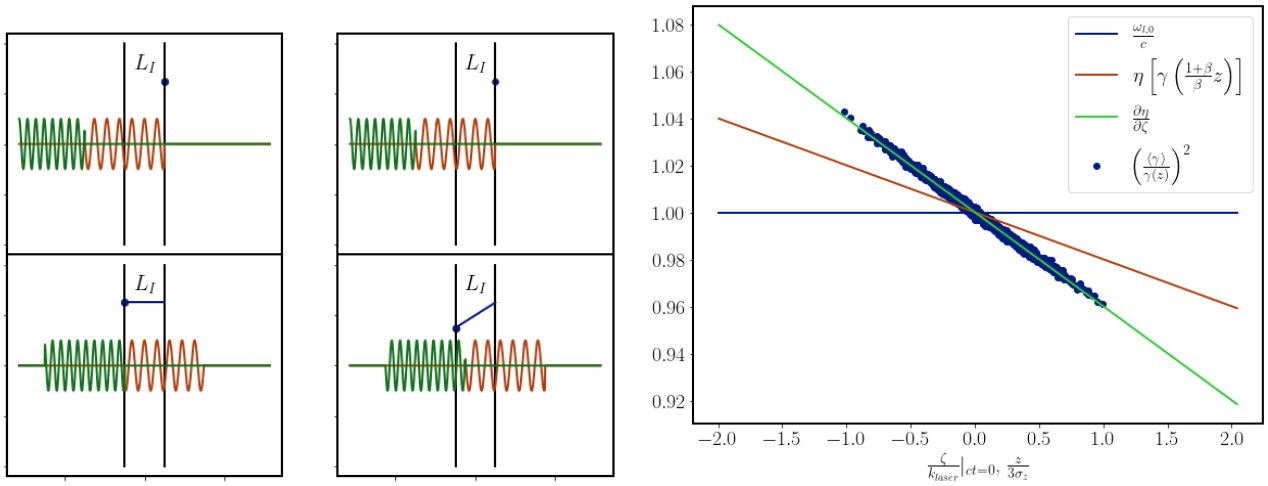

Figure 4.7: Schematic overview of the dynamics of a single electron colliding with a laser pulse with a longitudinal chirp (see left panel of Figure 4.6).
Left: An electron, without transverse momentum, enters the interaction region (L_I). At this instance the region is filled with a single frequency wave matched to the electron's energy. Because the wave and electron counter propagate, the length of the laser pulse containing ω needs to be $\frac{1+\beta}{\beta}L_I$.
Middle: When an electron has transverse momentum the time it takes to traverse the interaction region is longer. Thereby the electron can see wavelengths that are not matched to its energy.
Right: Phase (Eq. 4.9) and frequency (Eq. 4.6) of the laser pulse as function of the electron's energy. Note that the pulse and electrons counter propagate and thus an electron left of the figure will encounter the frequency on the right of the figure.

So far the interaction region L_I has been considered as an abstract entity containing a plane wave pulse. To obtain a physical system we will use two Gaussian beams crossing each other. Of course the spot of the laser pulse should be comparable to that of the electron bunch. Thus the two variables L_I &

W_0 thus put a constraint on the angle of incidence, given by

$$\alpha = \sin^{-1}\left(\frac{2\frac{3}{\sqrt{2}}W_0}{L_I}\right) \tag{4.10}$$

Figure 4.8 shows this relation and an example of realised the geometry. This angle of incidence reduces the frequency conversion of Thomson scattering. For the on-axis radiation the peak frequency is given by

$$\omega = (1+\beta\cos(\alpha))(1+\beta)\gamma^2\omega_{l,0} \tag{4.11}$$

Finally, the full set of equations to model the laser pulses are given by

$$\zeta = \frac{\omega_{l,0}}{c}(ct - z') \tag{4.12}$$
$$\eta = \frac{\omega_l(\zeta)}{c}\zeta \tag{4.13}$$
$$x'(\alpha) = z\sin(\alpha) + x\cos(\alpha) \tag{4.14}$$
$$z'(\alpha) = z\cos(\alpha) - x\sin(\alpha) \tag{4.15}$$
$$\Psi(\vec{r}) = \frac{G(r(\alpha))+G(r(-\alpha))}{2} \tag{4.16}$$
$$G(r(\alpha)) = \frac{q(0)}{q(z')}\exp\left[-i\frac{\omega_{l,0}}{c}\frac{x'^2+y^2}{2q(z')}\right] \tag{4.17}$$
$$q(z) = q_0 + z \tag{4.18}$$
$$q_0 = i\frac{W_0^2\frac{\omega_{l,0}}{c}}{2} \tag{4.19}$$
$$\mathscr{E}(K_\mu X^\mu) = 1 \tag{4.20}$$

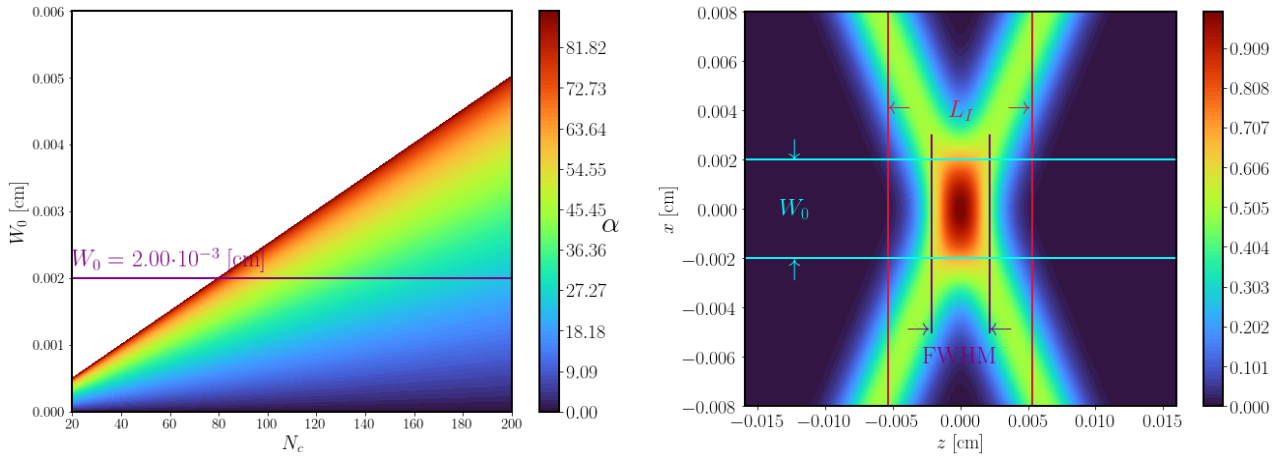

Figure 4.8: Realization of the interaction region for a longitudinal chirp $\eta(\gamma(z))$.
Left: Constraint on the angle of incidence for a given interaction length (L_I) and width of the laser pulse W_0. Reducing the angle of incidence, for a fixed interaction length, also reduces the spot size.
Right: Top view of the geometry of the two laser pulses. Here $L_I = 106.6\cdot10^{-4}$ [cm] ($N_c = 100$), $W_0 = 20\cdot10^{-4}$ [cm] and $\alpha = 52.75$ deg. Note that the length of the laser pulse is longer than L_I.

Simulation Results

Figure 4.9 shows the simulation results for on-axis radiation where the energy spread and interaction length have been kept constant, but the length of the bunch has been varied; thus changing the energy gradient of the bunch. What we see is that if the bunch is much longer than the interaction region the

spectrum reaches the plane wave - ideal electron bunch limit asymptotically. The reason for this is easiest understood starting with the case where the bunch is smaller than the interaction region: an electron in the bunch experiences the full bandwidth of the laser pulse as it traverses the interaction region. This, combined with the energy spread, results in an even broader and less intense spectrum. This does not mean that this method is not adequate for the bandwidth compensation, but rather sets a physical limit to the geometry; connecting the possible interaction length with the energy gradient of the bunch. In the end it is a design problem where the interaction length is easier to manipulate, thus given an electron bunch the possible interaction length is $L_I = \frac{1}{5}\sigma_z$. Combining Eq. 2.64 with the above relations the bandwidth of the Thomson spectrum for the LC case scales as

$$\frac{\sigma_\omega}{\omega} = \sqrt{\left(\Theta + \frac{\sigma_\epsilon}{\sigma_{W_b}}\right)^2 + \left(\frac{\Delta\omega_{\gamma,\epsilon^N}}{6\omega_{l,0}}\right)^2 + \left(\frac{\sigma_{\omega_{l,0}}}{\omega_{l,0}}\right)^2}, \tag{4.21}$$

where $\frac{\sigma_{\omega_{\gamma,\epsilon^N}}}{\omega_{l,0}} = 2\frac{\sqrt{2}\sigma_\gamma}{\gamma}\frac{L_I}{L_B}$

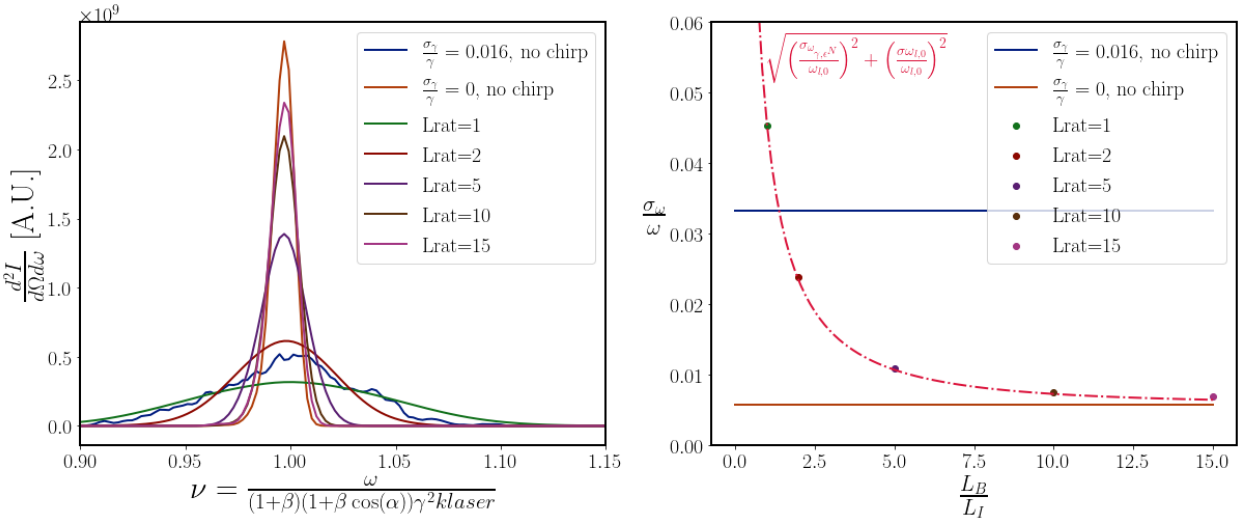

Figure 4.9: Simulation results for on-axis Thomson scattering for longitudinal chirp.
Left: On-axis spectra for the following cases: a quasi-monochromatic pulse - ideal electron bunch (orange), a quasi-monochromatic pulse - chirped electron bunch (blue), a chirped pulse - chirped electron bunch with varying ratios of interaction- and bunch length.
Right: Bandwidth of the on-axis spectrum as function of the ratio between the bunch length & interaction region. When the bunch is shorter than the L_I the spectrum is broader than when the same electron bunch collides with a monochromatic laser pulse collides, see blue in the left panel. This is because an electron experiences a large range of laser frequencies.

For the simulations calculating the energy collected on a screen we use electron parameters $\sigma_x = \sigma_y = 20$ [μm], $\sigma_z = 30$ [μm], $\epsilon^N{}_x = \epsilon^N{}_y = 10^{-6}$ [mm mrad], $\gamma = 10^3$, and $\frac{\sigma_\gamma}{\gamma} = 0.03$. An additional case of an unmatched chirp is provided as well; the bunch's energy spread is kept the same but the frequency modulation is calculated to be that of $\frac{\sigma_\gamma}{\gamma} = 0.05$.

First an electron bunch with an idealized energy correlation has been used, see left panel of Figure 4.10. For this the monochromatic Thomson spectrum is retrieved, both in photon numbers and in bandwidth. The number of photons emitted is roughly the same for all cases. For a more realistic bunch the ideal Thomson spectrum is not retrieved because each slice of the electron bunch inside the interaction region now has a finite energy spread.

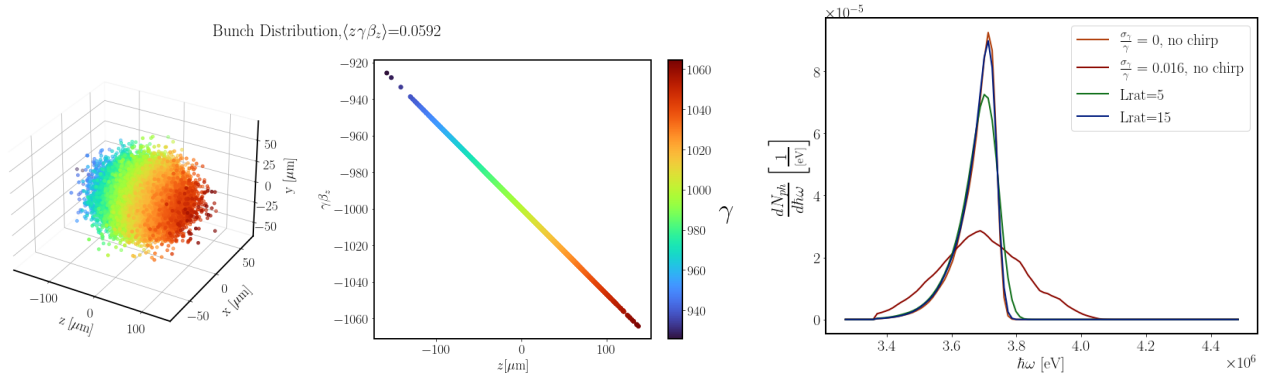

Figure 4.10: Simulation results of Thomson scattering, where the energy correlation of the electron bunch is compensated by a chirped laser pulse along the propagation direction.
Left: Particle Distribution.
Middle: Longitudinal position and momentum correlation.
Right: Energy collected within an azimuthal angle of $\frac{1}{6\gamma}$. The photon numbers for 10^3 particles and bandwidth are: no energy spread (orange) $N_{ph} = 9.4$, $\frac{\sigma_\omega}{\omega} = 1.61 \cdot 10^{-2}$, no chirp (red) $N_{ph} = 9.0$, $\frac{\sigma_\omega}{\omega} = 3.53 \cdot 10^{-2}$), matched chirp and $L_{rat} = 5$ (green) $N_{ph} = 9.6$, $\frac{\sigma_\omega}{\omega} = 1.78 \cdot 10^{-2}$), matched chirp (blue) and $L_{rat} = 15$ $N_{ph} = 9.6$, $\frac{\sigma_\omega}{\omega} = 1.65 \cdot 10^{-2}$).

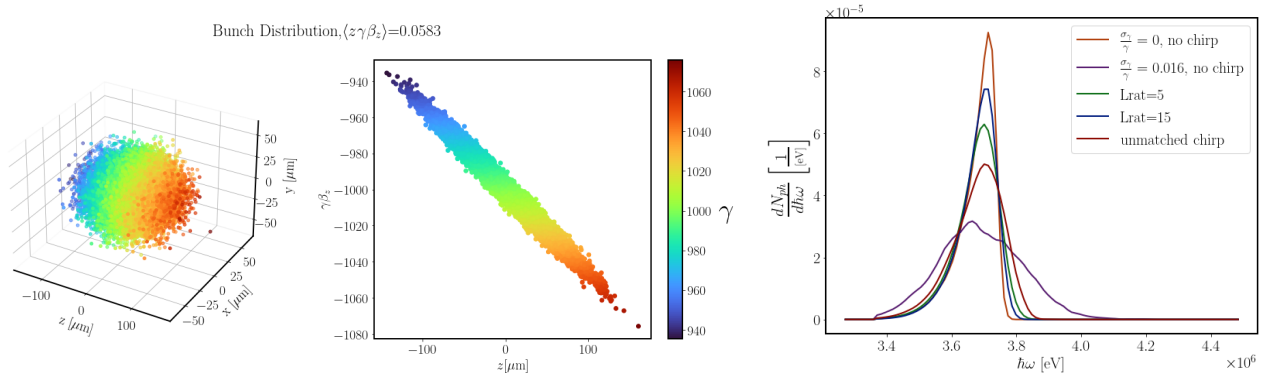

Figure 4.11: Simulation results of Thomson scattering, where the energy correlation of the electron bunch is compensated by a chirped laser pulse along the propagation direction.
Left: Particle Distribution.
Middle: Transverse position - Longitudinal momentum correlation.
Right: Energy collected within an azimuthal angle of $\frac{1}{6\gamma}$. The photon numbers for 10^3 particles and bandwidth are: no energy spread (orange) $N_{ph} = 9.4$, $\frac{\sigma_\omega}{\omega} = 1.61 \cdot 10^{-2}$; no chirp (purple) $N_{ph} = 9.7$, $\frac{\sigma_\omega}{\omega} = 3.45 \cdot 10^{-2}$); matched chirp (green) and $L_{rat} = 5$ $N_{ph} = 9.2$, $\frac{\sigma_\omega}{\omega} = 1.83 \cdot 10^{-2}$); matched chirp (blue) and $L_{rat} = 15$ $N_{ph} = 9.2$, $\frac{\sigma_\omega}{\omega} = 1.83 \cdot 10^{-2}$); unmatched chirp and $L_{rat} = 15$ $N_{ph} = 9.2$, $\frac{\sigma_\omega}{\omega} = 2.16 \cdot 10^{-2}$).

4.3.2 Transverse Frequency Modulation $\eta(\gamma(x))$

This geometry shares the same idea as the transverse gradient undulator, see [153, 154, 155] and references therein. A transverse frequency modulation can be realized only for a linearly polarized laser pulse and the chirp is orthogonal to the polarization axis. In fact this is what is shown in Figure 4.6. To start of with the model, we will collide an electron bunch with its correlated energy spread in $\hat{x}$ head-on with a

laser pulse with an amplitude $a_0 \ll 1$. The chirp condition is then simply

$$\frac{\partial \eta}{\partial \zeta} \equiv \frac{\omega_l(x)}{c} = \frac{\omega_{l,0}}{c}\left(\frac{\langle\gamma\rangle}{\gamma(x)}\right)^2 \tag{4.22}$$

$$\eta = \frac{\omega_l(x)}{c}\zeta \tag{4.23}$$

For this geometry no additional requirements are needed. So lets look into what frequencies an electron experiences due to emittance/divergence of the bunch or a collision angle.

$$\begin{aligned}\Delta\omega_{\alpha,\epsilon^N} &= \omega_l(ct=0, x=x0, z=-\tfrac{L_{pulse}}{2}) - \omega_l(ct_1, x1, z=\tfrac{L_{pulse}}{2}) \\ &= B\Delta x\end{aligned} \tag{4.24}$$

If we now take that the approximation that $\tan(\alpha) = \frac{\Delta x}{L_{pulse}}$ and $B = \frac{\Delta\omega_l}{W_b}$ than the we find

$$\Delta\omega_{\alpha,\epsilon^N} = \Delta\omega_l \tan(\alpha)\frac{L_{pulse}}{W_b} \tag{4.25}$$

If the angle is caused only by the divergence/emittance it is safe to say that this quantity is negligible. For an angle of incidence we will compare the value from the equation above with Eq. 4.8 reaching the PW limit. Thus, for a 100 fs pulse (FWHM) the maximum incidence angle is 4deg and for a 100 ps pulse the maximum incidence angle is 0.05deg. These angles are larger than is typical in Thomson experiments, and therefore off no concern for the remainder of this section. The bandwidth of the emitted radiation can be approximated as

$$\frac{\sigma_\omega}{\omega} = \sqrt{\left(\Theta + \frac{\sigma_\epsilon}{\sigma_{W_{bunch}}}\right)^2 + \left(\frac{\Delta\omega_{\alpha,\epsilon^N}}{6\omega_{l,0}}\right)^2 + \left(\frac{\sigma_{\omega_l}}{\omega_{l,0}}\right)^2}, \tag{4.26}$$

From a theoretical point of view a frequency modulation to compensate the non-linear broadening (Section 2.6.4)) is compatible with this geometry, as the two frequency modulations are along different axis. The chirp condition is now given by

$$\frac{\partial \eta}{\partial \zeta} = \frac{\omega_{l,0}}{c}\left(\frac{\langle\gamma\rangle}{\gamma(x)}\right)^2 (1 + (a)^2) \tag{4.27}$$

How to practically obtained such a frequency modulation is unknown to me, and therefore left out of this thesis, but simulation results can be found in [145]. Finally, the shape of the laser pulse is given by

$$\Psi(\vec{r}) = \frac{q(0)}{q(z)} \exp\left[-i\frac{\omega_{l,0}}{c}\frac{x^2+y^2}{2q(z)}\right], \tag{4.28}$$

$$\mathscr{E}(\zeta) = \operatorname{sech}\left(\frac{\zeta\sqrt{2}}{N_c}\right) \tag{4.29}$$

Simulation Results

For the simulations calculating the energy collected on a screen we use electron parameters $\sigma_x = \sigma_y = 15$ [μm], $\sigma_z = 30$ [μm], $\epsilon^N{}_x = \epsilon^N{}_y = 10^{-6}$ [mm mrad], $\gamma = 10^3$, and $\frac{\sigma_\gamma}{\gamma} = 0.03$. These are typical from plasma accelerated bunches as provided in Table 1.2. The collected radiation is within an azimutal angle of $\frac{1}{6\gamma} \approx 0.17$[mrad].

For the electron bunch with an idealized energy correlation the transverse chirp works excellent. It does not require any modifications and can retrieve the monochromatic photon number and bandwidth.

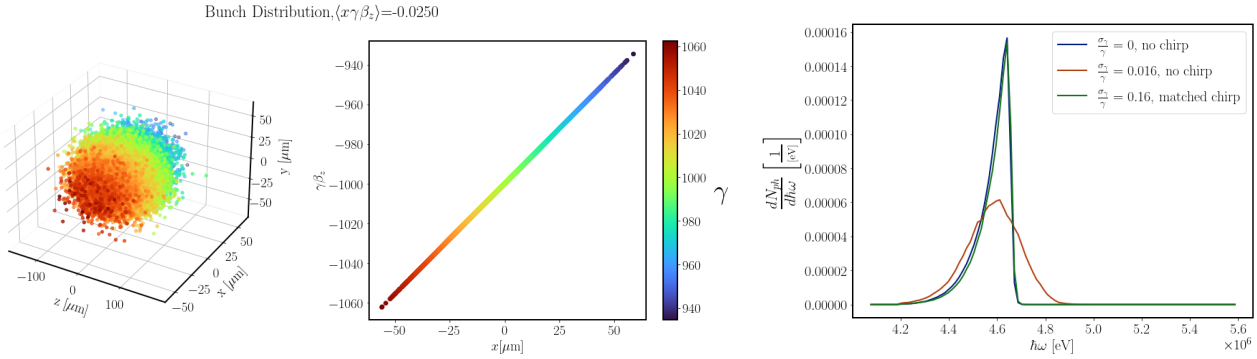

Figure 4.12: Simulation results of Thomson scattering, where the energy correlation of the electron bunch is compensated by a chirped laser pulse along the propagation direction.
Left: Particle Distribution.
Middle: Transverse position - Longitudinal momentum correlation.
Right: Energy collected within an azimuthal angle of $\frac{1}{6\gamma}$. The number of photons per 10^3 particles and bandwidth are: no energy spread (blue) $N_{ph} = 17.2$, , $\frac{\sigma_\omega}{\omega} = 1.62 \cdot 10^{-2}$; no chirp (orange) $N_{ph} = 16.3$, , $\frac{\sigma_\omega}{\omega} = 2.42 \cdot 10^{-2}$; matched chirp (green) $N_{ph} = 16.8$, , $\frac{\sigma_\omega}{\omega} = 1.55 \cdot 10^{-2}$.

The electron bunch so far has been modelled ideally; there is only a single energy at x. To obtain the energy spread in the transverse direction, either from a bunch with an uncorrelated - or a correlated longitudinal energy spread, one could use a (magnetic) dipole. Here we will not go into a specific beamline, but use an electron bunch that has similar characteristics as given for the study of the transverse undulator [155].

For a more realistic electron bunch a finite energy spread encounters a frequency, matched to the average in that transverse position. This decreases the effectiveness, but still good results are obtained.

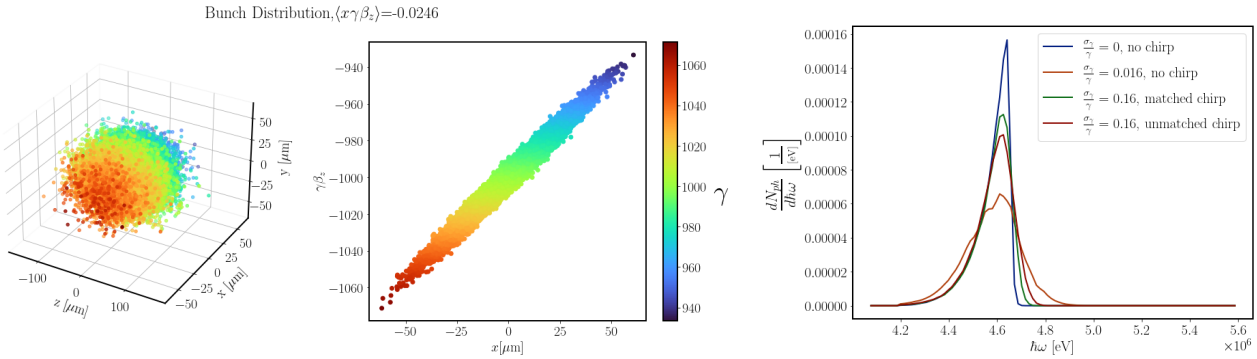

Figure 4.13: Simulation results of Thomson scattering, where the energy correlation of the electron bunch is compensated by a chirped laser pulse along the propagation direction.
Left: Particle Distribution.
Middle: Transverse position - Longitudinal momentum correlation.
Right: Energy collected within an azimuthal angle of $\frac{1}{6\gamma}$. The number of photons per 10^3 particles and bandwidth are: no energy spread (blue) $N_{ph} = 17.1$, , $\frac{\sigma_\omega}{\omega} = 1.57 \cdot 10^{-2}$; no chirp (orange) $N_{ph} = 16.7$, , $\frac{\sigma_\omega}{\omega} = 2.45 \cdot 10^{-2}$; matched chirp (green) $N_{ph} = 16.7$, , $\frac{\sigma_\omega}{\omega} = 1.70 \cdot 10^{-2}$; unmatched chirp (red) $N_{ph} = 17.3$, , $\frac{\sigma_\omega}{\omega} = 1.83 \cdot 10^{-2}$.

4.4 Discussion

The longitudinal and transverse energy compensation geometries have each their own merits and complications. Both can retrieve the monochromatic Thomson spectrum for an electron bunch with an idealized energy correlation. For a realistic electron bunch, that includes some uncorrelated energy spread, efficiency of the compensation scheme is decreased. The transverse geometry gives twice the photon number compared to the longitudinal one. For a 1nC bunch the order of magnitude of emitted photons is $> 10^7$.

Longitudinal $\eta(\gamma(z))$

The experimental implementation of a longitudinally chirped laser pulse for Thomson scattering is quite straightforward for an electron bunch obtained by laser plasma wake-field acceleration. The CPA laser pulse before the compression stage is exactly that what is needed for the scattering event: Joule-class with a bandwidth compatible to the energy spread of produced electron bunches. This makes the timing of colliding the electron bunch and laser pulse more synchronous as well.

A collision angle is required in order for an electron to experience a single frequency of the pulse. This angle depends on the interaction length and therefore the gradient of the energy spread of the electrons. This angle of incidence results in a lower emitted frequency than of head-on collision and should be kept in mind in the experimental design.

Here two pulses were used to maintain a clear connection to the abstraction used in the theory. When $a_0 \ll 1$ it is safe to use a single laser pulse, as the ponderomotive forces are negligible.

The timing of collision is rather important for this geometry. A time deviation of the arrival of either the laser pulse or electron bunch, i.e. jitter, results in a shift of the Thomson frequency for a linear energy correlation, but does not alter the bandwidth significantly. This seems less relevant for a full optical system where the bunch and Thomson scattering are done with a single CPA laser pulse. When a different laser pulse is used to obtain an electron bunch, or an RF facility is used, the jitter could be a negligible effect.

Transverse $\eta(\gamma(x))$

Thomson scattering with a transversely chirped laser pulse is quite robust. The PW bandwidth limit can be retrieved and, moreover, the photon number as an ideal Thomson scattering event. Also it is not sensitive to emittance or an angle of incidence between the bunch and the laser pulse.

The required laser pulse can be obtained by using CPA pulse and a dispersive optical component, e.g. a grating. Implementing this geometry experimentally does require a beamline such that the bunch has its energy correlation perpendicular to the propagation direction.

Prospects

It would be interesting to combine the two geometries together, whereby the laser is described with a pulse front tilt (see for example [156, 157]). An electron bunch obtained from plasma wake acceleration (or RF structure for that matter) can be used directly without the need of additional beamline components as with the $\eta(\gamma(z))$ case. Moreover an electron traverses the entire pulse length and can experience a matched frequency like in the $\eta(\gamma(x))$ case. A front tilted pulse is achieved by using a double set of gratings, like in the pulse compression of a CPA line. The losses for such a compression are substantial, e.g. 30% in [152, 105].

A further study needs to be conducted on two aspects that are intertwined: the maximum reachable bunch charge and quadratic chirp of the laser pulse. Here a 1 [nC] bunch charge was assumed to calculate the total emitted photons. Larger bunch charge can be achieved by increasing its physical size. This however can lead to non-linear energy correlations [158]. Which brings us to the second part: the compensation of non-linear energy correlation requires higher order frequency modulation terms. In

principal such a modulation is compatible with the linear Thomson regime, but could lead to constraints on the geometry similarly as in the study here provided.

4.5 Laser Profile Dependency in the non-linear Thomson regime

It has been shown that the non-linear broadening of the spectrum has a dependency on the shape of the laser pulse [84, 31, 100, 122, 114, 123, 159] as was also introduced in section 2.6.2. To summarise for a plane wave pulse, the longitudinal ponderomotive force is time dependent resulting in a time dependent Dopplershift in the spectrum. Here we will look more closely how the different (longitudinal) pulse shapes affect the spectrum. By having the laser pulse length defined as its Full Width Half Maximum, a meaningful comparison can be made between different pulse shapes, as the pulse energy and intensity are approximately equal, as was discussed in section 2.5.3.

Figure 4.14 shows the on-axis spectra for different intensities. For low intensities ($a_0 \ll 1$) the spectrum equals the Fourier transform of the pulse centred around the Thomson frequency. At $a_0 > 1$ we see the clearest effect of the laser pulse shape: for pulse shapes that have large wings most of the energy is emitted closer to the linear Thomson frequency and that non-linear Thomson peak is different from the flat pulse. To obtain the non-linear peak more accurately, as compared to Eq. 2.62, one should take the zero convexity approximation (see Appendix C.1) for Eq. 2.59. This analytical solution, which is valid where the second derivative of the pulse shape is zero, consists out of an Airy function. For pulse shapes like $\sin^2$, sech and the Gaussian the argument of the Airy function are the same; the only contribution to the spectrum comes from the peak of the pulse, hence we see no difference of the non-linear peak. From this one would expect that the higher harmonics will be equal for these pulses, but this is not what happens because harmonics start to overlap. Now the shape of the spectrum is determined by the interference of the field contributions, similarly as the subsidiary peaks (see section 2.6.2). On the other hand for a super Gaussian envelope we find several stationary points, hence the peak of a harmonic shifts closer to that of the rectangular envelope.

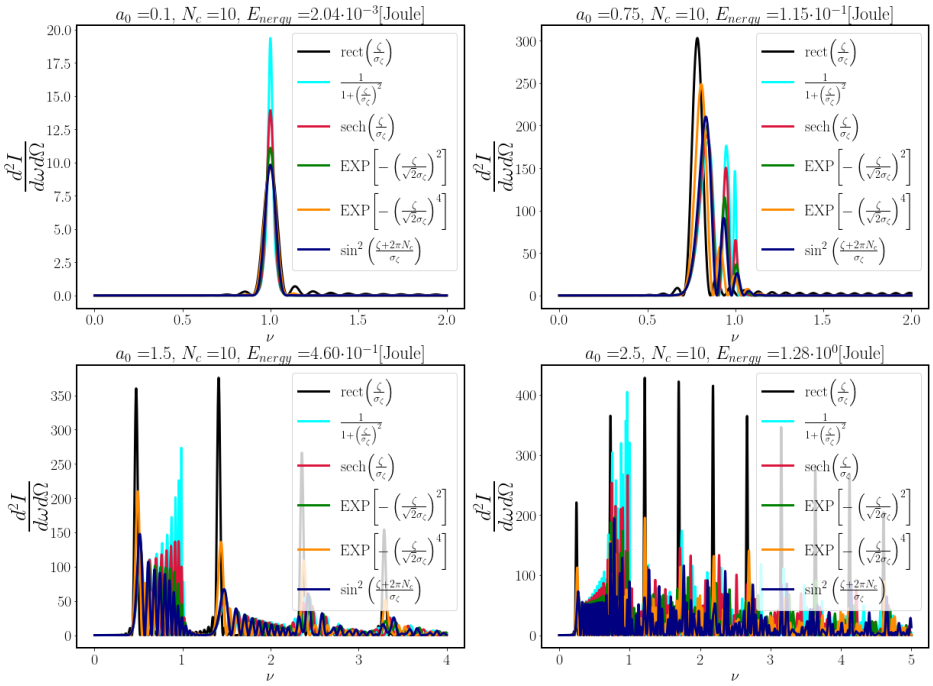

Figure 4.14: Comparison of on-axis Thomson spectra for different pulse shapes. The laser pulse is linearly polarized and the following parameters have been used to calculate the energy: central wavelength $\lambda_l = 1.066\mu$m and $W_0 = 20\mu$m.
Top left: Spectra in the Linear Thomson regime. The shape of the spectra is the same as the Fourier transform of the laser pulse profile, centred around the Thomson frequency.
Top right: The peak of the fundamental starts to shift due to the ponderomotive force. The peak for each pulse shape is slightly different.
Bottom left: Spectra in the non-linear Thomson regime. We see great differences in the fundamental harmonics: the broader wings the laser pulse has the more energy is radiated in the linear Thomson regime. The harmonics are approximately the same, as they reflect the pulse shapes near the centre of the pulse (see Figure 2.4).
Bottom right: In the highly non-linear regime there are two regions where the pulse shape effect remains clear: between the first and the third harmonic and near $\nu = 1$. The higher harmonics overlap, leading to chaotic behaviour and upon averaging will lead to the same contribution independent of the pulse shape.

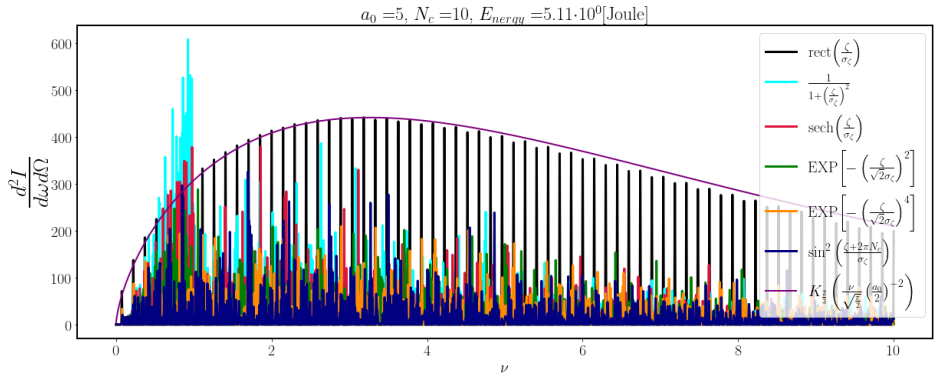

Figure 4.15: Comparison of on-axis Thomson spectra for different pulse shapes for a laser pulse with $a_0 = 5$. The laser pulse is linearly polarized and the following parameters have been used to calculate the energy: central wavelength $\lambda_l = 1.066\mu$m and $W_0 = 20\mu$m. Pulses that have only one maximum emit most of the radiation between $\left(1+\frac{a_0^2}{2}\right)^{-1} \leq \nu \leq 1$ due to the wings of the pulse. The tops of the rectangular pulse follow the modified Bessel function of the second kind (purple) similarly as of a charged particle in instantaneous circular motion [34]. For this pulse shape most of the energy is emitted in the higher harmonics (here around the 20^{th} harmonic).

The dependency of the spectrum regarding the transverse profile is more difficult, because this shape can include a non-negligible transverse ponderomotive force. For the discussion at hand this phenomenon is omitted. Electrons in a bunch will experience different laser field amplitudes due to the transverse profile ($a0\Psi * \vec{r}$). From Eq. 2.62 the difference of the peak of the fundamental frequency depending on the transverse profile is given by

$$\Delta\nu_{\mathscr{E}=1,\Psi} = \nu\left(\mathscr{E}=1,\Psi(x,y,z=0)\right) - \nu\left(\mathscr{E}=1,\Psi=1\right) = \frac{\frac{a_0^2}{2}}{1+\frac{a_0^2}{2}}\frac{1-\Psi^2(x,y)}{1+\frac{a_0^2}{2}\Psi^2(x,y)} \tag{4.30}$$

for a linearly polarised laser pulse. For a circularly polarised laser pulse the intensity term needs to be replaced by $\frac{a_0^2}{2} \rightarrow a_0^2$. This relation is visualized in Figure 4.16. The interesting note is that this broadening of the spectrum has it's largest effect at the start of the non-linearity ($a_0 \sim 1$). This is because here only the electrons most closely to the propagation axis of the laser undergo the non-linear motion. When a_0 increases the volume where the laser has a non-linear intensity is larger and coincidentally the difference of the non-linear Dopplershift decreases. It must be noted that for high a_0 the Lorentz force is no longer a good approximation (see Figure 2.6, as for large values of γ the recoil becomes substantial especially for the the higher harmonics (multi-photon scattering) [98, 99]). Combining the effects of the longitudinal- and transverse profile one expects that for an electron bunch, with its transverse size comparable to that of the laser pulse, will emit most of the energy close to $\nu = 1$. To reduce "noise" in the spectrum one should use an electron bunch several factors smaller than the laser pulse in the case of a Gaussian profile.

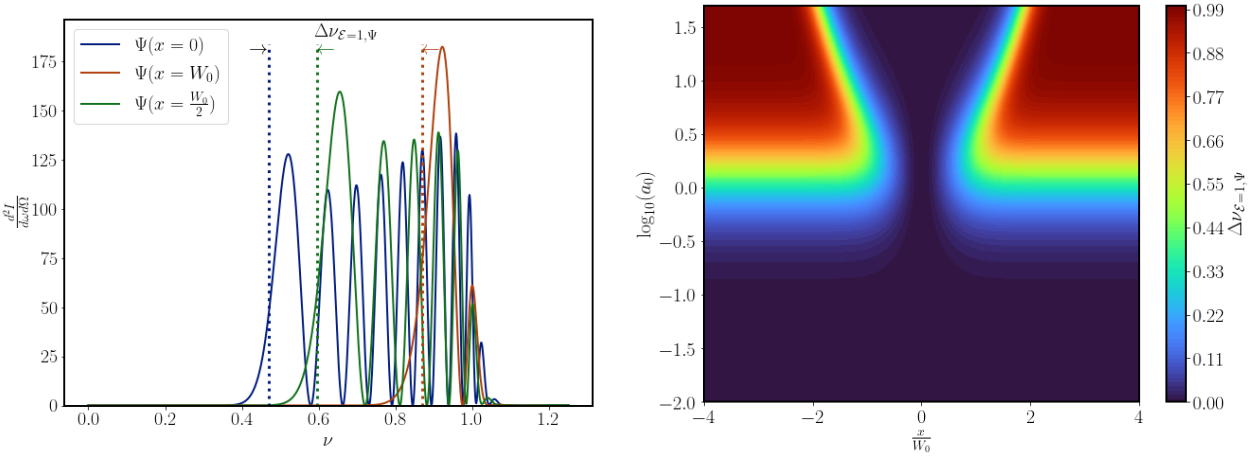

Figure 4.16: Comparison of single electron spectra for different initial transverse positions traversing a laser pulse with a Gaussian transverse- and sech longitudinal profile. Each electron experiences a different amplitude of the laser pulse and therefore the Doppler shift is different. The difference of the peak of the fundamental is given by Eq. 4.30.
Left: Spectrum for a single electron traversing the laser pulse at different transverse positions. The dotted lines indicate the peak of the fundamental.
Right: Contour plot of the difference in the peak of the fundamental harmonic as function of the laser intensity and transverse position of the electron.

4.6 Carrier Envelope Phase

The shape of exact shape of the laser field becomes important for laser pulses that have a length comparable to its wavelength ($\sigma_{t,FWHM} < 10^{-14}$ [s]). For such short pulses the relative phase of the oscillations with respect to the envelope (carrier envelope phase: CEP, η_0, see Figure 4.17) become important for interactions such as electron-nuclear dynamics, metrology, Tomography and Higher Harmonic Generation. For these I refer to the great published works of [142, 10] and references therein. For intensities up to I $\sim 10^{14} - 10^{15}$ $\left[\frac{\mathrm{W}}{\mathrm{cm}^2}\right]$ the CEP can be measured using ionization techniques [160, 161, 162, 163]. For higher intensities this method is no longer viable as the ions will be ionized before the peak intensity has reached the atoms. Instead, Non-linear Thomson scattering could be utilized as a non-destructive diagnostic tool to measure η_0 of the laser pulse in two ways:

- Shift in angular emission [164]
- The interference pattern within the spectrum [165]

These two complementary effects will be investigated in detail first for a single particle and thereafter numerical results are given for the interference pattern with realistic experimental parameters.

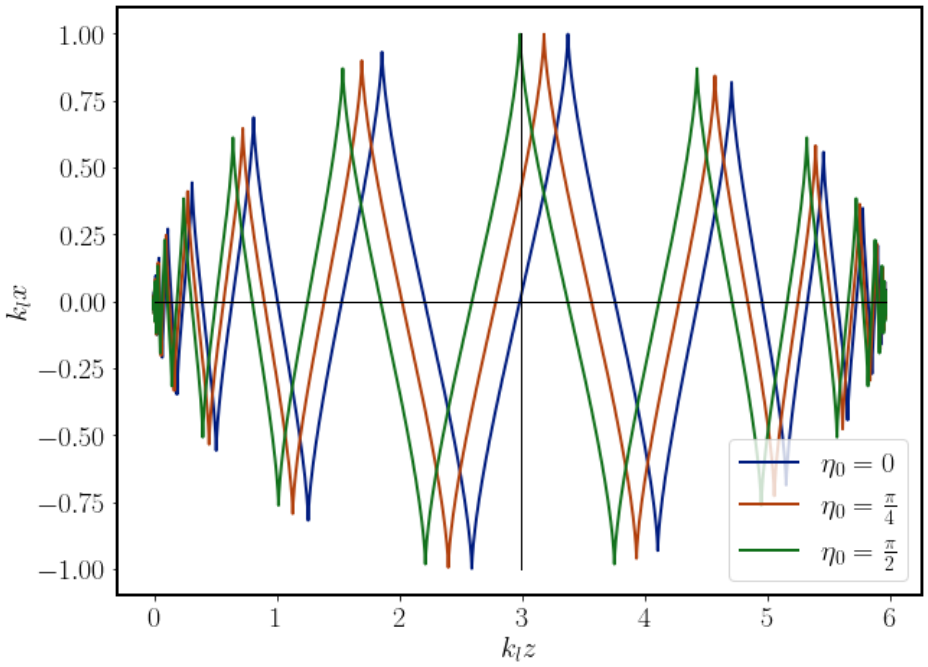

Figure 4.17: Electron trajectory in the non-linear regime ($a_0 > 1$) for different CEP phases (η_0) for a PW laser pulse polarized in $+\hat{x}$. The maxima in the transverse position coincide with the maximum acceleration (as with a harmonic oscillator). An electron will experience maximum acceleration at the centre of the laser pulse for $\eta_0 = \frac{\pi}{2}$. Note that a phase of $\eta_0 = \pi$ is the same as the polarization in $-\hat{x}$.

4.6.1 Single Particle Dynamics

For a quasi-monochromatic linearly polarized laser pulse, in the plane wave approximation, the double differential for back scattered radiation can be written as (see Appendix C)

$$\frac{d^2 I}{d\omega d\Omega} \propto \left| \int_{=\infty}^{\infty} d\zeta a_0 \mathscr{E} \sum_{m=-\infty}^{\infty} (\mathrm{J}_m(B) + \mathrm{J}_{m+1}(B)) \frac{\exp\left[i\eta_0(2m+1)\right]}{2} \exp\left[i \int_{-\infty}^{\zeta} d\zeta'(2m+1) + \nu\left(1 + \frac{a_0^2 \mathscr{E}^2}{2}\right)\right]\right|^2, \tag{4.31}$$

where $B = \nu\left(\frac{a_0\mathscr{E}}{2}\right)^2$ and $\nu = \frac{\omega}{\omega_l}\frac{1}{\gamma^2(1+\beta)^2}$. We can clearly see that there is a dependence on the CEP phase (η_0), but to appreciate how it influences the spectrum we will first interpret Eq. 4.31 quantitatively.

From the stationary phase approximation we know that the frequencies emitted during the interaction are given by

$$\nu_{\mathscr{H}} = -\frac{\mathscr{H}}{1 + \frac{a_0^2 \mathscr{E}^2(\zeta)}{2}}. \tag{4.32}$$

The term $\mathscr{H} = 2m+1$ is the harmonic number and tells us that the backscattered radiation contains odd harmonics. The field dependent term in the denominator is the drift velocity of the electron during the interaction, that gives rise to a Doppler shift in the spectrum (also called non-linear broadening). For low laser intensities the harmonics (if present) are spectrally separated from each other. This means that Eq. 4.31 can be read as the sum of the squares of the harmonics: $|\sum_{\mathscr{H}} f_{\mathscr{H}}|^2 = |f_1|^2 + |f_3| + \ldots$ (see Figure 2.8). In this case η_0 has no influence on the spectrum, and is in fact a global phase factor.

Increasing the laser intensity broadens the spectral composition of a harmonic: the upper bound remains the same ($\nu_{\mathscr{H}}(\zeta = \pm\infty)$) while the lower bound has an increased Doppler shift ($\nu_{\mathscr{H}}(\zeta = 0)$) as was described in Figure 2.7. Therefore there exsists a specific a_0 for when different harmonics start to

overlap and can be calculated using

$$\Delta\nu = 0 = \nu_{\mathscr{H}_i}(\zeta = \pm\infty) - \nu_{\mathscr{H}_j}(\zeta = 0)$$
$$a_{0\Delta\mathscr{H}} = \sqrt{2\frac{\mathscr{H}_j - \mathscr{H}_i}{\mathscr{H}_i}} \tag{4.33}$$

where $\mathscr{H}_i$ is a lower harmonic than $\mathscr{H}_j$. From this relation we find that for the first and the third harmonic to start overlapping the intensity needs to be $a_0 \geq 2$. When the harmonics start to overlap Eq. 4.31 has a solution of the form $|\sum_{\mathscr{H}} f_{\mathscr{H}}|^2 = |f_1|^2 + 2\mathscr{R}_e\left(f_1 f_3^*\right) + |f_3| + \ldots$, where f^* is the complex conjugate. The dependence of η_0 appears within the interfering harmonics. When we look at this cross term of two adjacent harmonics we find that the amplitude at the peak of the higher harmonic depends on the CEP as $\left|\frac{\exp[i\eta_0]}{2}\right|^2$. This change in amplitude at a specific frequency can also be viewed as a shift of the maximum to a different frequency:

$$\nu_{\mathscr{H},\eta_0} \propto \frac{\mathscr{H}}{1+\frac{a_0^2}{2}}\left(1 \pm \frac{\sin^2(\eta_0)}{\sigma_\zeta}\right) \tag{4.34}$$

The results of numerically integrating Eq. 4.31 as function of ν & η_0 are shown in Figure 4.18 ($a_0 = 2$), 4.19 ($a_0 = 3$) and 4.20 ($a_0 = 5$). For $a_0 = 2$ the effect of η_0 is quite clear for the third and fifth harmonic, although the amplitude does not follow smooth transition as the equation above suggests. Looking at $\nu = 2.4$, which actually does not correspond to a harmonic number, shows the signs of a smooth transition. Increasing the laser's amplitude (a_0) shows that for the third and the fifth harmonic the frequency keeps this jump between two values (in Figure 4.19 near $\nu = 0.6$ and in Figure 4.20 near $\nu = 0.2$ and $\nu = 0.4$). For $\nu > 1$ there are many harmonics that overlap and the shift of the peak is a smooth transition as predicted by Eq. 4.34. Note that most of the energy emitted remains close to $\nu = 1$ when the amplitude is increased as described in Section 4.5. The spectral range $\nu < 1$ is chaotic and not suitable for precision measurement of η_0. What we see in all figures is that the η_0 dependency is symmetric around $\eta_0 = \frac{\pi}{2}$. Therefore there is no unique solution for η_0, e.g. $\nu_{\mathscr{H},\eta_0}(\eta_0 = \frac{\pi}{4}) = \nu_{\mathscr{H},\eta_0}(\eta_0 = \frac{3\pi}{4})$. The physical reason behind this is the 2η dependency of the longitudinal oscillation. This combined with the fact that for the on-axis radiation the spectra for $\eta_0 = 0$ and $\eta_0 = \pi$ are equal. To distinguish between the latter two phases one needs to include off-axis radiation.

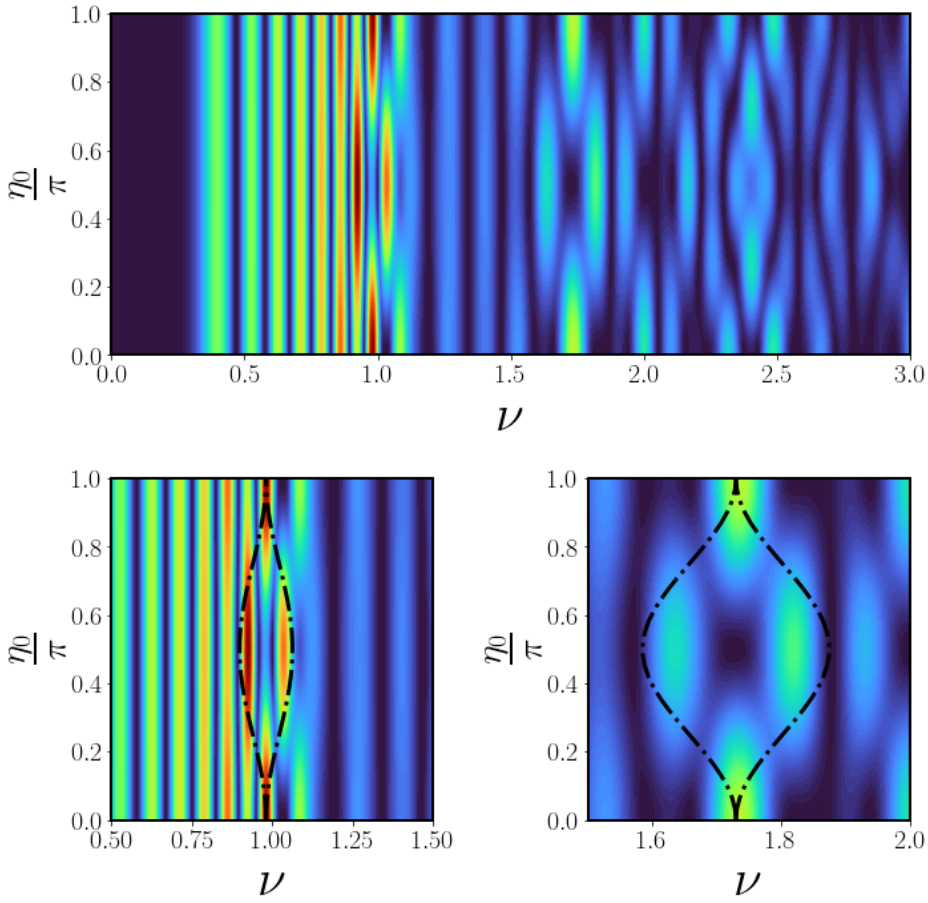

Figure 4.18: Contour plot of on-axis radiation as function of the normalized frequency ν and the CEP phase η_0 for a single electron colliding head-on with a linearly polarized PW laser pulse with an amplitude of $a_0 = 2$.
Top: Complete range of the contour plot.
Bottom left: Cut-out around the 3^{rd} harmonic including the behaviour of the peak according to Eq. 4.34 in black.
Bottom right: Cut-out around the 5^{th} harmonic including the behaviour of the peak according to Eq. 4.34 in black.

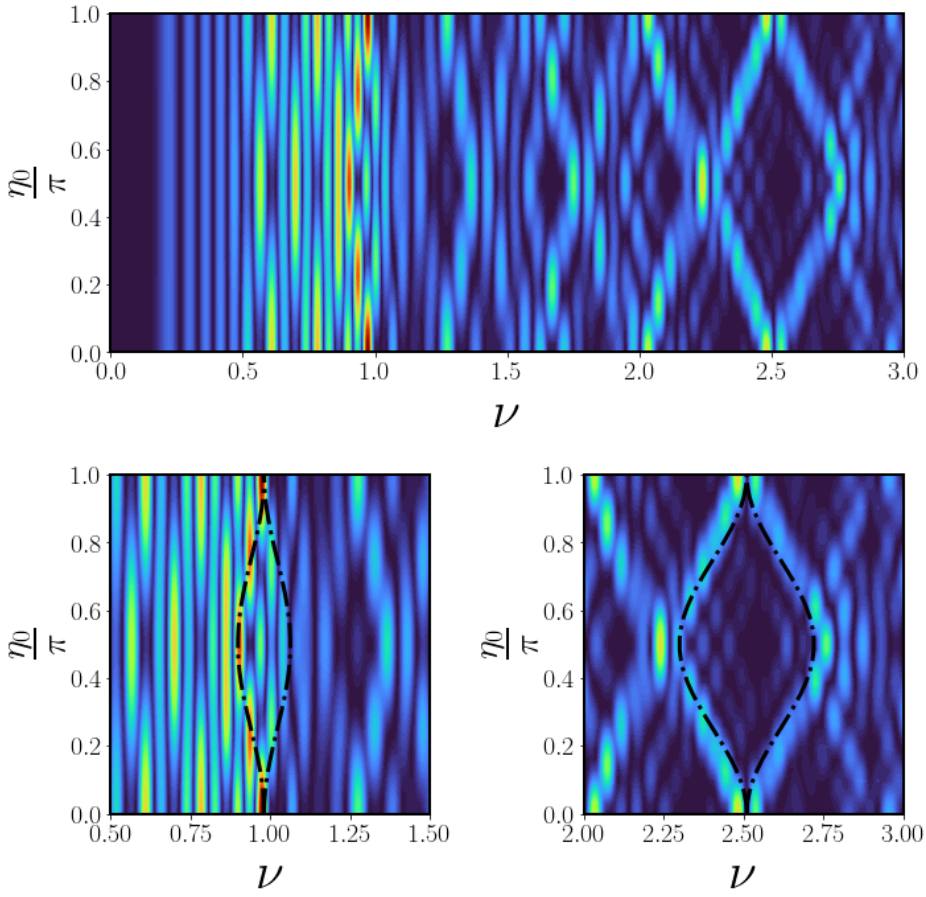

Figure 4.19: Contour plot of on-axis radiation as function of the normalized frequency ν and the CEP phase η_0 for a single electron colliding head-on with a linearly polarized PW laser pulse with an amplitude of $a_0 = 3$. For this and higher intensities many harmonic orders overlap and more of the emitted energy is found in higher harmonics. The CEP dependence is stronger for the higher harmonics, and clearly show a shift of the peak intensity as described by Eq. 4.34.
Top: Complete range of the contour plot.
Bottom left: Cut-out at the 5^{th} harmonic.
Bottom right: Cut-out near the 14^{th} harmonic. Due to the interference between harmonic orders we find that for $\eta_0 = 0$ even harmonics are emitted. For this case the electron has zero acceleration at the peak of the laser pulse. For $\eta_0 = \frac{\pi}{2}$ the electron experiences maximum acceleration at the peak of the laser pulse.

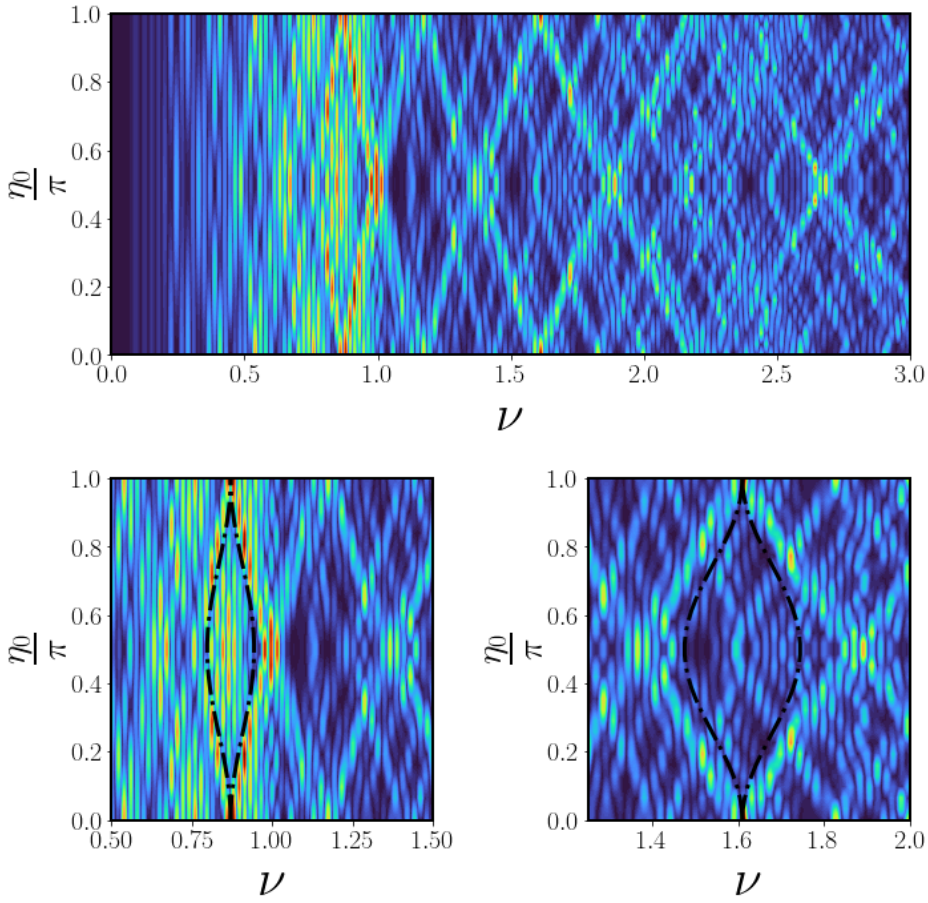

Figure 4.20: Contour plot of on-axis radiation as function of the normalized frequency ν and the CEP phase η_0 for a single electron colliding head-on with a linearly polarized PW laser pulse with an amplitude of $a_0 = 5$. For this and higher intensities many harmonic orders overlap and more of the emitted energy is found in higher harmonics. For such many overlapping harmonics the pattern of the CEP dependence is visible, though many harmonic peaks are shifted and crossing each other. Eq. 4.34 is no longer a good approximation for the shifting maximum.
Top: Complete range of the contour plot.
Bottom left: Cut-out at the 11^{th} harmonic. This harmonic is emitted close to $\nu = 1$ and contains substantial energy of the fundamental harmonic emitted in the wings of the laser pulse (see Figure 2.7).
Bottom right: Cut-out near the 21^{st} harmonic.

From Eq. 2.63 we know that the fundamental harmonic is radiated in a $\frac{1}{\gamma}$ cone. To include the higher harmonics it is better increase the detection cone to $\frac{3}{4\gamma}$. Figures 4.21 and 4.22 were obtained by numerically integrating Eq. 4.31. For $\eta_0 = 0$ we see that the angular spectrum is anti-symmetric around the x axis, whereas for $\eta_0 = \frac{\pi}{2}$ it is symmetric. This is in accordance with the anti-symmetry of the electron's trajectory as shown in Figure 4.17. The subsidiary peaks of a harmonic are emitted in the wings of the laser pulse (see Figure 2.7) and therefore are emitted alternately in the positive and negative x axis. The aforementioned uniqueness of the solution for η_0 can be determined by the off-axis spectra; because $\eta_0 = \pi$ will have a vertically mirrored spectrum of η_0. In [165] it was shown that for a circularly polarized laser pulse the CEP dependence is also visible, but only for off-axis radiation (where harmonics are presented).

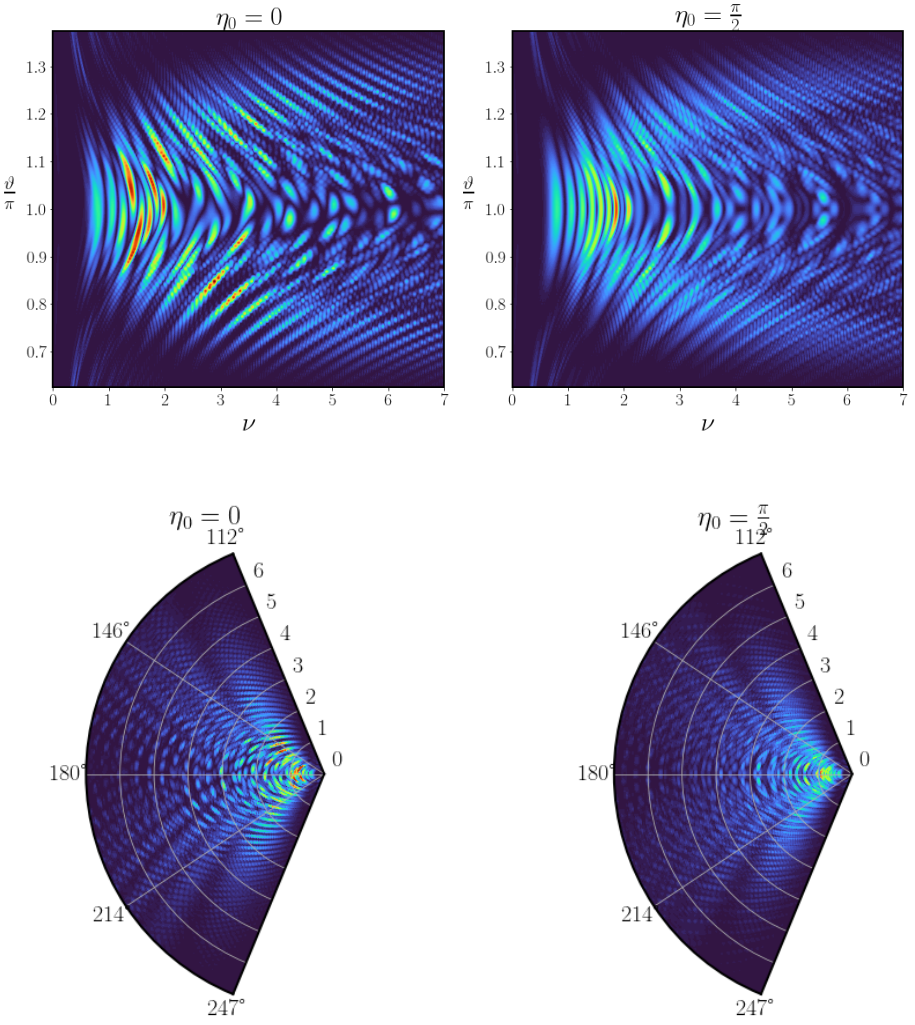

Figure 4.21: Contour plot of emitted radiation as function of the normalized frequency ν and the azimuthal angle ϑ (where $\vartheta = \pi$ is the backscattered direction) for a single electron with $\gamma = 2$ colliding head-on with a linearly polarized PW laser pulse with an amplitude of $a_0 = 2$ and length $N_c = 5$. The azimuthal angle ranges from $\pi(1 - \frac{3}{4\gamma}) \leq \vartheta \leq \pi(1 + \frac{3}{4\gamma})$. The top plots don't change in shape when γ increases, except for the values of the vertical axis. In contrary the bottom plots will be confined in a smaller cone.
Top left: Contour plot where $\eta_0 = 0$. The emitted radiation is anti-symmetric around $\vartheta = \pi$.
Top right: Contour plot where $\eta_0 = \frac{\pi}{2}$. The emitted radiation is symmetric around $\vartheta = \pi$.
Bottom left: Same as Top left, but represented as a polar plot.
Bottom right: Same as Top right but represented as a polar plot.

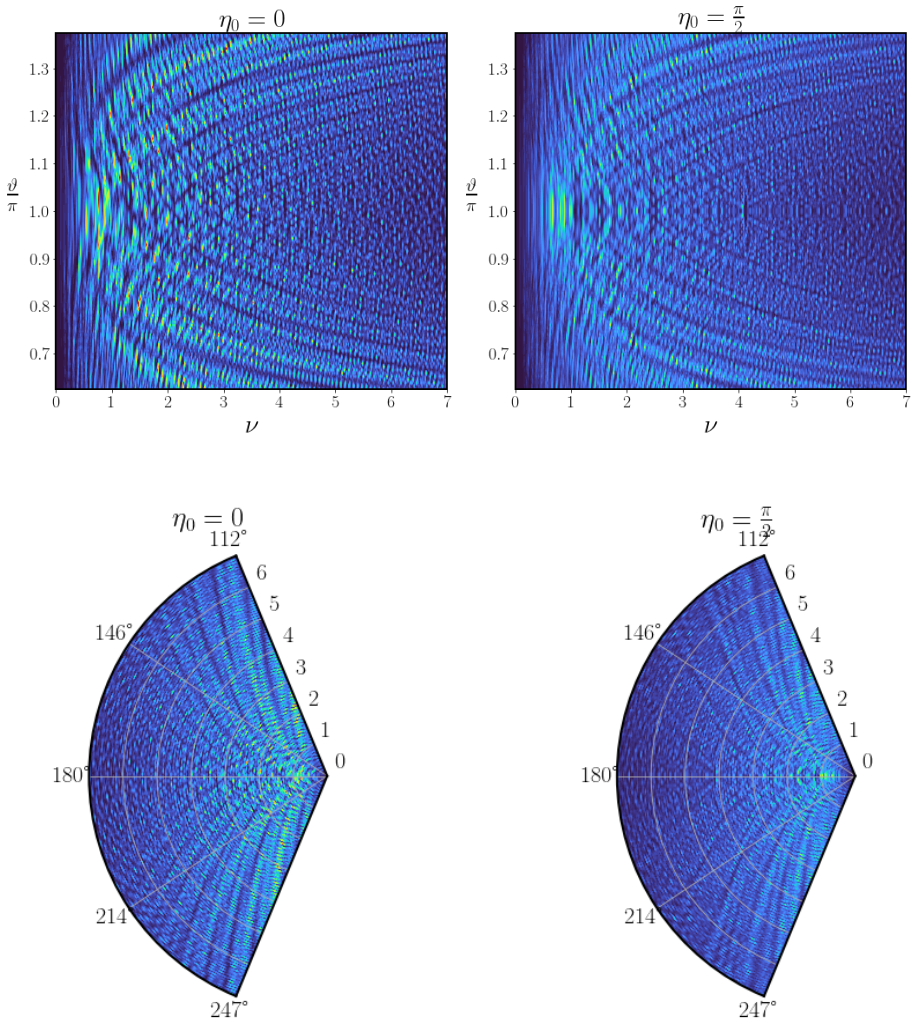

Figure 4.22: Contour plot of emitted radiation as function of the normalized frequency ν and the azimuthal angle ϑ (where $\vartheta = \pi$ is the backscattered direction) for a single electron with $\gamma = 2$ colliding head-on with a linearly polarized PW laser pulse with an amplitude of $a_0 = 5$ and length $N_c = 5$. The azimuthal angle ranges from $\pi(1 - \frac{3}{4\gamma}) \leq \vartheta \leq \pi(1 + \frac{3}{4\gamma})$. The top plots don't change in shape when γ increases, except for the values of the vertical axis. In contrary the bottom plots will be confined in a smaller cone.
Top left: Contour plot where $\eta_0 = 0$. The emitted radiation is anti-symmetric around $\vartheta = \pi$.
Top right: Contour plot where $\eta_0 = \frac{\pi}{2}$. The emitted radiation is symmetric around $\vartheta = \pi$. Comparing
Bottom left: Same as Top left, but represented as a polar plot.
Bottom right: Same as Top right but represented as a polar plot.

4.6.2 Electron beam

In this section the radiated energy within an aperture is calculated (i.e. Eq. 2.24 integrated over the solid angle of the aperture) for Thomson scattering with an electron bunch. Only a fraction of the emission cone is used as an aperture, $\vartheta_{max} = \frac{1}{10\gamma}$, since integration over the angle of Figure 4.21 clearly will washout the CEP dependence. The electron bunch considered here consists out of $N_e = 10^3$ macro particles with an energy spread ($\frac{\sigma}{\gamma} = 10^{-3}$) and emittance ($\epsilon^N{}_x = 10^{-6}$ mm mrad). The average energy of the electrons are chosen on the MeV scale ($2 \leq \gamma \leq 10$). These parameters are easily achievable and require

only a small beamline. First the electron bunch is collided with a plane wave laser pulse with a hyperbolic secant longitudinal profile, to showcase the effect for a realistic bunch and to omit the transverse laser profile dependency (see Section 4.5). Figure 4.23 shows the result for different values of a_0 and γ with dashed vertical lines indicating the position of odd harmonics for $\eta_0 = 0$ and the solid lines for $\eta_0 = \frac{\pi}{2}$ according to Eq. 4.34. The η_0 dependence remains quite clear.

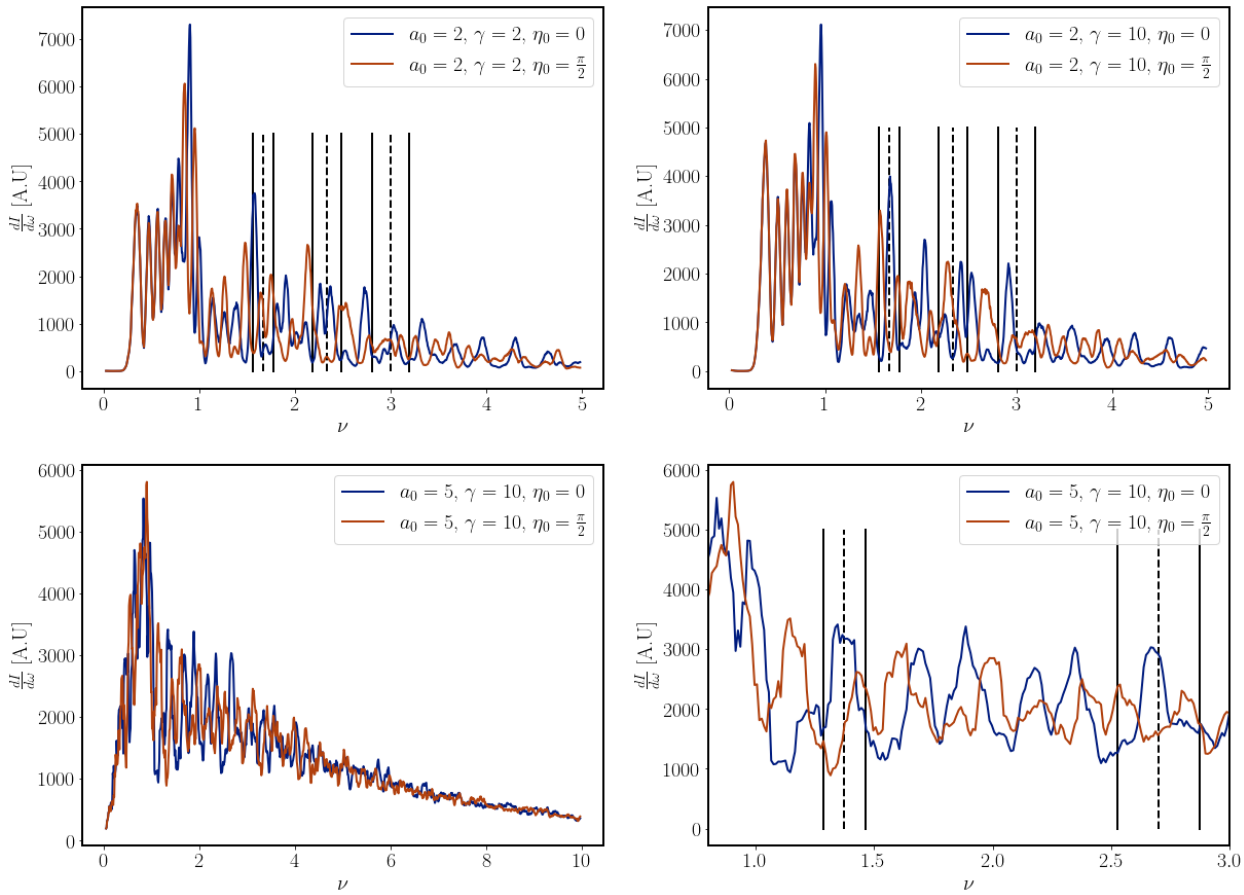

Figure 4.23: CEP dependence in Thomson scattering for a realistic electron bunch colliding with a linearly polarized plane wave laser pulse. The radiation is collected within a cone of $\frac{1}{10\gamma}$. The bunch consists out of $N_e = 10^3$ macro particles with an energy spread ($\frac{\sigma}{\gamma} = 10^{-3}$) and emittance ($\epsilon^N{}_x = 10^{-6}$ mm mrad), and the laser pulse's longitudinal profile is a hyperbolic secant.
Top left: Laser amplitude of $a_0 = 2$ and $\gamma = 2$. The black lines indicate the fifth, seventh and ninth harmonic.
Top right: Same as left, but with $\gamma = 10$. The shift in the harmonic peaks, as compared to the left panel, is due to the reduced ratio in the initial transverse and longitudinal momentum of the electrons.
Bottom left: Laser amplitude of $a_0 = 5$ and $\gamma = 10$. Within the frequency range $0 \leq \nu \leq 1$ the spectrum is chaotic due to the amount of radiation emitted in the wings of the laser pulse, see Section 4.5. For harmonics $\nu > 1$ the CEP dependence is clear.
Bottom right: Cut out of bottom left.

Electrons with a different transverse position experience a different intensity when colliding with a laser pulse with a transverse profile. If one were to use an electron bunch with the same spot size as that of the laser one cannot observe fine details, as is required for η_0. As was shown in Figure 4.16 one expects to see a clean signal for an electron bunch three times smaller than the laser pulse's width. Note that for a fixed emittance and reducing the width equates a stronger focussed beam (i.e. larger divergence). Figure 4.24 shows that the increase in divergence does not influence the spectrum as much as the reduction in width of the electron bunch. A smaller width of $\frac{1}{3}W_0$ does not lead to a cleaner signal.

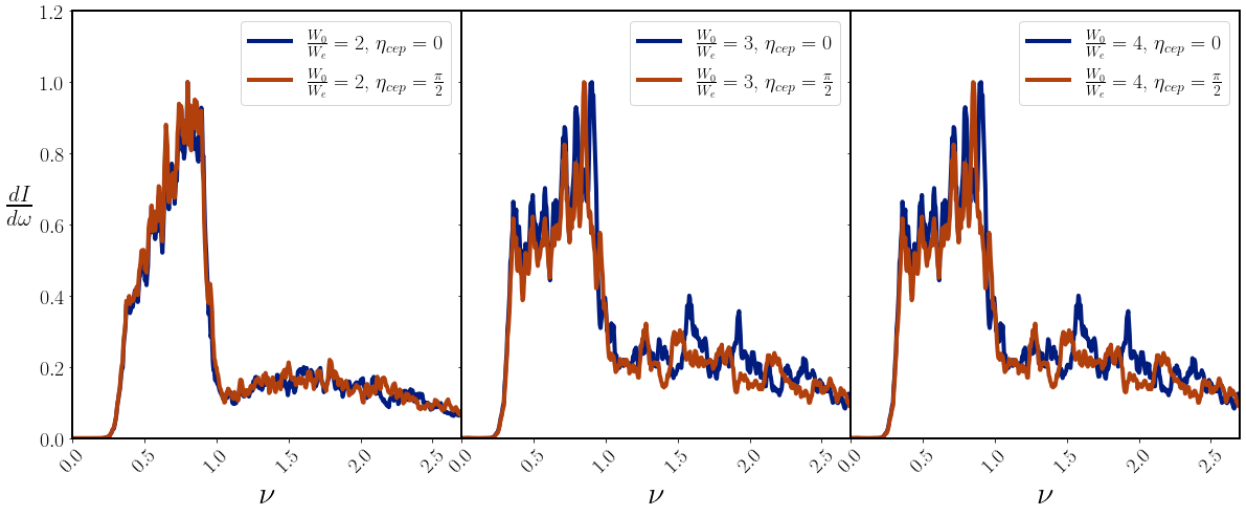

Figure 4.24: Comparison of the radiated energy collected within $\vartheta = \frac{1}{10\gamma}$ between three electron bunches with different transverse size. The laser parameters are $a_0 = 2$, $N_c = 5$, $W_0 = 45\mu$m and electron parameters $\gamma = 2$, $\epsilon^N = 10^{-6}$ mm mrad and $\frac{\sigma_\gamma}{\gamma} = 10^{-3}$. The profile of the laser pulse is given by Eq. 2.36. In order to see the effect of η_{cep} the ratio between the laser- and electron width needs to be small, because of the non-linear broadening depends on the (initial) transverse position of the particle (see Figure 4.16).
Left: For $\frac{W_0}{W_e} = 2$ the non-linear broadening for each electron is so different that the signal of η_{cep} is not visible.
Middle: For $\frac{W_0}{W_e} = 3$ the η_{cep} becomes visible at the higher harmonics. The first harmonic can be used to determine a_0.
Right: Smaller electron bunches does not lead to a cleaner signal.

4.6.3 Discussion

In the previous sections the classical description of non-linear Thomson scattering was used to show and explain the CEP dependency. To fulfil the classical limit the electron recoil needs to be very small including the recoil from multi-photon scattering. For example, to measure near the 100$^{\text{th}}$ harmonic, with a laser pulse with photon energy of 1 eV, the electron energy cannot exceed $\gamma \ll 130$, for the recoil factor to be $\chi \leq 0.01$. In [98, 99] was shown that for $\gamma = 100$ no difference between the classical and quantum description of the on-axis spectrum. Some minor deviations do occur for the harmonics measured at the $\vartheta = \frac{1}{\gamma}$ as was shown in [98] for $\gamma = 80$ up to the fourth harmonic. For the numerical results given in the previous sections the electron energy was $\gamma \leq 10$, reducing the deviation of the classical from the quantum description. Measuring the spectrum with a small aperture close to the axis as in Figure 4.24 further ensures that the classical limit is valid.

Furthermore, the use of these (relatively) low energy electrons have three further positive effects: a small beamline for electrons, the radiation cone is large as it scales with $\frac{3}{4\gamma}$ and the wavelength of the emitted radiation remain in the UV - soft x-ray range. For the latter the optics required for measurement are well established and the detector resolutions are high.

The results given here, were for a pulse length of $N_c = 5$ ($\sigma_t = 9$ fs). It is expected that for shorter pulses η_0 has a larger effect, however the profile described by Eq. 2.36 no longer is a good approximation to Maxwell's equations (see Figure 2.5).

Direct measurement of the angular difference of a harmonic as function of η_0 was first proposed in [164]. One might be tempted to use the off-axis spectrum (as shown in Figure 4.21) from two angles as a form of interferometer to determine η_0. This, however, is not that straightforward as it is a *field* depending phenomenon and the results given here are energy spectra (i.e. no more phase dependent). Adding the fields up at a specific angle, within the absolute brackets of Eq. 4.31, did not give the envisioned

result: for $\eta_0 = \frac{\pi}{2}$ the expectation is that the two fields cancel each other out, but this is not the case. One could of course subtract two energy spectra, obtained by two detectors positioned symmetrically around the backscattered direction, to find the η_0.

Chapter 5

Conclusions & Perspectives

To increase the efficiency of an FEL it is necessary to increase the brightness of a bunch. This can be achieved by compressors, such as chicanes or a double bend achromat. Here the electric and magnetic fields emanating from the electrons inside the bunch can cause unwanted effects. A computational tool has been developed to calculate the retarded time for electrons travelling along circular paths.

For the 1D model the retarded time, as function of the electron's energy, follows an "S" curve and three approximations have been found. One of them is a fitted function, consisting out of hyperbolic geometric functions, and although it does perform the worst I think it indicates to an exact analytical solution, because the critical points of the fit coincide with that of the electric field. From the geometric constraint a relation is given for the asymptotic value of the retarded time.

Using these solutions it was found that the Coulomb field increases in magnitude after a certain energy, and much larger than usually described as the relativistic regime. For example for a particle separation of 1 [μm], radius of curvature $R = 5$[m] the rise in the magnitude of the Coulomb field starts at $\gamma \sim 50$. At this energy the Coulomb and radiation field have the same magnitude, but because they point in opposite directions the total field is lower. The Coulomb field has its largest magnitude when the retarded time curve is at the inflection point. For the associated energy and particle separation a proportionality relation is given. The total electric field has an asymptote as the energy keeps increasing. This is because the Coulomb field becomes negligible. Also for this a proportionality relation is given.

From the 2D model, where the source travels along a circular path but the observation points can be in 3D, it was shown how the retarded time is very asymmetric for large distances away from the source's current position. The largest value for the retarded time is not found along $\vec{\beta}$ of the current position but rather for $\hat{\delta r} \cdot \hat{\beta} = \frac{\sqrt{2}}{2}$. With the 2D solution it was explained why the radiation field is zero before it becomes dominant: there exists a surface around the source's current position for which the term $\hat{n} - \vec{\beta}$ is parallel to the acceleration. This surface becomes narrower and envelopes the source particle more closely as the energy increases. That the Coulomb field and radiation field point in different directions has been shown clearly for the energy proportionality relations mentioned earlier.

Finally, the retarded time has been investigated for a bunch travelling in a dipole. Meaning that it travels along a helical path. The initial results of the algorithm, based on the analytical constraint, are quite good; the error in the retarded time and field are less than 10% for most particle pairs. For particles nearest to each other there is a larger error.

The algorithm needs to be optimized by itself and parallelization of the calculations need to implemented to decrease the simulation time. For example, it takes about 26 second to calculate the electric field on a grid of the 500x500 points for a single source. This is essentially the same as a bunch consisting of 500 macro-particles and calculating the fields for each pair. It will be very interesting to calculate the field effects for the aforementioned energy relations, and to calculate the effects on a practical example.

Most of the current production of synchrotron radiation using laser-electron scattering lie within the linear Thomson regime. The most common method is to use a Fabry-Perot cavity to obtain medium-high intensities of up to $I \sim 10^{14} - 10^{15}$ [W/cm^2]. Higher order transverse modes can be excited because of imperfections of the mirrors or deformations of them caused by heat dissipation. These modes are $n \geq 10$ and can have powers up to 20%. The incoherent summation of the emitted radiation is still a valid

approximation for such laser pulses if its spot size equals that of the electron bunch. The shape of the Thomson spectra for the degenerate modes equal that of the fundamental mode, but with a decreased intensity. Furthermore, different degenerate pulses could not be distinguished.

The general method for Thomson scattering is to collide a (quasi) monochromatic laser pulse with an electron bunch that has a very small energy spread to ensure that the emitted radiation has a narrow bandwidth. It has been investigated in detail if an electron bunch with a large linear energy spread can be compensated by a chirped laser pulse. This could improve the yield of the emitted radiation by increasing the bunch charge, without deterioration of the final spectrum. Laser pulses with the right criteria are readily available and are based on the chirped pulse amplification technique. Two geometries have been investigated: a longitudinal and a transverse chirp. For both cases the bandwidth of the monochromatic case can be retrieved.

The longitudinal configuration requires that the energy gradient to be small compared to the interaction length: $L_I \leq \frac{3}{5}\sigma_z$. Also it requires an angle of incidence between the laser pulse and the electron beam. This poses a problem for self-injected plasma accelerated electron bunches, but not for external injection or RF accelerated bunches. It has been shown that even for a realistic bunch this configuration retrieves the bandwidth of the ideal case, but with lower number of emitted photons.

The transverse configuration requires a dispersive element for both the laser and the electron bunch, but the plus side is that a single electron traverses the entire laser pulse and there are no further constraints. Inspiration for the design of a beamline can be taken from the transverse gradient undulator, and should not pose big issues. For an idealized chirped electron bunch the transverse configuration performs excellent. For a realistic case the energy spread along a transverse position does reduce its performance, similar as with the longitudinal case. In the simulation the laser pulse and electron bunch collide head-on, another study should decide if the angle of incidence for a realistic case has no influence.

What would be interesting is to investigate the two configurations combined: a laser pulse with a tilted wavefront. In such a configuration the energy spread of the electrons are along the propagation direction, and a single electron will travel through the entire pulse. Furthermore, the study here focussed only on a linear energy correlation of the electron bunch. In principle nothing prevents the compensation of a quadratic, or higher order, correlation. A further study is required in order to confirm this.

Within the non-linear Thomson regime two studies have been performed; the non-linear broadening from the laser pulse shape and the carrier phase envelope. To compare the different pulse shapes the FWHM temporal length has been used so that all profiles have the same energy, duration and intensity. For a rectangular temporal profile the on-axis radiation is identical to that of an electron traversing a dipole magnet. For other pulse shapes most of the on-axis radiation is emitted in the normalized frequency range $0 \leq \nu \leq 1$. The non-linear broadening due to a Gaussian transverse profile has been investigated and shown that it is maximal for $a_0 \sim 1$. In order to omit this broadening effect the width of an electron bunch should be $\sigma_x \leq \frac{W_0}{3}$. For $a_0 \geq 10$ the broadening effect is greatly diminished within W_0, as the non-linear broadening can be approximated with $\frac{1}{a_0^2}$ independent of the transverse position of the electrons.

For ultra-short pulses, the length comparable to or smaller than its wavelength, the carrier envelope phase determines the exact shape of the electromagnetic wave. Here it is shown that Thomson scattering can be used to measure this phase in the non-linear regime (I$> 10^{18}$ [W/cm^2], $a_0 > 1$). For these high intensities the different harmonic orders overlap in the spectrum and carrier envelope phase changes the positions of the harmonic peaks. By using low energy electrons of several MeV the classical description is still a good approximation. Coincidentally the wavelength of the emitted radiation is in the UV-soft x-ray range wherefore optics and detectors are well established.

Bibliography

[1] L et al. Serafini. "MariX, an advanced MHz-class repetition rate X-ray source for linear regime time-resolved spectroscopy and photon scattering". In: *Nuclear Instruments and Methods in Physics Research Section A: Accelerators, Spectrometers, Detectors and Associated Equipment* 930 (2019), pp. 167–172. URL: marix.eu.

[2] B. Piccirillo et al. "Geometric Phase-Enhanced Platform for Polarization and Wavefront analysis techniques with the short-TeraHertz FEL Oscillator TerRa BriXSinO". In: *unpublished* ().

[3] C. Koral et al. "Multi-pass Free-Electron Laser-assisted spectral and imaging applications in the THz/FIR range using the future superconducting electron source BriXinO". In: *Frontiers in Physics, section Radiation Detectors and Imaging* (accepted).

[4] Yun-Shik Lee. *Principles of terahertz science and technology*. Vol. 170. Springer Science and Business Media, 2009.

[5] B Zhu et al. "Terahertz science and technology and applications". In: *PIERS Proceedings*. 2009, pp. 1166–1170.

[6] W Cong and G Wang. "X-ray scattering tomography for biological applications". In: *Journal of X-ray Science and Technology* 19.2 (2011), pp. 219–227.

[7] B et al. Gunther. "The versatile X-ray beamline of the Munich Compact Light Source: design, instrumentation and applications". In: *Journal of Synchrotron Radiation* 27.5 (2020), pp. 1395–1414.

[8] Brian J Quiter et al. "Nuclear resonance fluorescence for materials assay". In: *IEEE Transactions on Nuclear Science* 58.2 (2011), pp. 400–403.

[9] Brian J Quiter et al. "Transmission nuclear resonance fluorescence measurements of 238U in thick targets". In: *Nuclear Instruments and Methods in Physics Research Section B: Beam Interactions with Materials and Atoms* 269.10 (2011), pp. 1130–1139.

[10] Ferenc Krausz and Misha Ivanov. "Attosecond physics". In: *Rev. Mod. Phys.* 81 (1 2009), pp. 163–234. DOI: 10.1103/RevModPhys.81.163.

[11] Calvin R Howell et al. "International workshop on next generation gamma-ray source". In: *Journal of Physics G: Nuclear and Particle Physics* 49.1 (2021), p. 010502.

[12] Yoshihide Nakamiya and Kensuke Homma. "Probing vacuum birefringence under a high-intensity laser field with gamma-ray polarimetry at the GeV scale". In: *Physical Review D* 96.5 (2017), p. 053002.

[13] G.A. Schott B.A. B.Sc. "XI. On the electron theory of matter and on radiation". In: *The London, Edinburgh, and Dublin Philosophical Magazine and Journal of Science* 13.74 (1907), pp. 189–213. DOI: 10.1080/14786440709463594.

[14] Herbert C. Pollock. "The discovery of synchrotron radiation". In: *American Journal of Physics* 51.3 (1983), pp. 278–280. DOI: 10.1119/1.13289.

[15] Gavin Connor Fox. "Generation X-ray–A Coming of Age". In: *ARBOR Ciencia, Pensamiento y Cultura* 191.772 (2015), a221.

[16] G Margaritondo. "Synchrotron light: A success story over six decades". In: *La Rivista del Nuovo Cimento* 40.9 (2017), pp. 411–471.

[17] G. N. KULIPANOV and A. N. SKRINSKY. “I. YA. POMERANCHUK AND SYNCHROTRON RADIATION”. In: *I Ya Pomeranchuk and Physics at the Turn of the Century*, pp. 72–87. DOI: 10.1142/9789812702883_0006.

[18] John P Blewett. “Radiation losses in the induction electron accelerator”. In: *Physical Review* 69.3-4 (1946), p. 87.

[19] Julian Schwinger. “On the classical radiation of accelerated electrons”. In: *Physical review* 75.12 (1949), p. 1912.

[20] Gennadii N Kulipanov. “ORAL ISSUE OF THE JOURNAL USPEKHI FIZICHESKIKH NAUK: Ginzburg’s invention of undulators and their role in modern synchrotron radiation sources and free electron lasers”. In: *Physics Uspekhi* 50.4 (2007), pp. 368–376.

[21] John Madey, Marlan O Scully, and Phillip Sprangle. “The free electron laser: conceptual history”. In: *Physica Scripta* 91.8 (2016), p. 083003. DOI: 10.1088/0031-8949/91/8/083003.

[22] Saldin Derbenev Rossbach. *Microbunch Radiative Tail-Head interaction*. 1995. (Visited on 12/03/2021).

[23] E.L. Saldin, E.A. Schneidmiller, and M.V. Yurkov. “On the coherent radiation of an electron bunch moving in an arc of a circle”. In: *Nuclear Instruments and Methods in Physics Research Section A: Accelerators, Spectrometers, Detectors and Associated Equipment* 398.2 (1997), pp. 373–394. ISSN: 0168-9002. DOI: 10.1016/S0168-9002(97)00822-X.

[24] Prof. J.J. Thomson M.A. F.R.S. “LXX. On the number of corpuscles in an atom”. In: *The London, Edinburgh, and Dublin Philosophical Magazine and Journal of Science* 11.66 (1906), pp. 769–781. DOI: 10.1080/14786440609463496.

[25] Chris Harvey, Thomas Heinzl, and Anton Ilderton. “Signatures of high-intensity Compton scattering”. In: *Phys. Rev. A* 79 (6 2009), p. 063407. DOI: 10.1103/PhysRevA.79.063407.

[26] JH Hubbell. “Summary of existing information on the incoherent scattering of photons, particularly on the validity of the use of the incoherent scattering function”. In: *Radiation Physics and Chemistry* 50.1 (1997), pp. 113–124.

[27] AI Nikishov and VI Ritus. “Quantum processes in the field of a plane electromagnetic wave and in a constant field. I”. In: *Sov. Phys. JETP* 19.2 (1964), pp. 529–541.

[28] Marc J. Feldman and Raymond Y. Chiao. “Single-Cycle Electron Acceleration in Focused Laser Fields”. In: *Phys. Rev. A* 4 (1 1971), pp. 352–358. DOI: 10.1103/PhysRevA.4.352.

[29] F. V. et al. Hartemann. “Three-dimensional relativistic electron scattering in an ultrahigh-intensity laser focus”. In: *Phys. Rev. E* 58 (4 1998), pp. 5001–5012. DOI: 10.1103/PhysRevE.58.5001.

[30] James J Condon and Scott M Ransom. *Essential radio astronomy*. Princeton University Press, 2016.

[31] F. Mackenroth and A. Di Piazza. “Nonlinear Compton scattering in ultrashort laser pulses”. In: *Phys. Rev. A* 83 (3 2011), p. 032106. DOI: 10.1103/PhysRevA.83.032106.

[32] D Seipt and B Kampfer. “Nonlinear Compton scattering of ultrahigh-intensity laser pulses”. In: *Laser Physics* 23.7 (2013), p. 075301. DOI: 10.1088/1054-660x/23/7/075301.

[33] George R Blumenthal and Robert J Gould. “Bremsstrahlung, synchrotron radiation, and compton scattering of high-energy electrons traversing dilute gases”. In: *Reviews of Modern Physics* 42.2 (1970), p. 237.

[34] John David Jackson. *Classical Electrodynamics*. 3rd. New York: John Wiley and Sons Inc., 1999, pp. xxii+808. ISBN: 0-471-30932-X.

[35] John Robinson Pierce. “Traveling-wave tubes”. In: *The bell System technical journal* 29.2 (1950), pp. 189–250.

[36] Claudio Pellegrini and S Reiche. “The development of X-ray free-electron lasers”. In: *IEEE Journal of Selected Topics in Quantum Electronics* 10.6 (2004), pp. 1393–1404.

[37] R Bonifacio et al. “Physics of the high-gain FEL and superradiance”. In: *La Rivista del Nuovo Cimento (1978-1999)* 13.9 (1990), pp. 1–69.

[38] G Fiocco and E Thompson. “Thomson scattering of optical radiation from an electron beam”. In: *Physical Review Letters* 10.3 (1963), p. 89.

[39] Richard H Milburn. “Electron scattering by an intense polarized photon field”. In: *Physical Review Letters* 10.3 (1963), p. 75.

[40] L Federici et al. “Backward Compton scattering of laser light against high-energy electrons: the LADON photon beam at Frascati”. In: *Il Nuovo Cimento B (1971-1996)* 59.2 (1980), pp. 247–256.

[41] W Decking et al. “A MHz-repetition-rate hard X-ray free-electron laser driven by a superconducting linear accelerator”. In: *Nature photonics* 14.6 (2020), pp. 391–397.

[42] Henrik Loos et al. “LCLS beam diagnostics”. In: *Proc. IBIC’14* (2014).

[43] V Schlott et al. “Overview and status of SwissFEL diagnostics”. In: *Proc. IBIC’15* (2016), pp. 12–16.

[44] H Tanaka et al. “Status Report on the Commissioning of the Japanese XFEL at SPring-8”. In: *Laser* 20 (2011), p. 30.

[45] Wolfgang Weingarten. “Superconducting cavities: basics”. In: (1996).

[46] A Bacci et al. “Two-pass two-way acceleration in a superconducting continuous wave linac to drive low jitter x-ray free electron lasers”. In: *Physical Review Accelerators and Beams* 22.11 (2019), p. 111304.

[47] Helmut Wiedemann. “Introduction to Accelerator Physics”. In: *Particle Accelerator Physics*. Cham: Springer International Publishing, 2015, pp. 3–41. ISBN: 978-3-319-18317-6. DOI: 10.1007/978-3-319-18317-6_1.

[48] M Borland. “ELEGANT: A flexible SDDS-compliant code for accelerator simulation”. In: (2000). DOI: 10.2172/761286.

[49] M. Rossetti Conti. “BEAM DYNAMICS FOR EXTREME ELECTRON BEAMS”. English. PhD thesis. Physics, 2019. DOI: 10.6100/IR571240.

[50] S.B. Geer van der et al. *3D Space-charge model for GPT simulations of high-brightness electron bunches*. English. TESLA report. DESY, 2003.

[51] Toshiki Tajima and John M Dawson. “Laser electron accelerator”. In: *Physical Review Letters* 43.4 (1979), p. 267.

[52] CE Clayton et al. “Relativistic plasma-wave excitation by collinear optical mixing”. In: *Physical review letters* 54.21 (1985), p. 2343.

[53] WP Leemans et al. “Multi-GeV electron beams from capillary-discharge-guided subpetawatt laser pulses in the self-trapping regime”. In: *Physical review letters* 113.24 (2014), p. 245002.

[54] MC Downer et al. “Diagnostics for plasma-based electron accelerators”. In: *Reviews of Modern Physics* 90.3 (2018), p. 035002.

[55] S Arjmand et al. “Characterization of plasma sources for plasma-based accelerators”. In: *Journal of Instrumentation* 15.09 (2020), p. C09055.

[56] CGR Geddes et al. “High-quality electron beams from a laser wakefield accelerator using plasma-channel guiding”. In: *Nature* 431.7008 (2004), pp. 538–541.

[57] R. et al. Weingartner. “Ultralow emittance electron beams from a laser-wakefield accelerator”. In: *Phys. Rev. ST Accel. Beams* 15 (11 2012), p. 111302. DOI: 10.1103/PhysRevSTAB.15.111302.

[58] Lianghong Yu et al. “Optimization for high-energy and high-efficiency broadband optical parametric chirped-pulse amplification in LBO near 800nm”. In: *Opt. Lett.* 40.14 (2015), pp. 3412–3415. DOI: 10.1364/OL.40.003412.

[59] E. vystun et al. “Beam quality preservation studies in a laser-plasma accelerator with external injection for EuPRAXIA”. In: *Nuclear Instruments and Methods in Physics Research A* 909 (2018), pp. 90–94. DOI: 10.1016/j.nima.2018.02.060.

[60] S M Hooker et al. “Multi-pulse laser wakefield acceleration: a new route to efficient, high-repetition-rate plasma accelerators and high flux radiation sources”. In: *Journal of Physics B: Atomic, Molecular and Optical Physics* 47.23 (2014), p. 234003. DOI: 10.1088/0953-4075/47/23/234003.

[61] R. et al. D’Arcy. “FLASHForward: plasma wakefield accelerator science for high-average-power applications”. In: *Philosophical Transactions of the Royal Society A: Mathematical, Physical and Engineering Sciences* 377.2151 (2019), p. 20180392. DOI: 10.1098/rsta.2018.0392.

[62] S. et al. Corde. “High-field plasma acceleration in a high-ionization-potential gas”. In: *Nature Communications* 7 (June 2016). DOI: 10.1038/ncomms11898.

[63] Riccardo Pompili et al. “Energy spread minimization in a beam-driven plasma wakefield accelerator”. In: *Nature Physics* (2020), pp. 1–5.

[64] et al. Taek Kim. “Stable multi-GeV electron accelerator driven by waveform-controlled PW laser pulses”. In: *Scientific Reports* 7.1 (2017). DOI: 10.1038/s41598-017-09267-1.

[65] et al. Gonsalves. “Petawatt Laser Guiding and Electron Beam Acceleration to 8 GeV in a Laser-Heated Capillary Discharge Waveguide”. In: *Phys. Rev. Lett.* 122 (8 2019), p. 084801. DOI: 10.1103/PhysRevLett.122.084801.

[66] Altan Cakir and Oguz Guzel. *A Brief Review of Plasma Wakefield Acceleration*. 2020. arXiv: 1908.07207 [physics.acc-ph].

[67] B. Hidding et al. “Directions in plasma wakefield acceleration”. In: *Philosophical Transactions of the Royal Society A: Mathematical, Physical and Engineering Sciences* 377.2151 (2019), p. 20190215. DOI: 10.1098/rsta.2019.0215.

[68] A. Pukhov and I. Kostyukov. “Control of laser-wakefield acceleration by the plasma-density profile”. In: *Phys. Rev. E* 77 (2 2008), p. 025401. DOI: 10.1103/PhysRevE.77.025401.

[69] R. et al. Pompili. “Energy spread minimization in a beam-driven plasma wakefield accelerator”. In: *Nature Physics* 17.4 (2021), 499–503. ISSN: 1745-2481. DOI: 10.1038/s41567-020-01116-9.

[70] P Tomassini et al. “High-quality 5 GeV electron bunches with resonant multi-pulse ionization injection”. In: *Plasma Physics and Controlled Fusion* 62.1 (2019), p. 014010. DOI: 10.1088/1361-6587/ab45c5.

[71] Alexander Debus et al. “Circumventing the Dephasing and Depletion Limits of Laser-Wakefield Acceleration”. In: *Phys. Rev. X* 9 (3 2019), p. 031044. DOI: 10.1103/PhysRevX.9.031044.

[72] B. Hidding et al. “Monoenergetic Energy Doubling in a Hybrid Laser-Plasma Wakefield Accelerator”. In: *Phys. Rev. Lett.* 104 (19 2010), p. 195002. DOI: 10.1103/PhysRevLett.104.195002.

[73] G. Bassi et al. “Overview of CSR codes”. In: *Nuclear Instruments and Methods in Physics Research Section A: Accelerators, Spectrometers, Detectors and Associated Equipment* 557.1 (2006). Energy Recovering Linacs 2005, pp. 189–204. ISSN: 0168-9002. DOI: 10.1016/j.nima.2005.10.067.

[74] Z. Tibai et al. “Proposal for Carrier-Envelope-Phase Stable Single-Cycle Attosecond Pulse Generation in the Extreme-Ultraviolet Range”. In: *Phys. Rev. Lett.* 113 (10 2014), p. 104801. DOI: 10.1103/PhysRevLett.113.104801.

[75] V. Petrillo et al. "Optical beam with vortices: A first order paraxial analysis". In: *Nuclear Instruments and Methods in Physics Research Section A: Accelerators, Spectrometers, Detectors and Associated Equipment* 865 (2017). Physics and Applications of High Brightness Beams 2016, pp. 13–19. ISSN: 0168-9002. DOI: 10.1016/j.nima.2016.08.051.

[76] R. L. Jaffe. *MIT Quantum Theory Notes Supplementary Notes for MIT's Quantum Theory Sequence*. 2007.

[77] J. Napolitano. *SI and CGS Units in Electromagnetism*. 2017.

[78] R. G. Littlejohn. *Gaussian, SI and Other Systems of Units in Electromagnetic Theory*. 2020.

[79] H.G.B. Casimir. "On electromagnetic units". In: 41 (1968), pp. 6–7.

[80] F. Rohrlich. "The self-force and radiation reaction". In: *American Journal of Physics* 68.12 (2000), pp. 1109–1112. DOI: 10.1119/1.1286430.

[81] L. D. Landau and E. M. Lifshitz. *The Classical Theory of Fields*. Oxford: Pergamon Press, 1962, pp. ix+404.

[82] N. V. Elkina et al. "Improving the accuracy of simulation of radiation-reaction effects with implicit Runge-Kutta-Nystrom methods". In: *Phys. Rev. E* 89 (5 2014), p. 053315. DOI: 10.1103/PhysRevE.89.053315.

[83] Y. Hadad et al. "Effects of radiation reaction in relativistic laser acceleration". In: *Phys. Rev. D* 82 (9 2010), p. 096012. DOI: 10.1103/PhysRevD.82.096012.

[84] A. Di Piazza. *Exact solution of the Landau-Lifshitz equation in a plane wave*. 2008. arXiv: 0801.1751 [physics.optics].

[85] M Ruijter, V Yu Kharin, and S G Rykovanov. "Analytical solutions for nonlinear Thomson scattering including radiation reaction". In: *Journal of Physics B: Atomic, Molecular and Optical Physics* 51.22 (2018), p. 225701. DOI: 10.1088/1361-6455/aae6e9.

[86] E.D. Courant and H.S. Snyder. "Theory of the Alternating-Gradient Synchrotron". In: *Annals of Physics* 281.1 (2000), pp. 360–408. ISSN: 0003-4916. DOI: 10.1006/aphy.2000.6012.

[87] G. K. O'Neill and E. J. Woods. "Intersecting-Beam Systems with Storage Rings". In: *Phys. Rev.* 115 (3 1959), pp. 659–668. DOI: 10.1103/PhysRev.115.659.

[88] J. Buon. "Beam phase space and emittance". In: *Cas,Cern Accelerator School 5 General Accelerator Physics Course*. Jyvaeskylae, Finland. URL: http://hal.in2p3.fr/in2p3-00020876.

[89] F.B. Kiewiet. "Generation of ultra-short, high brightness relativistic electron bunches". English. PhD thesis. Applied Physics, 2003. ISBN: 90-386-1815-8. DOI: 10.6100/IR571240.

[90] *Space Charge Mitigation*. 2018. DOI: 10.23730/CYRSP-2018-005.89.

[91] C. P. Hauri et al. "Intrinsic Emittance Reduction of an Electron Beam from Metal Photocathodes". In: *Phys. Rev. Lett.* 104 (23 2010), p. 234802. DOI: 10.1103/PhysRevLett.104.234802.

[92] John S. Nodvick and David S. Saxon. "Suppression of Coherent Radiation by Electrons in a Synchrotron". In: *Phys. Rev.* 96 (1 1954), pp. 180–184. DOI: 10.1103/PhysRev.96.180.

[93] Carol J. Hirschmugl, Michael Sagurton, and Gwyn P. Williams. "Multiparticle coherence calculations for synchrotron-radiation emission". In: *Phys. Rev. A* 44 (2 1991), pp. 1316–1320. DOI: 10.1103/PhysRevA.44.1316.

[94] Alexander Blinne et al. "A systematic approach to numerical dispersion in Maxwell solvers". In: *Computer Physics Communications* 224 (2018), pp. 273–281. ISSN: 0010-4655. DOI: 10.1016/j.cpc.2017.10.010.

[95] Kirk T. Mcdonald. *Second-Order Paraxial Gaussian Beam*. 2016.

[96] A E Siegmann. *Lasers*. 1986. ISBN: ISBN-13: 978-0935702118.

[97] "Fourier Optics". In: *Fundamentals of Photonics*. John Wiley and Sons, Ltd, 1991. Chap. 4, pp. 108–156. ISBN: 9780471213741. DOI: doi.org/10.1002/0471213748.ch4.

[98] D. Seipt and B. Kampfer. "Nonlinear Compton scattering of ultrashort intense laser pulses". In: *Phys. Rev. A* 83 (2 2011), p. 022101. DOI: 10.1103/PhysRevA.83.022101.

[99] B. Terzić et al. "Laser chirping in inverse Compton sources at high electron beam energies and high laser intensities". In: *Phys. Rev. Accel. Beams* 24 (9 2021), p. 094401. DOI: 10.1103/PhysRevAccelBeams.24.094401.

[100] V. Petrillo et al. "Phase space distribution of an electron beam emerging from Compton/Thomson back-scattering by an intense laser pulse". In: *EPL (Europhysics Letters)* 101.1 (2013), p. 10008. DOI: 10.1209/0295-5075/101/10008.

[101] KA et al. Tanaka. "Current status and highlights of the ELI-NP research program". In: *Matter and Radiation at Extremes* 5.2 (2020), p. 024402.

[102] Alexander Fedotov. "Conjecture of perturbative QED breakdown". In: *Journal of Physics: Conference Series* 826 (2017), p. 012027. DOI: 10.1088/1742-6596/826/1/012027.

[103] A. et al. Jochmann. "High Resolution Energy-Angle Correlation Measurement of Hard X Rays from Laser-Thomson Backscattering". In: *Phys. Rev. Lett.* 111 (11 2013), p. 114803. DOI: 10.1103/PhysRevLett.111.114803.

[104] KIM TA PHUOC et al. "All-optical Compton gamma-ray source". In: *Nature Photonics* 6 (2012), pp. 308–311. DOI: 10.1038/nphoton.2012.82.

[105] Igor V. Pogorelsky et al. "BESTIA – The next generation ultra-fast CO2 laser for advanced accelerator research". In: *Nuclear Instruments and Methods in Physics Research Section A: Accelerators, Spectrometers, Detectors and Associated Equipment* 829 (2016). 2nd European Advanced Accelerator Concepts Workshop - EAAC 2015, pp. 432–437. ISSN: 0168-9002. DOI: 10.1016/j.nima.2015.11.126.

[106] R. W. Schoenlein et al. "Femtosecond X-ray Pulses at 0.4 angstrom Generated by 90degree Thomson Scattering: A Tool for Probing the Structural Dynamics of Materials". In: *Science* 274.5285 (1996), pp. 236–238. DOI: 10.1126/science.274.5285.236.

[107] C. et al. Vaccarezza. "The SPARC-LAB Thomson source commissioning". In: *IPAC 2014: Proceedings of the 5th International Particle Accelerator Conference* (2014), pp. 267–270.

[108] C. Bruni et al. "Electron Beam Dynamics in the 50 MeV ThomX Compact Storage Ring". In: vol. MOPS050. San Sebastian, Spain: Joint Accelerator Conferences Website, 2011, pp. 715–717.

[109] Wenchao et al. Yan. "High-order multiphoton Thomson scattering". In: *Nature Photonics* 11.8 (2017). ISSN: 1749-4885. DOI: 10.1038/nphoton.2017.100.

[110] A Chauchat et al. "Production and characterisation of inverse compton scattering X-rays witha 17 MEV electron beam". In: *IPAC 2010 - 1st International Particle Accelerator Conference* (2010).

[111] E. S. Sarachik and G. T. Schappert. "Classical Theory of the Scattering of Intense Laser Radiation by Free Electrons". In: *Phys. Rev. D* 1 (10 1970), pp. 2738–2753. DOI: 10.1103/PhysRevD.1.2738.

[112] F. V. Hartemann, D. J. Gibson, and A. K. Kerman. "Classical theory of Compton scattering: Assessing the validity of the Dirac-Lorentz equation". In: *Phys. Rev. E* 72 (2 2005), p. 026502. DOI: 10.1103/PhysRevE.72.026502.

[113] C. Maroli et al. "Nonlinear effects in Thomson backscattering". In: *Phys. Rev. ST Accel. Beams* 16 (3 2013), p. 030706. DOI: 10.1103/PhysRevSTAB.16.030706.

[114] S G Rykovanov et al. "Quasi-monoenergetic femtosecond photon sources from Thomson Scattering using laser plasma accelerators and plasma channels". In: *Journal of Physics B: Atomic, Molecular and Optical Physics* 47.23 (2014), p. 234013. DOI: 10.1088/0953-4075/47/23/234013.

[115] S. G. Rykovanov et al. “Controlling the spectral shape of nonlinear Thomson scattering with proper laser chirping”. In: *Phys. Rev. Accel. Beams* 19 (3 2016), p. 030701. DOI: 10.1103/PhysRevAccelBeams.19.030701.

[116] M. et al. Babzien. “Observation of the Second Harmonic in Thomson Scattering from Relativistic Electrons”. In: *Phys. Rev. Lett.* 96 (5 2006), p. 054802. DOI: 10.1103/PhysRevLett.96.054802.

[117] T. Kumita. “Observation of the nonlinear effect in relativistic Thomson scattering of electron and laser beams”. en. In: *Laser Physics* 16.2 (2006), pp. 267–271. ISSN: 1054-660X, 1555-6611. DOI: 10.1134/S1054660X06020101. (Visited on 11/18/2021).

[118] Y. et al. Sakai. “Observation of redshifting and harmonic radiation in inverse Compton scattering”. In: *Phys. Rev. ST Accel. Beams* 18 (6 2015), p. 060702. DOI: 10.1103/PhysRevSTAB.18.060702.

[119] N. et al. Ranjan. “Simulation of inverse Compton scattering and its implications on the scattered linewidth”. In: *Phys. Rev. Accel. Beams* 21 (3 2018), p. 030701. DOI: 10.1103/PhysRevAccelBeams.21.030701.

[120] Donald P. Umstadter. “All-laser-driven Thomson X-ray sources”. In: *Contemporary Physics* 56.4 (2015), pp. 417–431. DOI: 10.1080/00107514.2015.1023519.

[121] Isaac Ghebregziabher, B. A. Shadwick, and Donald Umstadter. “Spectral bandwidth reduction of Thomson scattered light by pulse chirping”. In: *Phys. Rev. ST Accel. Beams* 16 (3 2013), p. 030705. DOI: 10.1103/PhysRevSTAB.16.030705.

[122] B. Terzić et al. “Narrow-Band Emission in Thomson Sources Operating in the High-Field Regime”. In: *Phys. Rev. Lett.* 112 (7 2014), p. 074801. DOI: 10.1103/PhysRevLett.112.074801.

[123] D. Seipt et al. “Narrowband inverse Compton scattering x-ray sources at high laser intensities”. In: *Phys. Rev. A* 91 (3 2015), p. 033402. DOI: 10.1103/PhysRevA.91.033402.

[124] C. Maroli et al. “Compensation of non-linear bandwidth broadening by laser chirping in Thomson sources”. In: *Journal of Applied Physics* 124.6 (2018), p. 063105. DOI: 10.1063/1.5033549.

[125] J. H. Field. *Retarded electric and magnetic fields of a moving charge: Feynman's derivation of Lienard-Wiechert potentials revisited*. 2015.

[126] Rui Li et al. “Two-dimensional Effects on the Behavior of the CSR Force In a Bunch Compression Chicane”. In: 2011.

[127] Yunhai Cai. “Coherent synchrotron radiation by electrons moving on circular orbits”. In: *Phys. Rev. Accel. Beams* 20 (6 2017), p. 064402. DOI: 10.1103/PhysRevAccelBeams.20.064402.

[128] A D Brynes et al. “Beyond the limits of 1D coherent synchrotron radiation”. In: *New Journal of Physics* 20.7 (2018), p. 073035. DOI: 10.1088/1367-2630/aad21d.

[129] Yunhai Cai and Yuantao Ding. “Three-dimensional effects of coherent synchrotron radiation by electrons in a bunch compressor”. In: *Phys. Rev. Accel. Beams* 23 (1 2020), p. 014402. DOI: 10.1103/PhysRevAccelBeams.23.014402.

[130] K. Floettmann. *ASTRA-A space charge tracking algorithm*.

[131] A Kabel, M Dohlus, and T Limberg. “Using TraFiC4 to calculate and minimize emittance growth due to coherent synchrotron radiation”. In: *Nuclear Instruments and Methods in Physics Research Section A: Accelerators, Spectrometers, Detectors and Associated Equipment* 455.1 (2000), 185–189. ISSN: 0168-9002. DOI: 10.1016/s0168-9002(00)00729-4.

[132] L. Giannessi and M. Quattromini. “TREDI simulations for high-brilliance photoinjectors and magnetic chicanes”. In: *Phys. Rev. ST Accel. Beams* 6 (12 2003), p. 120101. DOI: 10.1103/PhysRevSTAB.6.120101.

[133] A. R. Rossi et al. “Numerical treatment of retarded radiation effects from high brightness electron beams”. In: *Phys. Rev. ST Accel. Beams* 12 (10 2009), p. 104202. DOI: 10.1103/PhysRevSTAB.12.104202.

[134] A. D. Greenwood et al. “On the elimination of numerical Cerenkov radiation in PIC simulations”. In: *Journal of Computational Physics* 201.2 (2004), pp. 665–684. ISSN: 0021-9991. DOI: https://doi.org/10.1016/j.jcp.2004.06.021.

[135] Tsumoru Shintake. “NEW REAL-TIME SIMULATION TECHNIQUE FOR SYNCHROTRON AND UNDULATOR RADIATIONS”. In: 2002.

[136] Roger A. Horn and Charles R. Johnson. *Matrix analysis*. English. Repr. with corr. Cambridge University Press Cambridge [Cambridgeshire] , New York, 1985, xiii, 561 p. ISBN: 0521305861 0521386322.

[137] Ioachim Pupeza et al. “Power scaling of a high-repetition-rate enhancement cavity”. In: *Opt. Lett.* 35.12 (2010), pp. 2052–2054. DOI: 10.1364/OL.35.002052.

[138] H. Carstens et al. “Megawatt-scale average-power ultrashort pulses in an enhancement cavity”. In: *Opt. Lett.* 39.9 (2014), pp. 2595–2598. DOI: 10.1364/OL.39.002595.

[139] L. Amoudry et al. “Modal instability suppression in a high-average-power and high-finesse Fabry–Perot cavity”. In: *Appl. Opt.* 59.1 (2020), pp. 116–121. DOI: 10.1364/AO.59.000116.

[140] Amber L. Bullington et al. “Modal frequency degeneracy in thermally loaded optical resonators”. In: *Appl. Opt.* 47.15 (2008), pp. 2840–2851. DOI: 10.1364/AO.47.002840.

[141] I. et al. Drebot. “BriXs Ultra High Flux Inverse Compton Source Based on Modified Push-Pull Energy Recovery Linacs”. In: *Instruments* 3.3 (2019). ISSN: 2410-390X. DOI: 10.3390/instruments3030049.

[142] Thomas Brabec and Ferenc Krausz. “Intense few-cycle laser fields: Frontiers of nonlinear optics”. In: *Rev. Mod. Phys.* 72 (2 2000), pp. 545–591. DOI: 10.1103/RevModPhys.72.545.

[143] B. Terzić et al. “Improving performance of inverse Compton sources through laser chirping”. In: *EPL (Europhysics Letters)* 126.1 (2019), p. 12003. DOI: 10.1209/0295-5075/126/12003.

[144] Tong Xu et al. “Spectrum bandwidth narrowing of Thomson scattering X-rays with energy chirped electron beams from laser wakefield acceleration”. In: *Applied Physics Letters* 104.1 (2014), p. 013903.

[145] Marcel Ruijter, Vittoria Petrillo, and Matt Zepf. “Decreasing the bandwidth of linear and nonlinear Thomson scattering radiation for electron bunches with a finite energy spread”. In: *Phys. Rev. Accel. Beams* 24 (2 2021), p. 020702. DOI: 10.1103/PhysRevAccelBeams.24.020702.

[146] Stanley W Botchway et al. “Laser-induced radiation microbeam technology and simultaneous real-time fluorescence imaging in live cells”. In: 504 (2012), pp. 3–28.

[147] M.P. Kalashnikov et al. “Broadband amplification of 800-nm pulses with a combination of negatively and positively chirped pulse amplification”. In: *IEEE Journal of Selected Topics in Quantum Electronics* 12.2 (2006), pp. 194–200. DOI: 10.1109/JSTQE.2006.872730.

[148] Henning Stark et al. “1 kW, 10 mJ, 120 fs coherently combined fiber CPA laser system”. In: *Opt. Lett.* 46.5 (2021), pp. 969–972. DOI: 10.1364/OL.417032.

[149] C. Roedel et al. “High repetition rate plasma mirror for temporal contrast enhancement of terawatt femtosecond laser pulses by three orders of magnitude”. In: *Applied Physics B* 103 (2011), p. 295. DOI: 10.1007/s00340-010-4329-7.

[150] Aurelie Jullien et al. “Carrier-envelope-phase stable, high-contrast, double chirped-pulse-amplification laser system”. In: *Opt. Lett.* 39.13 (2014), pp. 3774–3777. DOI: 10.1364/OL.39.003774.

[151] Kei Nakamura et al. “Diagnostics, Control and Performance Parameters for the BELLA High Repetition Rate Petawatt Class Laser”. In: *IEEE Journal of Quantum Electronics* 53.4 (2017), pp. 1–21. DOI: 10.1109/JQE.2017.2708601.

[152] M. Pittman et al. “Design and characterization of a near-diffraction-limited femtosecond 100-TW 10-Hz high-intensity laser system”. en. In: *Applied Physics B* 74.6 (2002), pp. 529–535. ISSN: 0946-2171, 1432-0649. DOI: 10.1007/s003400200838. (Visited on 12/22/2021).

[153] Zhirong Huang, Yuantao Ding, and Carl B Schroeder. “Compact X-ray free-electron laser from a laser-plasma accelerator using a transverse-gradient undulator”. In: *Physical review letters* 109.20 (2012), p. 204801.

[154] Robert Rossmanith et al. “A Novel Optical Beam Concept for Producing Coherent Synchrotron Radiation with Large Energy Spread Beams”. In: (2017), pp. 2646–2649.

[155] Farzad Jafarinia. “Studies on Experiments and Free-Electron laser concepts with a Transverse Gradient Undulator”. English. PhD thesis. Physics, 2021.

[156] K. Osvay et al. “Angular dispersion and temporal change of femtosecond pulses from misaligned pulse compressors”. In: *IEEE Journal of Selected Topics in Quantum Electronics* 10.1 (2004), pp. 213–220. DOI: 10.1109/JSTQE.2003.822917.

[157] Selcuk Akturk et al. “Pulse-front tilt caused by spatial and temporal chirp”. In: *Optics express* 12 (Oct. 2004), pp. 4399–410. DOI: 10.1364/OPEX.12.004399.

[158] A. et al. Bacci. “Electron Linac design to drive bright Compton back-scattering gamma-ray sources”. In: *Journal of Applied Physics* 113.19 (2013), p. 194508. DOI: 10.1063/1.4805071.

[159] Vasily Yu. Kharin, Daniel Seipt, and Sergey G. Rykovanov. “Higher-Dimensional Caustics in Nonlinear Compton Scattering”. In: *Phys. Rev. Lett.* 120 (4 2018), p. 044802. DOI: 10.1103/PhysRevLett.120.044802.

[160] G. G. et al. Paulus. “Measurement of the Phase of Few-Cycle Laser Pulses”. In: *Phys. Rev. Lett.* 91 (25 2003), p. 253004. DOI: 10.1103/PhysRevLett.91.253004.

[161] Shinichi Fukahori et al. “Determination of the absolute carrier-envelope phase by angle-resolved photoelectron spectra of Ar by intense circularly polarized few-cycle pulses”. In: *Phys. Rev. A* 95 (5 2017), p. 053410. DOI: 10.1103/PhysRevA.95.053410.

[162] I. et al. Orfanos. “Attosecond pulse metrology”. In: *APL Photonics* 4.8 (2019), p. 080901. DOI: 10.1063/1.5086773.

[163] Qingcao et al. Liu. “Ionization-Induced Subcycle Metallization of Nanoparticles in Few-Cycle Pulses”. In: *ACS Photonics* 7.11 (2020), pp. 3207–3215. DOI: 10.1021/acsphotonics.0c01282.

[164] F. Mackenroth, A. Di Piazza, and C. H. Keitel. “Determining the Carrier-Envelope Phase of Intense Few-Cycle Laser Pulses”. In: *Phys. Rev. Lett.* 105 (6 2010), p. 063903. DOI: 10.1103/PhysRevLett.105.063903.

[165] Marcel Ruijter et al. “Signatures of the Carrier Envelope Phase in Nonlinear Thomson Scattering”. In: *Crystals* 11.5 (2021). ISSN: 2073-4352. DOI: 10.3390/cryst11050528.

Acknowledgements

By the time I will have submitted my thesis it will be three years, three months and one week since I started my PhD. I would imagine that under normal circumstances one would already reflect on life through the PhD, now even more so with a pandemic disrupting life.

To start I would like to express my thanks to:
Barbara Kirchner, who got me into contact with Luca Serafini, and made my PhD adventure possible.
Vittoria Petrillo with her help in temporary housing, bureaucracy, and in having my back. I also look fondly back to the walks we made together during the less severe times of the pandemic, to talk about physics & life, but also me listening to a lot of Italian/Milanese history.

I want to thank my parents Eduard Ruijter and Agnes Póka for their support and supplying me with ample amounts of liquorish and stroopwafels, and my siblings László and Judit Ruijter. I am really happy they visited me during the first summer of my PhD.

A special thanks goes to Julia Järnström, my girlfriend, that encouraged and supported me so much over this period.

Although some hundreds of kilometres away, my good friend Thomas C. Teter was, and still is, always ready for a call; to talk about what we are working on, to discuss something less-related-to-us-physics, or just whatever the day brought to us. On a similar note I want to thank Matthijs Wagemakers. Further I want to thank Riccardo Martini, Tieke Jansen, Victor Zuza and Olga Rusyakina for their lasting friendship. And a special thanks to my friend and former room-mate with whom I stayed in quarantine during the strictest lockdown, his feedback on my food and, on that regard, his tireless insistence on using the proper yeast for the pizza dough: Vincenzo Pavese. I want to thank Michele Opromolla & Marcello Rossetti Conti for their comradery.

On a more professional note:
I want to thank my previous supervisors from the days back in Jena, Germnay: Matt Zepf, Sergey Rykovanov, Vasily Kharin. Through whom I started the theoretical/analytical endeavour on high energy laser-electron. Sometimes I still look into the numerics and analytics worked out with the help of Vasily.

I want to thank my current super visors Vittoria Petrillo & Luca Serafini and the research group: Michele Opromolla, Marcello Rossetti Conti, Andrea Rossi, Alberto Bacci, Illya Drebot, Sanae Samsam and Cesare Maroli, for their collegiality and friendly discussions.

I also want to express my thanks the one anonymous referee (on [145]) that was exceptionally great in helping me shape my academic writing into (hopefully) something more proper.

"Et Al is the greatest scientist, he's on all the papers! "
- Hosea Jan "Ze" Frank

Appendix A

Derivations Equation of Motion

A.1 Force relations

Lorentz Force
The Lorentz force is given by

$$\frac{dU^\mu}{ds} = \frac{q}{mc^2} F^{\mu\nu} U_\nu = \frac{q}{mc^2} (\partial^\mu A^\nu - \partial^\nu A^\mu) U_\nu. \tag{A.1}$$

The prefactors can be combined with the vector-potential, since the definition of the four-velocity used here is dimensionless, to the normalized vector potential

$$a^\mu = \frac{q}{mc^2} A^\mu \tag{A.2}$$

Landau-Lifshitz
Starting from the Lorentz-Abraham-Dirac equation [XXX]

$$\frac{dU^\mu}{ds} = \frac{q}{mc^2} F^{\mu\nu} U_\nu + \frac{2e^2}{3mc^2} F^\mu_{rad} \tag{A.3}$$

$$F^\mu_{rad} = \left(\frac{d^2U^\mu}{ds^2} - U^\mu U^\nu \frac{d^2U_\nu}{ds^2} \right) \tag{A.4}$$

The approximation made by Landau & Lifshitz [XXX] is to take the second derivative of the velocity as the derivative of the Lorentz Force, as shown below.

$$\frac{d^2U}{ds^2} = \frac{q}{mc^2} \frac{d}{ds} F^{\mu\nu} U_\nu = \frac{q}{mc^2} \left(\partial_\gamma F^{\mu\nu} U_\nu U^\gamma + F^{\mu\nu} F_{\nu\beta} U^\beta \right), \tag{A.5}$$

where the partial derivative acts on the components of the electromagnetic field tensor. Substitution results in the Landau-Lifshitz equation of motion

$$\frac{dU^\mu}{ds} = \frac{q}{mc^2} F^{\mu\nu} U_\nu + \frac{2e^2}{3mc^2} F^\mu_{rad} \tag{A.6}$$

$$\frac{dU^\mu}{ds} = \frac{q}{mc^2} F^{\mu\nu} U_\nu + \frac{2q^2}{3mc^2} \left(\frac{q}{mc^2} \partial_\gamma F^{\mu\nu} U_\nu U^\gamma + \left(\frac{q}{mc^2} \right)^2 \left(F^{\mu\nu} F_{\nu\beta} U^\beta - F_{\nu\beta} F^{\beta\alpha} U_\alpha U^\nu U^\mu \right) \right). \tag{A.7}$$

A.2 Electron - Constant Electric Field - Lorentz Force

An electron in a constant electric field will accelerate in the direction of that field. Here we will take $\vec{E} = E_0\hat{z}$. The equations of motion are then given by

$$\frac{dU^0}{ds} = -\frac{eE_0}{mc^2}U^3 \tag{A.8}$$
$$\frac{dU^1}{ds} = 0 \tag{A.9}$$
$$\frac{dU^2}{ds} = 0 \tag{A.10}$$
$$\frac{dU^3}{ds} = -\frac{eE_0}{mc^2}U^0 \tag{A.11}$$

Subtracting the last relation from the first we find $\frac{dU^0-U^3}{ds} = \frac{eE_0}{mc^2}(U^0 - U^3)$. This can readily be solved by separating the variables

$$U^0 - U^3 = \exp\left[\frac{eE_0}{mc^2}s + C\right], \tag{A.12}$$

where C depends on the initial conditions and equals to $\exp[C] = \gamma(0)(1-\beta_z(0))$. Using the magnitude relation of the four-velocity we can find the solutions of the equation of motion

$$U_\mu U^\mu = 1 = (U^0)^2 - (U^1)^2 - (U^2)^2 - (U^3)^2, \tag{A.13}$$
$$1 = (U^0 + U^3)(U^0 - U^3) - (U_\perp)^2, \tag{A.14}$$

where $(U_\perp)^2 = \gamma^2(0)\left[\beta_x^2(0) + \beta_y^2(0)\right]$. The solutions for the four-velocity are

$$U^\mu = \begin{pmatrix} \cosh\left(\frac{eE_0}{mc^2}s + C\right) + \frac{U_\perp^2 \exp\left[-\left(\frac{eE_0}{mc^2}s+C\right)\right]}{2} \\ \gamma(0)\beta_x(0) \\ \gamma(0)\beta_y(0) \\ -\sinh\left(\frac{eE_0}{mc^2}s + C\right) + \frac{U_\perp^2 \exp\left[-\left(\frac{eE_0}{mc^2}s+C\right)\right]}{2} \end{pmatrix} \tag{A.15}$$

A.3 Electron - Constant Magnetic field - Lorentz Force

The equations of motion for an electron in a constant magnetic field in $+\hat{y}$ governed by the Lorentz Force are given by

$$\frac{dU^0}{ds} = 0 \tag{A.16}$$
$$\frac{dU^1}{ds} = \frac{eB_0}{mc^2}U^3 \tag{A.17}$$
$$\frac{dU^2}{ds} = 0 \tag{A.18}$$
$$\frac{dU^3}{ds} = -\frac{eB_0}{mc^2}U^1 \tag{A.19}$$

From the first relation we find that not only is the energy ($U^0 = \gamma$) constant but also $ds = \frac{dct}{\gamma} \rightarrow s = \frac{ct}{\gamma}$. There are several ways to solve for the perpendicular motion, here we take the method of introducing $V = U^1 + iU^3$. For which we find

$$\frac{dV}{ds} = \frac{dU^1}{ds} + i\frac{dU^3}{ds} = -i\Omega V, \tag{A.20}$$

where $\Omega = \frac{eB_0}{mc^2}$. This equation has the solution $V = A\exp[-i\Omega(s+s_0)] = U^1 + iU^3 = A\,(cos(\Omega(s+s_0)) - i\sin(\Omega(s+s_0)))$. The constant A can be found by taking $|V| = A = \gamma\sqrt{\beta_x^2+\beta_y^2} = \gamma\beta_\perp$

The final solution is thus given by

$$U^\mu = \gamma \begin{pmatrix} 1 \\ \beta_\perp \cos(\frac{eB_0}{\gamma mc^2}(ct + ct_0)) \\ \beta_y(0) \\ -\beta_\perp \sin(\frac{eB_0}{\gamma mc^2}(ct + ct_0)) \end{pmatrix} \tag{A.21}$$

and upon integration

$$X^\mu = \begin{pmatrix} ct \\ R\sin(\frac{eB_0}{\gamma mc^2}(ct + ct_0)) \\ \beta_y(0)ct \\ R\cos(\frac{eB_0}{\gamma mc^2}(ct + ct_0)) \end{pmatrix}, \tag{A.22}$$

where $R = \frac{\gamma\beta_\perp mc^2}{eB_0}$. The argument of the sinusoidal functions can be rewritten into $\frac{eB_0}{\gamma mc^2}ct = \frac{\beta_\perp}{R}ct$.

A.4 Electron - Constant Magnetic field - Landau-Lifshitz equation

Here we follows the solutions provided in [Elkina2014]. The derivative of constant magnetic field (in space and time) is zero and therefore the term containing the partial derivative in Eq. A.7 vanishes. To be explicit the equation of motion for an electron in a constant magnetic field in $+\hat{y}$ is given by

$$\frac{dU^\mu}{ds} = -\frac{e}{mc^2}\begin{pmatrix} 0 \\ -U^3 \\ 0 \\ U^1 \end{pmatrix} + \frac{2e^2}{3mc^2}\left(\frac{e}{mc^2}\right)^2 \left[\begin{pmatrix} 0 \\ -U^1 \\ 0 \\ -U^3 \end{pmatrix} - \left((U^1)^2 + (U^3)^2\right)\begin{pmatrix} U^0 \\ U^1 \\ U^2 \\ U^3 \end{pmatrix}\right] \tag{A.23}$$

For abbreviation we will use $\frac{e}{mc^2} = \Omega$ and $\mathscr{E} = \frac{2e^2}{3mc^2}$ Since without the friction term we have to solution of a particle travelling along a circular trajectory (for the components perpendicular to the magnetic field) the authors of [Elkina2014] rightfully assume that the solution including a small friction force will have a similar solution.

$$\begin{pmatrix} U^1 \\ U^3 \end{pmatrix} = U_\perp \begin{pmatrix} \cos(\phi) \\ -\sin(\phi) \end{pmatrix} \tag{A.24}$$

where $U_\perp = \sqrt{(U^1)^2 + (U^3)^2}$. We will first look at how this term behaves upon taking the derivative

$$\frac{d}{ds}\sqrt{(U^1)^2 + (U^3)^2} = \frac{U^1\frac{dU^1}{ds} + U^3\frac{dU^3}{ds}}{\sqrt{(U^1)^2 + (U^3)^2}}. \tag{A.25}$$

Now we can use the derivatives from Eq. A.23 to find that

$$U^1\frac{dU^1}{ds} + U^3\frac{dU^3}{ds} = -\mathscr{E}\Omega^2(1 + U_\perp^2)U_\perp \tag{A.26}$$

Combining the last two equations and separating the variables we find

$$\frac{dU_\perp}{(1+U_\perp^2)U_\perp} = -\mathscr{E}\Omega^2 ds \tag{A.27}$$

$$U_\perp = \frac{U_\perp(0)}{\sqrt{(1+U_\perp(0)^2)\exp[2ks] - U_\perp(0)^2}} \tag{A.28}$$

where $k = \mathscr{E}\Omega^2$ To find the solution for ϕ we look at the

$$\frac{dU^1}{ds} = \frac{dU_\perp}{ds} cos(\phi) - U_\perp sin(\phi) \frac{d\phi}{ds} \tag{A.29}$$

$$= -\Omega(-U^3) + \mathscr{E}\Omega^2 \left[-U^1 - U_\perp U^1\right] \tag{A.30}$$

Rewriting the terms we in the end find

$$\frac{d\phi}{ds} = \Omega \tag{A.31}$$

Now there are two components left to solve for which are of the form $\frac{d}{ds} f = f g(s)$ which can (also) be solved using separation of variables. The final result for the motion is given by

$$U^\mu = \begin{pmatrix} \frac{U^0(0)\exp[ks]}{\sqrt{U_\perp(0)(\exp[2ks]-1)+\exp[2ks]}} \\ \frac{U_\perp^2}{\sqrt{(1+U_\perp(0)^2)\exp[2ks]-U_\perp(0)^2}} \cos(\Omega s) \\ -\frac{U_\perp^2}{\sqrt{(1+U_\perp(0)^2)\exp[2ks]-U_\perp(0)^2}} \sin(\Omega s) \\ \frac{U^3(0)\exp[ks]}{\sqrt{U_\perp(0)(\exp[2ks]-1)+\exp[2ks]}} \end{pmatrix} \tag{A.32}$$

A.5 Electron - Plane Wave interaction - Lorentz Force

The (four-) vector potential for a plane wave propagating in the +z direction is given by

$$A^\mu = a_0 \mathscr{E}(\zeta) e^{i\zeta} \begin{pmatrix} 0 \\ 1 \\ 0 \\ 0 \end{pmatrix}, \tag{A.33}$$

for linear polarization and

$$A^\mu = a_0 \mathscr{E}(\zeta) e^{i\zeta} \begin{pmatrix} 0 \\ 1 \\ i \\ 0 \end{pmatrix}, \tag{A.34}$$

for circular polarization, where $\zeta = k(ct - z)$. This coordinate can also be expressed in terms $\zeta = K_\mu X^\mu = K'_\mu X'^\mu$.

$$K^\mu = \begin{pmatrix} \frac{\omega}{c} \\ 0 \\ 0 \\ k \end{pmatrix}, \quad X^\mu = \begin{pmatrix} ct \\ x \\ y \\ z \end{pmatrix} \tag{A.35}$$

$$K'^\mu = \begin{pmatrix} \gamma(1+\beta)\frac{\omega}{c} \\ 0 \\ 0 \\ \gamma(1+\beta)k \end{pmatrix}, \quad X'^\mu = \begin{pmatrix} \gamma ct + \gamma\beta z \\ x \\ y \\ \gamma\beta ct + \gamma z \end{pmatrix} \tag{A.36}$$

The derivation here will take the latter as the necessary steps are equal for the former.

Taking the electromagnetic field tensor as the partial derivatives of the vector potential, we obtain the following set of equations

$$\frac{dU^0}{ds} = -\left(\partial^0 a^1 U_1 + \partial^0 a^2 U_2\right) \tag{A.37}$$
$$\frac{dU^1}{ds} = -\left(-\partial^0 a^1 U_0 - \partial^3 a^1 U_3\right) \tag{A.38}$$
$$\frac{dU^2}{ds} = -\left(-\partial^0 a^2 U_0 - \partial^3 a^2 U_3\right) \tag{A.39}$$
$$\frac{dU^3}{ds} = -\left(\partial^3 a^1 U_1 + \partial^3 a^2 U_2\right). \tag{A.40}$$

The Eq. A.38 can be rewritten by noticing $\partial^0 a^1 U_0 + \partial^3 a^1 U_3 = \partial^0 a^1 \frac{dX^0}{ds} + \partial^3 a^1 \frac{dX^3}{ds} = \frac{da^1}{ds}$, and leads to the result that the transverse motion is

$$U_\perp = a_\perp \tag{A.41}$$

Second, since $\partial_0 \zeta = -\partial_3 \zeta$ difference between the Eq. A.37 and A.40 is zero, and taking the initial condition of the electron as $U^\mu(ct = 0) = \gamma(1, 0, 0, -\beta)$, i.e. a head-on collision, we obtain

$$\frac{dU^0 - U^3}{ds} = 0, \tag{A.42}$$
$$U^0 - U^3 = \text{const} = \gamma(1+\beta), \tag{A.43}$$
$$\frac{dX^0 - X^3}{ds} = \frac{1}{k}\frac{d\zeta}{ds} = \gamma(1+\beta). \tag{A.44}$$

The last equation has an important physical interpretation: the motion of the electron is in phase with the driving EM field. To find the final solution to the motion we use the relation

$$U_\mu U^\mu = 1 = (U^0)^2 - (U^1)^2 - (U^2)^2 - (U^3)^2, \tag{A.45}$$
$$1 = (U^0 + U^3)(U^0 - U^3) - (a)^2, \tag{A.46}$$

where $(a)^2 = -a_\mu a^\mu$ Using the previously obtained solutions the motion of the electron is solved and reads

$$U^\mu = \begin{pmatrix} \gamma + \frac{(a)^2}{2}\gamma(1-\beta) \\ a^1 \\ a^2 \\ -\gamma\beta + \frac{(a)^2}{2}\gamma(1-\beta) \end{pmatrix} \tag{A.47}$$

A.6 Electron - Undulator

The equations of motion for an electron traversing an undulator are often solved using the three vector Lorentz Force equation in combination with the magnetic field, see textbooks like [Schmüser]. Moreover, the solutions of the motion are derived by starting with an approximation: that the velocity perpendicular to the magnetic field is taken constant (first order) and using the solution of the transverse velocity to produce a second order solution of the perpendicular velocity.

These approximations are unnecessary when four-vectors are used and an exact solution can be derived as follows. The vector potential of an undulator is given by (This field is equivalent to the magnetic field as given in [Schmüser] and can be shown by using $\vec{B} = \nabla \times \vec{A}$, through which we find that $B_0 = A_0 k_u$)

$$A^\mu = A_0 \cosh(k_u y) \sinh(k_u z) \begin{pmatrix} 0 \\ 1 \\ 0 \\ 0 \end{pmatrix} \tag{A.48}$$

If we consider an electron to travel on-axis, i.e. $y = 0$ & $\beta_y = 0$, and use the normalization $a_0 = \frac{eA_0}{mc^2}$ we find the following equations of motion

$$\frac{dU^0}{ds} = 0 \tag{A.49}$$
$$\frac{dU^1}{ds} = -\partial^3 a^1 U_3 \tag{A.50}$$
$$\frac{dU^2}{ds} = 0 \tag{A.51}$$
$$\frac{dU^3}{ds} = -\partial^3 a^1 U_1. \tag{A.52}$$

Here we can use again that $\frac{da^1(X^3)}{ds} = \partial_3 a^1 U^3$ and thus find that the transverse velocity equals the vector potential. The second step is to use the magnitude of the four-velocity

$$U^\mu U_\mu = 1 = (U^0)^2 - (U^1)^2 - (U^2)^2 - (U^3)^2 \tag{A.53}$$
$$U^3 = \sqrt{\gamma^2 - (1 + (a)^2)}, \tag{A.54}$$

where $(a)^2 = -a^\mu a_\mu$ is the magnitude squared of the vector potential. Thus the solution to the velocity is given by

$$U^\mu = \begin{pmatrix} \gamma \\ a^1 \\ 0 \\ \sqrt{\gamma^2 - (1 + (a)^2)} \end{pmatrix} \tag{A.55}$$

Note that in literature " the undulator parameter K" is usually found instead of the normalized vector potential a_0. They are equivalent, however, from a theoretical point this amplitude is better expressed as the vector potential as it is not inherently related to the magnetic field of an undulator.

To obtain the position of the particle we will need to integrate, and since γ =constant we end up with the following relation

$$\frac{dX^3}{ds} = \sqrt{\gamma^2 - (1 + (a)^2)} \tag{A.56}$$
$$\frac{dX^3}{dct} = \sqrt{1 - \frac{(1 + (a)^2)}{\gamma^2}} \frac{dX^3}{\sqrt{1 - \frac{(1+(a)^2)}{\gamma^2}}} = dct \tag{A.57}$$

This last equation does have an analytical expression that contains an elliptic integral of the first kind, but it does not give any meaningful insight to the problem at hand nor does it make the integral for the transverse velocity component easier. Thus, here, we take the series of U^3.

$$U^3 = \sqrt{\gamma^2 - (1 + (a)^2)} \tag{A.58}$$
$$\approx \gamma \left[1 - \frac{1 + \frac{a_0^2}{2}}{2\gamma^2} - \left(\frac{a_0}{2\gamma} \right)^2 \cos(2k_u z) \right] \tag{A.59}$$

Here there are two ways to find the solution:
1) Separation of variables, for which the solution is given by

$$X^3 = -\frac{1}{k_u} \tan^{-1} \left(\frac{\sqrt{(B^2 - A^2)}}{A + B} \tanh(k_u \sqrt{B^2 - A^2} ct) \right) \tag{A.60}$$

where $A = 1 - \frac{1+\frac{{a_0}^2}{2}}{2\gamma^2}$ and $B = \left(\frac{a_0}{2\gamma}\right)^2$.
2) Make the approximation that Eq. A.59 can be read as a drift velocity and a fast oscillatory function with a small amplitude. The oscillatory function is then considered negligible and we find

$$X^\mu = \begin{pmatrix} ct \\ \frac{a_0}{\bar{\beta}_z k_u \gamma} \sin(k_u \bar{\beta}_z ct) \\ 0 \\ \bar{\beta}_z ct - \left(\frac{a_0}{2\gamma}\right)^2 \frac{\sin(2k_u \bar{\beta}_z ct)}{2k_u} \end{pmatrix}, \tag{A.61}$$

where the drift velocity is $\bar{\beta}_z = 1 - \frac{1+\frac{{a_0}^2}{2}}{2\gamma^2}$.

Appendix B

Derivations & Additional information for Retarded Time

B.1 Cardano's Formula

A polynomial of third order is given by

$$ax^3 + bx^2 + cx + d = 0 \tag{B.1}$$

and its real root be solved by first depressing it to the form

$$t^3 + pt + q = 0, \tag{B.2}$$

where $t = x + \frac{b}{3a}$, $p = \frac{3ac-b^2}{3a^2}$ and $q = \frac{2b^3-3^2abc+3^3a^2d}{3^3a^3}$. Then Cardano's formula can be used, which is given by

$$t = \mathscr{CF}(p,q) = \sqrt[3]{-\frac{q}{2} + \sqrt{\left(\frac{q}{2}\right)^2 + \left(\frac{p}{3}\right)^3}} + \sqrt[3]{-\frac{q}{2} - \sqrt{\left(\frac{q}{2}\right)^2 + \left(\frac{p}{3}\right)^3}}. \tag{B.3}$$

B.2 Derivation Analytical Approximation $c\tau$ 1D circular motion

B.2.1 Fraction of radiation cone

We start by splitting the transcendental equation B.9 into two parts and subtracting them one from another

$$\frac{\alpha}{2} = \frac{\beta c\tau}{2R} + \frac{\delta\vartheta}{2} \tag{B.4}$$

$$\frac{c\tau}{2R} = \beta \sin(\tfrac{\alpha}{2}) \tag{B.5}$$

$$c\tau = 2R(1+\beta)\gamma^2\left(\sin(\tfrac{\alpha}{2}) - \tfrac{\alpha}{2} + \tfrac{\delta\vartheta}{2}\right) \tag{B.6}$$

Now we assume that r_o lies on a fraction of the radiation cone of r_s', i.e. $\frac{\alpha}{2} = \frac{1}{f\gamma}$. Now we take the series of the sine function up to third order ($\sin\left(\frac{1}{f\gamma}\right) = \frac{1}{f\gamma} - \frac{1}{3!}\left(\frac{1}{f\gamma}\right)^3$) and substitute it into Eq. B.9, which gives us the following function

$$\frac{\delta\vartheta\gamma^3}{2} = \frac{1}{(1+\beta)f} + \frac{1}{3!f^3} \tag{B.7}$$

Now we set $1+\beta_s \approx 2$ and using Cardano's formula (Eq. B.3) we can calculate the fraction f for the given $\delta\vartheta$ and γ_s. We also calculate a new energy γ_f using Eq. B.7, which corresponds to the energy for which

$c\tau(\gamma)$ and $\frac{1}{f\gamma_s}$ intersect (see Figure 3.11). Finally we substitute f and γ_f in Eq. B.6 and obtain

$$c\tau(f) = 2R\sqrt{1-\left(\frac{3\delta\vartheta}{3f^2+1}\right)^{\frac{2}{3}}}\left(\sqrt[3]{\frac{3\delta\vartheta}{3f^2+1}}-\frac{\delta\vartheta}{2}\right) \tag{B.8}$$

B.2.2 Geometric $\mathcal{O}(4)$ Polynomial 2D motion

The relation of the retarded time for a particle travelling along a circular trajectory can be expressed using the law of cosines

$$c\tau^2 = r_s'^2 + r_o^2 - 2r_s' r_o \cos\left(\frac{\beta_s c\tau}{R} + \delta\vartheta\right) \tag{B.9}$$

We start by taking the series of the cosine up to fourth order at $\delta\vartheta$. This gives us

$$c\tau^2 = r_s'^2 + r_o^2 - 2r_s' r_o \left[\cos(\delta\vartheta) - \sin(\delta\vartheta)\left(\frac{\beta_s c\tau}{R}\right) - \frac{\cos(\delta\vartheta)}{2!}\left(\frac{\beta_s c\tau}{R}\right)^2 + \frac{\sin(\delta\vartheta)}{3!}\left(\frac{\beta_s c\tau}{R}\right)^3 + \frac{\cos(\delta\vartheta)}{4!}\left(\frac{\beta_s c\tau}{R}\right)^4\right] \tag{B.10}$$

Since the source travels along a circle the magnitude $|r_s'| = |r_s| = R$. Therefore the leading terms on the rights hand side are simply $r_s^2 + r_o^2 - 2r_s r_o\cos(\delta\vartheta) = \delta r^2$. From numerical observation, we know that $c\tau \sim$[cm] for the (electric) field travelling in the forward direction. Within the domain of small angles ($\delta\vartheta$) and that r_o lies on the circle too, we can safely assume δr^2 is negligible. In fact, the other terms in the polynomial are on the order of δr. This turns the equation above to a third order polynomial. Reordering gives us

$$\left(\frac{\beta_s c\tau}{2R}\right)^3 + \left(\frac{\beta_s c\tau}{2R}\right)^2 2\tan(\delta\vartheta) + \left(\frac{\beta_s c\tau}{2R}\right)3\frac{\frac{1}{\beta^2}-\cos(\delta\vartheta)}{\cos(\delta\vartheta)} - 3\tan(\delta\vartheta) = 0 \tag{B.11}$$

This third order equation can be depressed, i.e. written in $t^3 + pt + q = 0$, with $p = \frac{3ac-b^2}{3a^2}$ and $q = \frac{2b^3-3^2abc-3^3a^2d}{(3a)^3}$. Since the coefficients (a,b,c,d) of the polynomial are on the same order and small, in the depressed form we disregard the quadratic terms, i.e. $p \approx c$ and $q \approx d$. Finally we approximate the trigonometric functions up to first order and stress that directionality is important, that is $\cos(\delta\vartheta) \approx 1$ and $\tan(\delta\vartheta) \approx \text{sign}(\vec{\delta r}\cdot\vec{\beta}_s)\delta\vartheta \approx \hat{\delta r}\cdot\hat{\beta}_s\frac{\delta r}{R}$. The resulting polynomial is

$$X^3 + X3\left(\frac{1}{\beta_s^2}-1\right) - 3\frac{\vec{\delta r}\cdot\vec{\beta}_s}{R\beta_s} = 0 \tag{B.12}$$

where $X = \left(\frac{\beta_s c\tau}{2R}\right) - \frac{2\tan(\delta\vartheta)}{3}$. Now Cardano's Formula (B.3) can be used to obtain the solution for X. From observations the quantity $\left(\frac{\beta_s c\tau}{2R}\right) \gg \frac{2\tan(\delta\vartheta)}{3}$, meaning that $X \approx \left(\frac{\beta_s c\tau}{2R}\right)$.

Appendix C

Derivation Spectral Equations

In this section the approximate solution to the spectral (double differential) equation for a single electron in a plane wave is derived. The double differential equation is given by

$$\frac{d^2I}{d\omega d\Omega} = \frac{e^2}{4\pi^2 c}\left|\frac{\omega}{c}\int_{-\infty}^{\infty} dct\,\hat{n}\times\hat{n}\times\vec{\beta}\exp\left[i\frac{\omega}{c}(ct-\hat{n}\cdot\vec{r})\right]\right|^2. \tag{C.1}$$

We can rewrite this equation in terms of ζ, since the equations of motion are expressed in terms of it (Eq. A.47). Thus $dct\vec{\beta} = \frac{dct}{\gamma}\gamma\beta = ds\vec{U} = d\zeta\frac{\vec{U}}{k\gamma(1+\beta)}$. Moreover, the terms in the exponential can be rewritten as an integral of the four-velocities with respect to ζ: $ct-\hat{n}\cdot\vec{r} = \int_{-\infty}^{s} ds' U^0 - \hat{n}\vec{U} = \int_{-\infty}^{\zeta} d\zeta' \frac{U^0-\hat{n}\cdot\vec{U}}{k\gamma(1+\beta)}$. Thus the double differential in terms of the laser phase is given by

$$\frac{d^2I}{d\omega d\Omega} = \frac{e^2}{4\pi^2 c}\left|\nu\gamma(1+\beta)\int_{-\infty}^{\infty} d\zeta\,\hat{n}\times\hat{n}\times\vec{U}\exp\left[i\nu\gamma(1+\beta)\int_{-\infty}^{\zeta} d\zeta' U^0 - \hat{n}\cdot\vec{U}\right]\right|^2, \tag{C.2}$$

where $\nu = \frac{\omega}{\omega_l}\frac{1}{\gamma^2(1+\beta)^2}$. Due to non-linearity of the motion of the electron (Eq. A.47) there are no exact solutions to the integral above. However, by utilizing the oscillatory behaviour one can find useful relations and make accurate approximations.

Here we will focus on a single observation angle; the backscattered case ($\vartheta = \pi$: $\hat{n} = -1\hat{z}$).

C.1 Phase Approximations

Solutions for integrals where the integrand is a highly oscillating functions exist in the form of approximations: where the integrand oscillates rapidly, the contributions to the integral are negligible and only the points where the integrand oscillates slowly contribute. The integral in the general form is given by

$$\mathscr{I} = \int dx g(x)\exp[if(x)]. \tag{C.3}$$

If $f(x) = f(x,k)$, with k being the complementary variable, the equation is a generalized Fourier transform. The phase function $f(x)$ is Taylor expanded around points (λ) that contribute to the integral.

$$f(x) \approx f(\lambda) + \left.\frac{df(x)}{dx}\right|_\lambda (x-\lambda) + \left.\frac{d^2f(x)}{dx^2}\right|_\lambda \frac{(x-\lambda)^2}{2!} + \left.\frac{d^3f(x)}{dx^3}\right|_\lambda \frac{(x-\lambda)^3}{3!} + \mathscr{O}(4) \tag{C.4}$$

To the values for λ are found by setting one of the derivatives to zero and is explained further below.

Stationary Phase Approximation

Stationary phase points are those for which $\frac{df(x)}{dx} = 0$. For these points the Taylor expansion only needs to be taken up to quadratic order. Substitution of the expansion into Eq. C.3 leads to a Gaussian integral

for which the solution is

$$\mathscr{I} \approx \exp[if(\lambda)] \exp\left[i\frac{\mu\pi}{4}\right] \sqrt{\frac{2\pi}{\left|\frac{d^2 f(x)}{dx^2}\Big|_\lambda\right|}}. \tag{C.5}$$

This solution can only be used for stationary points where $\frac{d^2 f}{dx^2}\Big|_\lambda \neq 0$. The next section will describe the case for when this condition is not met. Figure C.1 shows two examples: one function for which the stationary phase approximation can be used, and a second function that is a generalized Fourier transform for which the stationary phase approximation can be used conditionally.

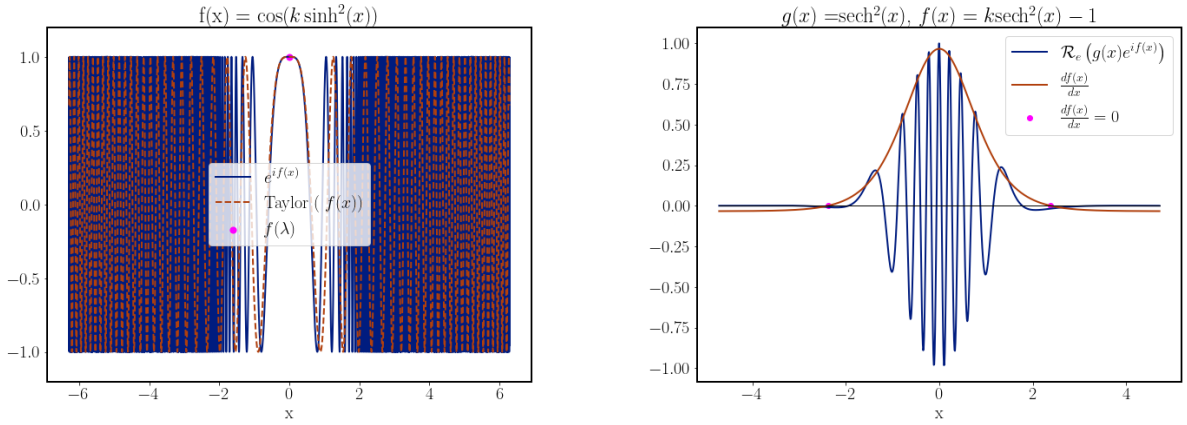

Figure C.1: Examples of the stationary phase approximation.
Left: The function contains a single stationary point and clearly shows that the contribution comes from where the change of the phase is small. The solution of the integral are 0.637 and 0.627 for numerical and Eq. C.5 respectively.
Right: The function represents a generalized Fourier transform. The parameter k changes the vertical position of $\frac{df}{dx}$ and thus provides different contributions for different frequencies. For one value of k the stationary point is at $\lambda = 0$, for which $\frac{d^2 f}{dx^2}\Big|_\lambda = 0$. For this point the solution of Eq. C.5 is not applicable. For all other values of k there exist two stationary phase points.

Zero Convexity

A point for which $\frac{d^2 f}{dx^2} = 0$ is called a zero convexity point. In such cases the solution to the integral is found by taking Taylor expansion up to the cubic term. Using the definition of the Airy function

$$\text{Ai}(z) = \frac{1}{2\pi}\int_{-\infty}^{\infty} dt \exp\left[i\left(zt - \frac{t^3}{3}\right)\right], \tag{C.6}$$

the approximated solution of Eq. C.3 is then given by

$$\mathscr{I} \approx \exp[if(\lambda)]\text{Ai}\left(\frac{df}{dx}\Big|_\lambda \sqrt[3]{\frac{1}{2}\frac{d^3 f(x)}{dx^3}\Big|_\lambda}\right). \tag{C.7}$$

C.2 PW Linear Polarization

The normalized vector potential of a linearly polarized plane wave (laser pulse) propagating in $+z$ is given by

$$a^{\mu} = a_0 \mathscr{E}(\zeta) \mathscr{R}_e \left(e^{i\eta(\zeta)+\eta_0} \begin{pmatrix} 0 \\ 1 \\ 0 \\ 0 \end{pmatrix} \right), \tag{C.8}$$

Substitution of the laser field into Eq. C.2 (through also Eq. A.47) leads to

$$\frac{d^2 I}{d\omega d\Omega} \propto \left| \nu\gamma(1+\beta) \int_{-\infty}^{\infty} d\zeta\, a_0 \mathscr{E}(\zeta) \frac{\exp[i(\eta(\zeta)+\eta_0)] + \exp[-i(\eta(\zeta)+\eta_0)]}{2} \exp\left[i\nu \int_{-\infty}^{\zeta} d\zeta' 1 + a_0^2 \mathscr{E}^2 \frac{1+\cos(2(\eta+\eta_0))}{2} \right] \right|^2 \tag{C.9}$$

This equation needs to be rewritten into the form where the SPA can be used; separate the slowly varying functions and a rapidly oscillating exponent. To obtain this we notice that the integral term in the exponent containing the cosine can be solved using the slowly varying amplitude approximation. To write the following steps more compact, we will only focus on the integrand with the exponent containing $-\eta(\zeta)$. This exponent, in addition, is included in the exponent with the integral. Thus now we have

$$a_0 \mathscr{E}(\zeta) \exp\left[i\nu \frac{a_0^2 \mathscr{E}^2}{2^2} \frac{\sin(2(\eta(\zeta)+\eta_0))}{\frac{\partial \eta}{\partial \zeta}} \right] \exp\left[i \int_{-\infty}^{\zeta} d\zeta' - \frac{\partial \eta}{\partial \zeta} + \nu \left(1 + \frac{a_0^2 \mathscr{E}^2}{2} \right) \right] \tag{C.10}$$

This result allows for the Jacobi-Anger expansion on the first exponent.

$$\exp[ia\sin(bx)] = \sum_{m=-\infty}^{\infty} \mathrm{J}(a) \exp[imb] \tag{C.11}$$

Using this expansion gives us

$$a_0 \mathscr{E} \sum_{m=-\infty}^{\infty} \mathrm{J}_m(B) \exp\left[i\eta_0 (2m-1) \right] \exp\left[i \int_{-\infty}^{\zeta} d\zeta' \frac{\partial \eta}{\partial \zeta} (2m-1) + \nu \left(1 + \frac{a_0^2 \mathscr{E}^2}{2} \right) \right], \tag{C.12}$$

where $B = \nu \left(\frac{a_0 \mathscr{E}}{2} \right)^2 \left(\frac{\partial \eta}{\partial \zeta} \right)^{-1}$. Combining with the other part of the integrand, i.e. with the exponent containing $+\eta(\zeta)+\eta_0$, leads to terms with $2m+1$. Because the summations of the Bessel functions run from $-\infty \leq m \leq \infty$ we can shift this summation to get the final form of the integrand:

$$\int_{=\infty}^{\infty} d\zeta\, a_0 \mathscr{E} \sum_{m=-\infty}^{\infty} \left(\mathrm{J}_m(B) + \mathrm{J}_{m+1}(B) \right) \frac{\exp\left[i\eta_0 (2m+1) \right]}{2} \exp\left[i \int_{-\infty}^{\zeta} d\zeta' \frac{\partial \eta}{\partial \zeta} (2m+1) + \nu \left(1 + \frac{a_0^2 \mathscr{E}^2}{2} \right) \right] \tag{C.13}$$

Using the stationary phase approximation we find can find two relations: 1) the emitted frequencies and 2) the stationary phase points. The former is given by the relation

$$\nu = -\frac{2m+1}{1 + \frac{a_0^2 \mathscr{E}^2(\zeta)}{2}} \frac{\partial \eta}{\partial \zeta} \tag{C.14}$$

From here we find that $m \leq 0$, since only positive frequencies are relevant. Notable is that $2m+1$ has a physical meaning: it is the harmonic number of the emitted radiation. To solve for the stationary phase points the following equation needs to be solved for ζ

$$\mathscr{E}(\zeta) = \sqrt{\left(-\frac{\partial \eta}{\partial \zeta} \frac{2m+1}{\nu} - 1 \right) \frac{2}{a_0^2}}. \tag{C.15}$$

This, however, depends on the chosen envelop function if there are analytical solutions available. It also needs to be noted that for a laser pulse with symmetric shape and a single maximum, the second derivative is zero at the peak of the pulse. This means that for this point the Stationary Phase Approximation fails and one should use the zero convexity approach. However the latter is not a good approximation far from the centre of the pulse. An analytical solution for the spectrum can only be constructed by piecewise functions.

C.3 Circular Polarization

The normalized vector potential of a circularly polarized plane wave (laser pulse) propagating in $+z$ is given by

$$a^{\mu} = a_0 \mathscr{E}(\zeta) \mathscr{R}_e \left(e^{i\eta(\zeta)+\eta_0} \begin{pmatrix} 0 \\ 1 \\ i \\ 0 \end{pmatrix} \right), \tag{C.16}$$

Substitution of the laser field into Eq. C.2 (through also Eq. A.47) leads to

$$\frac{d^2 I}{d\omega d\Omega} \propto \left| \nu\gamma(1+\beta) \int_{-\infty}^{\infty} d\zeta\, a_0 \mathscr{E}(\zeta) \left(\frac{\frac{\exp[i(\eta(\zeta)+\eta_0)]+\exp[-i(\eta(\zeta)+\eta_0)]}{2}}{\frac{\exp[i(\eta(\zeta)+\eta_0)]-\exp[-i(\eta(\zeta)+\eta_0)]}{2}} \right) \exp\left[i\nu \int_{-\infty}^{\zeta} d\zeta' 1 + a_0^2 \mathscr{E}^2 \right] \right|^2 \tag{C.17}$$

The two vectorial components are almost identical and therefore we will concentrate on the integrand of one. Moreover we will look to the to the term containing $-(\eta(\zeta)+\eta_0)$. The resulting integrand is given by

$$\int_{-\infty}^{\infty} d\zeta\, a_0 \mathscr{E} \exp\left[-i\eta_0\right] \exp\left[i \int_{-\infty}^{\zeta} d\zeta' - \frac{\partial \eta}{\partial \zeta} + \nu(1 + a_0^2 \mathscr{E}) \right] \tag{C.18}$$

Using the stationary phase approximation we find can find two relations: 1) the emitted frequencies and 2) the stationary phase points. The former is given by the relation

$$\nu = \frac{1}{1 + a_0^2 \mathscr{E}^2(\zeta)} \frac{\partial \eta}{\partial \zeta} \tag{C.19}$$

To solve for the stationary phase points the following equation needs to be solved for ζ

$$\mathscr{E}(\zeta) = \sqrt{\left(\frac{\partial \eta}{\partial \zeta} \frac{1}{\nu} - 1 \right) \frac{2}{a_0^2}}. \tag{C.20}$$

This, however, depends on the chosen envelop function if there are analytical solutions available. It also needs to be noted that for a laser pulse with symmetric shape and a single maximum, the second derivative is zero at the peak of the pulse.

C.4 Off-Axis Radiation

For radiation close to the backscattered angle we take a look at the interesting part of $\nu \int_{-\infty}^{\zeta} d\zeta' \gamma(1+\beta)(U^0 - \hat{n}\cdot\vec{U})$, namely

$$\gamma(1+\beta)(U^0 - \cos\vartheta U^3) = \gamma(1+\beta)\left(\gamma(1-\beta\cos\vartheta') + \gamma(1-\beta)\frac{(a)^2}{2}(1+\cos\vartheta') \right) \tag{C.21}$$

where $\vartheta' = \pi - \vartheta$. The cosine term is expanded for small angles. For the last term in the equation we only need to take the first order of the expansion. The first term however we need to take a couple of additional steps

$$\begin{aligned}\gamma(1+\beta)\gamma(1-\beta\cos\vartheta) = &\quad \gamma^2(1+\beta-\beta\cos\vartheta'-\beta^2\cos\vartheta')\\ = &\quad \gamma^2\left(1+\beta(1-(1+\tfrac{\vartheta'^2}{2}))-\beta^2(1+\tfrac{\vartheta'^2}{2})\right)\\ = &\quad \cancel{\gamma^2(1-\beta^2)}^{\,1}+\gamma^2\vartheta'^2\tfrac{\beta+\beta^2}{2}\\ \approx &\quad 1+\gamma^2\vartheta'^2\end{aligned} \tag{C.22}$$

If we use this relation in combination with Eq. C.14 and C.19 we find

$$\nu = \frac{\mathscr{H}}{1+\gamma^2\vartheta'^2+\langle a^2\rangle}\frac{\partial\eta}{\partial\zeta} \tag{C.23}$$

where $\mathscr{H}$ is the harmonic order and is equal to $2m+1$ for linear polarization and 1 for circular polarization, and $\langle a^2\rangle$ is non-oscillating magnitude square of the vector potential and is equal to $\frac{a_0^2\mathscr{E}^2}{2}$ for linear polarization and $a_0^2\mathscr{E}^2$ for circular polarization.